

CHALMERS



Polarimetric Decomposition of SAR Data for Forest Structure Assessment

*Master's Thesis in the Master Degree Program,
Wireless, Photonics and Space Engineering*

SHRINIWAS AGASHE

Department of Earth and Space Sciences

Radar Remote Sensing Group

CHALMERS UNIVERSITY OF TECHNOLOGY

Göteborg, Sweden 2013

MASTER'S THESIS IN RADAR REMOTE SENSING

Polarimetric Decomposition of SAR Data for Forest Structure Assessment

SHRINIWAS AGASHE

Department of Earth and Space Sciences

Radars Remote Sensing Group

CHALMERS UNIVERSITY OF TECHNOLOGY

Göteborg, Sweden 2013

Polarimetric Decomposition of SAR Data for Forest Structure Assessment

SHRINIWAS AGASHE

©SHRINIWAS AGASHE, 2013

Department of Earth and Space Sciences

Chalmers University of Technology

SE-412 96 Göteborg

Sweden

Telephone: +46 (0) 31-772 1000

Department of Earth and Space Sciences

Göteborg, Sweden 2013

Abstract

One of the prime factors in the global carbon budget is forest biomass, and it is estimated that about 20% of the carbon flux to the atmosphere comes from deforestation and disturbance. Thus, it is important to quantify the amount of biomass present on Earth for climate change studies and for the estimation of global carbon stock. Synthetic Aperture Radar (SAR) polarimetry finds a useful application in remote sensing of forests as it can help with the assessment of forest structure and above-ground forest biomass.

This thesis presents MATLAB implementation of three polarimetric target decomposition theorems, Pauli decomposition, Freeman-Durden decomposition, and H/A/alpha decomposition. The potential of air-borne SAR polarimetry for forest structure assessment is then evaluated using P- and L-band SAR data acquired with the ONERA SETHI system under the BioSAR 2010 campaign over the boreal forest of Remningstorp in southern Sweden. Results show that Freeman-Durden decomposition provides better visual classification of the forested area than Pauli and H/A/alpha decomposition techniques. Results also show that at L-band, most scattering occurs in forest canopy, while at P-band, forest canopy is penetrated to a higher degree and ground-locked mechanism takes over.

Also, a biomass estimation model is developed based on a linear regression analysis of different decomposition products. Results for P-band data show that of all studied parameters, the parameter $|\delta|$, which is a sensitive indicator for the amount of ground scattering visible, is best correlated with reference biomass. On the other hand, results for L-band data show that of all studied parameters, the parameter $|HH-VV|$ is best correlated with reference biomass. Biomass estimation model corresponding to parameter $|\delta|$, in case of P-band, and parameter $|HH-VV|$, in case of L-band, shows the lowest root mean square error of the order of 35-50 tons/ha, for all flight headings.

Key words: synthetic aperture radar (SAR), forest, decomposition theorems, biomass estimation model

Contents

Abstract	i
Contents	ii
Acknowledgements	v
1 Introduction	1
1.1 Background	1
1.2 Problem Description	2
1.3 Disposition	2
2 Radar systems	3
2.1 Radar Basics	3
2.2 Radar Equation and signal to noise ratio	4
2.3 Radar Cross section σ	5
2.4 Range and azimuth resolution	6
2.5 Synthetic aperture radar	6
3 Polarimetry theory	8
3.1 Jones vector	8
3.2 Scattering or Sinclair matrix	8
3.3 Scattering target vectors \underline{k} and $\underline{\Omega}$	9
3.4 Polarimetric coherency and covariance matrix	9
4 Polarimetric target decomposition theorems	11
4.1 Coherent decomposition	11
4.2 Model based decomposition	12
4.3 Eigenvalue-Eigenvector based decomposition	15
4.4 Miscellaneous definitions	17
4.4.1 Scattering mechanism indicator $ \delta $	17
4.4.2 Root mean square error	17
5 Data description and MATLAB program flow	18
5.1 BioSAR2010	18
5.2 Test site	18
5.3 Airborne SAR data acquisition	20
5.4 Reference biomass data	21
5.5 MATLAB program flow	21
6 Results and discussion	23
6.1 Heading Bio01	23
6.2 Decomposition results	24
6.2.1 Pauli decomposition	24

6.2.2 Freeman-Durden decomposition	28
6.2.3 H/A/alpha decomposition	30
6.3 Biomass modeling	31
6.4 Discussion on biomass modeling results	33
6.5 Heading Bio05 and Heading Bio07	33
6.6 Effect of heading on scattering mechanism	33
7 Conclusions	35
8 References	36
Appendix 1	37
Appendix 2	50
Appendix 3	63

Acknowledgements

I would like to thank my thesis supervisor Maciej Soja for his excellent guidance and continuous encouragement throughout the work. The constant feedbacks and future directions provided by him were of great help for the successful accomplishment of my work.

I am also grateful to Adjunct Professor Lars Ulander for introducing me to this interesting field of radar engineering and its applications as well as for the patient examination of my thesis work.

1. Introduction

1.1 Background

The world's forest resources play an important role by providing renewable raw materials and energy, maintaining biological diversity, mitigating climate changes, improving air quality and helping to alleviate poverty. At the same time, deforestation, mainly caused by the use of forest for agricultural and urban expansion, continues at an alarmingly high rate - about 13 million hectares per year [1]. One of the important characteristics of the forests is that they are vital carbon sink. Carbon stored in forests is very closely related to forest biomass. Forest biomass includes, all forest plants and forest plant derived materials [2]. In this thesis, forest biomass in the form of parts of the trees which are above the ground is only considered and referred to as the *Above Ground Biomass* (AGB). Above Ground Biomass is measured as dry mass per unit area. The changes in the area of forests and per hectare changes in the forest biomass resulting from the management and re-growth are the two factors which have dominated the long-term net flux of carbon between the terrestrial ecosystems and the atmosphere [3]. Thus, it is important to study changes in the forest structure and to estimate the forest biomass in order to study the global carbon cycle.

Forests cover 30% of the total land area and store 283 gigatonnes(Gt) of carbon in the form of the forest biomass [1]. However, forest biomass estimation is a strenuous task. Forest biomass is traditionally measured on field, but field measurements are labor intensive task. Also, they are far too expensive and have limitations because of the spatial variability of the forest structure. The development and use of high-resolution synthetic aperture radar (SAR) has proved useful for forest biomass mapping. Another promising technique for forest biomass estimation is LiDAR (**L**ight **D**etection **A**nd **R**anging). However, both these techniques are limited in the accuracy with which forest biomass can be estimated. In both these techniques, forest biomass is represented as a function of the backscattered signal. The backscattered signal carries information about forest canopy and tree stems. In addition to this information, the signal also carries additional information about soil and canopy moisture and ground topography. The interaction of the radar signal with the object of interest (tree stem in our case which mainly contains the forest biomass) and with its surroundings depends mainly upon the signal characteristics such as wavelength, incidence angle, polarization, and operational mode. All these factors affect the accuracy with which forest biomass can be estimated, as they affect the information content in the backscattered signal. Other factors that also can affect forest biomass estimation using these techniques include spatial variability, local tree species composition and distribution, and the non-monotonous development of forests in terms of height, density, and volume [4].

Radar polarimetry (*polar*: polarization, *metry*: measure) is the science of acquiring, processing and analyzing of the polarization state of an electromagnetic field [5]. Radar transmits electromagnetic waves with specific polarization towards an object. The polarization state of these electromagnetic waves can be changed as they pass through media with different refractive properties such as air and water, as well as when they strike an object. This may cause the scattered waves to have completely different polarization state than that of the incident waves. Change in the polarization state of the scattered waves depends upon the characteristic features of an object. Radar then receives these scattered waves with specific polarization state. Determination of the object features such as size, shape and dielectric properties from the measured properties of the received waves in comparison with the transmitted waves is the main objective in radar polarimetry.

Traditional, non-polarimetric radars transmit and receive signals with the same polarization states. The main disadvantage of this kind of radar is that they cannot help us to determine the complete vector nature of scattered signal. Because of that there is a loss of information regarding the target or the target is completely missed by the radar if the scattered signals have orthogonal sense of polarization. Polarimetric radar, on the other hand, transmits and receives signals with two orthogonal polarization states. One of the commonly used orthogonal bases is horizontal (H) and vertical (V). The measurement of both co-polarized signals (HH and VV) and cross polarized signals (HV and VH) facilitates the complete characterization of the scatterer. Right- and left-hand circular and linear $+45^\circ$ and -45° are other examples of orthogonal polarization bases [6].

Remote sensing with synthetic aperture radar makes great use of radar polarimetric techniques in order to study the environment and its dynamics. Indications of the natural hazards, effects of climatic changes, precise estimation of various natural resources, and oceans and costal monitoring are some of the areas of applications of SAR polarimetry [6].

1.2 Problem Description

The first objective of this thesis is to implement the following target decomposition theorems in MATLAB:

1. Pauli Decomposition theorem
2. H/A/ α decomposition theorem
3. Freeman-Durden three component decomposition theorem

The second objective is the structural assessment of forest by applying the above mentioned decomposition theorems to the available P-band and L-band airborne SAR data.

The third objective is to formulate and validate the model for biomass estimation from various scattering parameters obtained from the decomposition theorems.

1.3 Disposition

The thesis comprises of 8 chapters and 3 appendices. Chapter 2 explains the basics of radar systems. Chapter 3 illustrates the polarimetry theory and forms the foundation for Chapter 4, which describes polarimetric target decomposition theorems. Chapter 5 provides data description and MATLAB program flow. Chapter 6 describes and discusses the results. In Chapter 7, conclusions are drawn.

2. Radar Systems

2.1: Radar Basics

Radar is an abbreviation for **R**adio **D**etection **A**nd **R**anging [7]. Radar is a device for transmitting the electromagnetic (EM) signals and receiving echoes from the objects of interest (targets) within its volume of coverage [8]. Radar is thus used for remote sensing applications to study target characteristics. The main advantage of radar is that it is an active system, which means that radar does not require any external illumination. Thus, it can be operated during the day as well as during the night. Also, weather-independent capability makes radar a suitable device for remote sensing applications. Radars, when used for remote sensing applications, are usually mounted on the air- or space-borne systems such as airplanes or satellites. Thus, large areas can be monitored repeatedly over a period of time.

There exist mainly two types of radar systems

1) Monostatic Radar:

The monostatic radar uses the same antenna for both transmission and reception.

2) Bistatic Radar:

The bistatic radar is an example of multistatic radar system. It uses two separate antennas for transmission and reception of the electromagnetic waves.

An electromagnetic wave transmitted by radar possesses a specific polarization state. In the most commonly used H/V orthogonal polarization basis, polarization state is either horizontal (H) or the vertical (V). As waves propagate through the medium and as they hit a target, wave polarization state changes. The back scattered waves are then measured at a certain polarization state, for example horizontal or vertical. Depending upon the type of polarization state used for transmission and reception, the polarization mode is defined. For example, in case of the VH mode, transmission is done with the horizontally polarized antenna while reception is done with the vertically polarized antenna. A fully polarimetric system is capable of measuring all the four possible combinations, HH, HV, VH, and VV, of the two polarization states. Throughout this work, a fully polarimetric monostatic system is used.

The part of electromagnetic spectrum used by the radar systems is divided into so called radar bands. Table 1 shows the names of the radar frequency bands and corresponding frequency ranges. Use of a particular frequency band depends upon the application.

Table 1: Radar bands and their corresponding frequency intervals [9].

Band	Frequency (GHz)
HF	0.003-0.03
VHF	0.03-0.3
UHF	0.3-1
L	1-2
S	2-4
C	4-8
X	8-12
Ku	12-18
K	18-27
Ka	27-40
V	40-75
W	75-110

It is important to note that frequencies from 0.216 to 0.45 GHz are sometimes called P-band. Where, P stands for Previous, since early British radar used this band. This band does not belong to IEEE standard letter designations for radar-frequency bands.

2.2 Radar Equation and Signal to Noise Ratio

For the monostatic case, the power received by the radar antenna is given by the *radar equation* [8]:

$$P_r = \frac{P_t G^2 \lambda^2 \sigma}{(4\pi)^3 R^4 L}, \quad (2.1)$$

where P_t is the transmitted power, G is the gain of the radar antenna, λ is the wavelength, σ is the radar cross section (RCS) of the object (target), R is the distance of the object from the radar antenna, and L is the loss factor. The distance between the target and the radar antenna, which is often called range, is computed by measuring the time delay Δt between the transmission and the reception of the radar signal, and is given by:

$$R = \frac{c_0 \Delta t}{2}, \quad (2.2)$$

where free-space propagation is assumed and c_0 is the speed of light in vacuum, $c_0 \approx 3 \cdot 10^8$ m/s [10].

In practice, there is a noise that corrupts the received radar signal. Most of this noise is the thermal noise generated by the first stage of the receiver. It is important to define the signal to noise ratio which relates the strength of the received signal to the noise power. The noise power at the receiver input is given by [11],

$$P_n = k_B T B, \quad (2.3)$$

where k_B is the Boltzmann constant, $1.38 \cdot 10^{-23}$ J/K [10], T is the equivalent receiver noise temperature and B is the receiver bandwidth.

Hence, the signal to noise ratio is given by:

$$SNR_{rcvd} = \frac{P_r}{P_n} = \frac{P_t G^2 \lambda^2 \sigma}{(4\pi)^3 R^4 L k_B T B}. \quad (2.4)$$

2.3 Radar Cross Section σ

The radar cross section (RCS) for a target smaller than the radar footprint is defined as [8]:

$$\sigma = \lim_{R \rightarrow \infty} 4\pi R^2 \frac{\{\text{Power per unit area in scattered wave}\}}{\{\text{Power per unit area in a wave incident on target}\}},$$

$$\sigma = \lim_{R \rightarrow \infty} 4\pi R^2 \frac{|\vec{E}_S|^2}{|\vec{E}_I|^2}. \quad (2.5)$$

The radar cross section has the same dimension as that of area. RCS can be smaller or greater than the actual physical area of the object. RCS can only be taken into account if the far-field condition is satisfied. RCS depends strongly upon the frequency and polarization of the incident waves and it affects the characteristics of the scattered waves.

Radar cross section is a function of:

1. radar signal frequency,
2. wave Polarization,
3. imaging configuration that is incident and scattering directions,
4. geometrical structure of the target,

and

5. dielectric properties of the target

When the radar resolution is much larger than the wavelength, it is often useful to model the scattering as a collection of statistically independent point targets. In such a case, the final scattered wave is generated as a result of coherent addition of scattered waves from each independent target. Such a collection of individual point targets is modeled as an extended scatterer. The term σ^0 is called *scattering coefficient* and is defined as the statistically averaged radar cross section per unit ground area. σ^0 is the ratio of statistically averaged scattered power density to average incident power density over a surface of the sphere of radius r and is given by [6]:

$$\sigma^0 = \frac{\langle \sigma \rangle}{A_0} = \frac{4\pi r^2}{A_0} \frac{\langle |\vec{E}_S|^2 \rangle}{|\vec{E}_I|^2}. \quad (2.6)$$

σ^0 is dimensionless. In case of the extended scatterer, the RCS in the radar equation is replaced by $\sigma^0 A$, where A is the radar resolution cell. Similar to the RCS, σ^0 characterizes the scattered radiation and is a function of the same parameters as the RCS.

2.4 Range and Azimuth Resolution

Resolution is the ability to distinguish between closely located targets. In radar imagery, location of the target is determined by two parameters, slant range and azimuth. Slant range is the line-of-sight distance between radar antenna and the target. When projected on to the ground, slant range is referred to as ground range. Azimuth is the target position in the along track direction i.e. in the direction of flight. These concepts are illustrated in Figure 1. The ability to distinguish between closely located targets in range and azimuth directions is termed range and azimuth resolution of the radar.

Range resolution describes the ability of radar to distinguish between the targets located in the same direction but at different ranges. For a pulsed radar system, it is given by [12]:

$$\Delta R = \frac{c_0 \tau}{2}, \quad (2.7)$$

where τ is the length of the transmitted pulse expressed in seconds and c_0 is the speed of light in vacuum. Good range resolution requires thus short pulses. However, this affects signal to noise ratio. To overcome this problem, modern radar systems use pulse compression technique. The range resolution of such a system is given by [8]:

$$\Delta R = \frac{c_0}{2B}, \quad (2.8)$$

where B is the bandwidth of the transmitted pulse.

Azimuth resolution describes the ability of radar to separate two closely spaced objects in the direction of motion. It is given by [12]:

$$\Delta A \approx \frac{\lambda R}{D}, \quad (2.9)$$

where λ is the signal wavelength, D is the radar antenna size where $D \gg \lambda$ and R is the slant range. Thus, good azimuth resolution requires large antenna.

2.5 Synthetic Aperture Radar

Many applications, such as geographic mapping, environmental monitoring and military applications demand high resolution imagery. However, as mentioned in the previous section, to achieve good resolution, large antenna is needed, which is impractical or even impossible in airborne and spaceborne systems. The need for large aperture can be fulfilled by the use of the synthetic aperture technique. It is a method of achieving high resolution by using the flight path of the platform to simulate a larger aperture. This is shown in the Figure 2 [15].

Azimuth resolution for synthetic aperture radar (SAR) in stripmap mode is given by [8]:

$$\Delta A = \frac{R\lambda}{2D_x} \approx \frac{D}{2}, \quad (2.10)$$

where $D \gg \lambda$. As it can be seen, the azimuth resolution of the SAR depends only on the antenna size in the azimuth direction and is independent of the wavelength and slant range. Figure 1 shows SAR resolution cell [15].

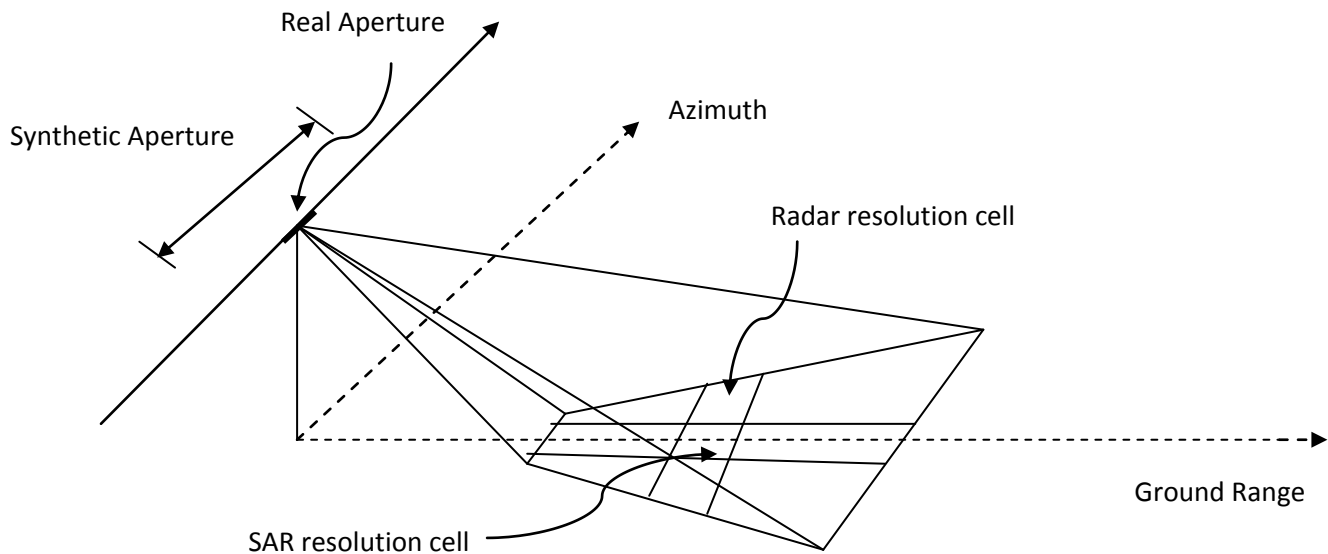


Figure 1: Basic radar and SAR geometry

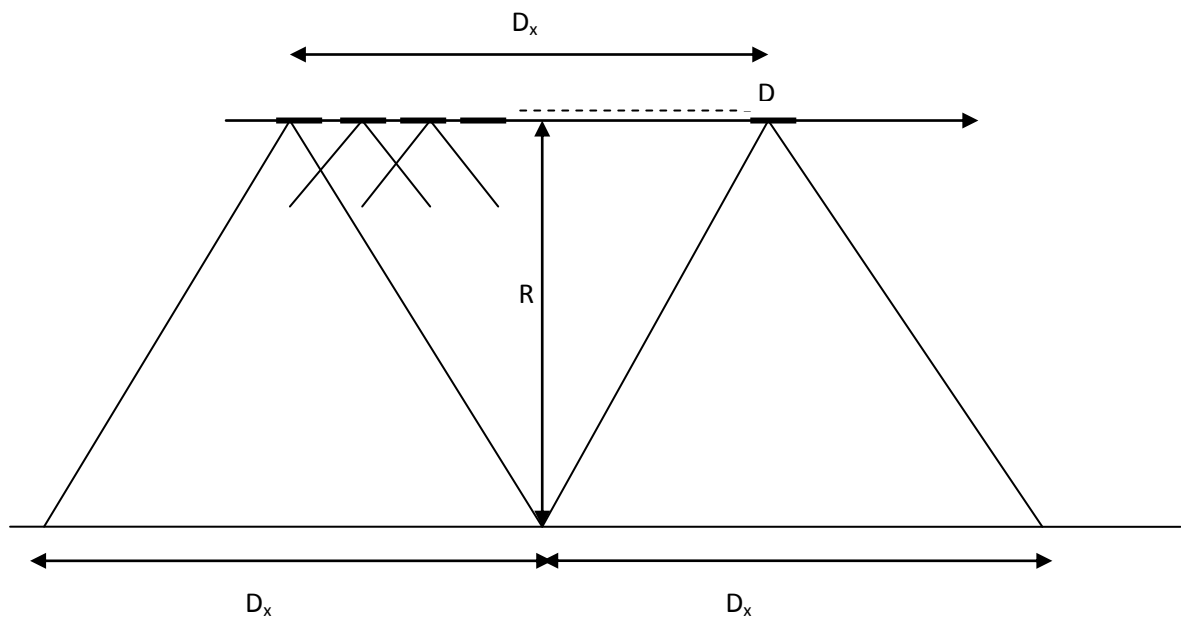


Figure 2: Synthetic aperture realization

3. Polarimetry Theory

3.1 Jones Vector

Polarization state of a plane monochromatic electric field is represented in its most compact form by the introduction of the Jones vector [6].

An electric field vector in an orthogonal basis ($\hat{x}, \hat{y}, \hat{z}$), located in the plane perpendicular to the direction of propagation along \hat{z} can be represented in time domain as:

$$\vec{E}(z,t) = \begin{bmatrix} E_{0x} \cos(\omega t - kz + \delta_x) \\ E_{0y} \cos(\omega t - kz + \delta_y) \end{bmatrix} \quad (3.1)$$

$$\vec{E}(z,t) = \text{Re} \left\{ \begin{bmatrix} E_{0x} e^{j\delta_x} \\ E_{0y} e^{j\delta_y} \end{bmatrix} e^{-jkz} e^{j\omega t} \right\} \quad (3.2)$$

$$\vec{E}(z,t) = \text{Re} \{ \underline{\underline{E}}(z) e^{j\omega t} \} \quad (3.3)$$

For the monochromatic case, we can neglect the time dependence. With $z=0$, we get,

$$\underline{\underline{E}} = \underline{\underline{E}}(z)|_{z=0} = \underline{\underline{E}}(0) = \begin{bmatrix} E_{0x} e^{j\delta_x} \\ E_{0y} e^{j\delta_y} \end{bmatrix} \quad (3.4)$$

$\underline{\underline{E}}$ is called as the Jones vector. The Jones vector completely defines the amplitude and phase of the complex orthogonal components of an electric field.

3.2 Scattering or Sinclair Matrix

Assuming that the incident and scattered waves are characterized by their corresponding Jones vectors, $\underline{\underline{E}}_I$ and $\underline{\underline{E}}_S$, respectively, the scattering process at the target can be represented in terms of these Jones vectors as [6]:

$$\underline{\underline{E}}_S = \frac{e^{-jkr}}{r} S \underline{\underline{E}}_I = \frac{e^{-jkr}}{r} \begin{bmatrix} S_{11} & S_{12} \\ S_{21} & S_{22} \end{bmatrix} \underline{\underline{E}}_I \quad (3.5)$$

where matrix S is named as the *scattering matrix* and elements of it are referred to as the *complex scattering coefficients*. Since the diagonal elements relate the same polarization of incident and scattered fields, they are known as the *co-polar* terms, while the off-diagonal elements are known as *cross-polar* terms, as they relate the orthogonal polarization of the incident and scattered fields. In case of a monostatic system, the reciprocity theorem results in equal cross-polar terms, that is $S_{12} = S_{21}$. Term $\frac{e^{-jkr}}{r}$ takes into account the propagation effects, both in amplitude and phase. Relation (3.5) holds only in the far-field zone where the incident and scattered fields are assumed to be planar.

If q represents the polarization of an incident field and p represents the polarization of the scattered field then, the RCS of the target can be related to the scattering matrix elements as:

$$\sigma_{qp} = 4\pi |S_{qp}|^2. \quad (3.6)$$

Hence, the scattering matrix characterizes the given target.

The values of the complex scattering coefficients S_{ij} are coordinate system and polarization basis dependent.

3.3 Scattering Target Vectors \underline{k} and $\underline{\Omega}$

Vectorization of the 2×2 coherent Sinclair matrix is required in order to extract the physical information about the target. Vectorization of the S-matrix yields a target vector \underline{k} . For monostatic case, the 3-D \underline{k} -target vector or 3-D Pauli feature vector is given by:

$$\underline{k} = \frac{1}{\sqrt{2}} \begin{bmatrix} S_{XX} + S_{YY} \\ S_{XX} - S_{YY} \\ 2S_{XY} \end{bmatrix}. \quad (3.7)$$

The corresponding 3-D $\underline{\Omega}$ -target vector or 3-D Lexicographic feature vector is given by:

$$\underline{\Omega} = \begin{bmatrix} S_{XX} \\ \sqrt{2}S_{XY} \\ S_{YY} \end{bmatrix}. \quad (3.8)$$

The two target vectors are related as:

$$\underline{k} = U_{3(L \rightarrow P)} \underline{\Omega}, \quad (3.9)$$

where

$$U_{3(L \rightarrow P)} = \frac{1}{\sqrt{2}} \begin{bmatrix} 1 & 0 & 1 \\ 1 & 0 & -1 \\ 0 & \sqrt{2} & 0 \end{bmatrix}, \quad (3.10)$$

is the special unitary transformation with $|U_{3(L \rightarrow P)}| = 1$ and $U_{3(L \rightarrow P)}^{-1} = U_{3(L \rightarrow P)}^{*T}$

Total power is given by:

$$Total\ Power = Span = |\underline{k}|^2 = |\underline{\Omega}|^2 = |S_{XX}|^2 + 2|S_{XY}|^2 + |S_{YY}|^2 \quad (3.11)$$

3.4 Polarimetric Coherency and Covariance Matrix

Many of the radar targets are situated in the dynamically changing environment and undergo spatial and temporal variations. Such scatterers are referred to as *distributed targets*. In spite of the dynamically changing environment, assumptions of stationarity, homogeneity and ergodicity have to be made. In order to carry out the analysis, the concept of a space and time varying stochastic process is introduced. In this concept, the target or the environment can be described by the second order moments of fluctuations. These moments are extracted from the polarimetric coherency or covariance matrices.

For the monostatic backscattering case, the polarimetric coherency and covariance matrices are given by [6]:

$$T_3 = \langle \underline{k}, \underline{k}^{*T} \rangle = \left\langle \begin{bmatrix} |k_1|^2 & k_1 k_2^* & k_1 k_3^* \\ k_2 k_1^* & |k_2|^2 & k_2 k_3^* \\ k_3 k_1^* & k_3 k_2^* & |k_3|^2 \end{bmatrix} \right\rangle, \quad (3.12)$$

$$T_3 = \frac{1}{2} \left[\begin{array}{ccc} \langle |S_{XX} + S_{YY}|^2 \rangle & \langle (S_{XX} + S_{YY})(S_{XX} - S_{YY})^* \rangle & 2\langle (S_{XX} + S_{YY})S_{XY}^* \rangle \\ \langle (S_{XX} - S_{YY})(S_{XX} + S_{YY})^* \rangle & \langle |S_{XX} - S_{YY}|^2 \rangle & 2\langle (S_{XX} - S_{YY})S_{XY}^* \rangle \\ 2\langle S_{XY}(S_{XX} + S_{YY})^* \rangle & 2\langle S_{XY}(S_{XX} - S_{YY})^* \rangle & 4\langle |S_{XY}|^2 \rangle \end{array} \right], \quad (3.13)$$

and

$$C_3 = \langle \underline{\Omega}, \underline{\Omega}^{*T} \rangle = \left\langle \begin{bmatrix} |\Omega_1|^2 & \Omega_1 \Omega_2^* & \Omega_1 \Omega_3^* \\ k_2 k_1^* & |\Omega_2|^2 & \Omega_2 \Omega_3^* \\ \Omega_3 \Omega_1^* & \Omega_3 \Omega_2^* & |\Omega_3|^2 \end{bmatrix} \right\rangle, \quad (3.14)$$

$$C_3 = \left[\begin{array}{ccc} \langle |S_{XX}|^2 \rangle & \sqrt{2}\langle S_{XX}S_{XY}^* \rangle & \langle S_{XX}S_{YY}^* \rangle \\ \sqrt{2}\langle S_{XY}S_{XX}^* \rangle & \langle |S_{XY}|^2 \rangle & \sqrt{2}\langle S_{XY}S_{YY}^* \rangle \\ \langle S_{YY}S_{XX}^* \rangle & \sqrt{2}\langle S_{YY}S_{XY}^* \rangle & \langle |S_{YY}|^2 \rangle \end{array} \right]. \quad (3.15)$$

3×3 polarimetric coherency and covariances matrices are related by:

$$T_3 = U_{3(L \rightarrow P)} C_3 U_{3(L \rightarrow P)}^{-1} \quad (3.16)$$

where

$$U_{3(L \rightarrow P)} = \frac{1}{\sqrt{2}} \begin{bmatrix} 1 & 0 & 1 \\ 1 & 0 & -1 \\ 0 & \sqrt{2} & 0 \end{bmatrix} \quad (3.17)$$

4. Polarimetric Target Decomposition Theorems

Scattering matrices are often stochastic in nature rather than deterministic. Target decomposition theorems help to determine the various scattering mechanisms involved by expressing average scattering matrix as a sum of independent matrices, each associated with an elementary scattering mechanism. It is also possible to determine the dominant scattering mechanism using target decomposition theorems. Huynen was the first to formalize target decomposition theorems, which have the roots in the work of Chandrashekhara on light scattering by small anisotropic particles [6].

Target decomposition theorems can be classified into four main types [6]:

1. Those employing coherent decomposition of scattering matrix S (Pauli, Krogager, Cameron, Touzi);
2. Those based on model-based decomposition of the T_3 or C_3 matrix (Freeman and Durden, Yamaguchi, Dong);
3. Those using an eigenvector or eigenvalue analysis of the T_3 or C_3 matrix (H/A/alpha, Holm, van Zyl);
4. Those based on dichotomy of the Kennaugh matrix K (Huynen, Holm and Barnes, Yang).

In order to study the forest structure, the first three types of decomposition theorems are particularly useful [6]. Therefore, three main decomposition theorems will be studied: Pauli decomposition, Freeman-Durden three component decomposition, and H/A/alpha decomposition.

4.1 Coherent Decomposition

The coherent decomposition aims to express the measured S matrix as a combination of canonical scattering mechanism matrices:

$$S = \sum_{k=1}^N \alpha_k S_k. \quad (4.1)$$

Pauli Decomposition:

For monostatic case, Pauli decomposition decomposes S matrix into three scattering mechanisms:

1. Single scattering by plane surface (single or odd bounce scattering),
2. Diplane scattering from corners with a relative orientation of 0° (double or even bounce scattering),
3. Diplane scattering from corners with a relative orientation of 45° (double or even bounce scattering).

These scattering mechanisms are represented by Pauli matrices. Scattering matrix, S , is represented as the sum of these matrices:

$$S = \begin{bmatrix} S_{HH} & S_{HV} \\ S_{VH} & S_{VV} \end{bmatrix} = \frac{a}{\sqrt{2}} \begin{bmatrix} 1 & 0 \\ 0 & 1 \end{bmatrix} + \frac{b}{\sqrt{2}} \begin{bmatrix} 1 & 0 \\ 0 & -1 \end{bmatrix} + \frac{c}{\sqrt{2}} \begin{bmatrix} 0 & 1 \\ 1 & 0 \end{bmatrix}, \quad (4.2)$$

where a, b, and c are the all complex parameters given by,

$$a = \frac{S_{HH} + S_{VV}}{\sqrt{2}} \quad (4.3)$$

$$b = \frac{S_{HH} - S_{VV}}{\sqrt{2}} \quad (4.4)$$

$$c = \frac{S_{HV} + S_{VH}}{\sqrt{2}} \quad (4.5)$$

The span, which is a measure of total scattered power, is given by,

$$Span = |S_{HH}|^2 + 2|S_{HV}|^2 + |S_{VV}|^2 = |a|^2 + |b|^2 + |c|^2 \quad (4.6)$$

4.2 Model Based Decomposition

Freeman-Durden Decomposition:

In the Freeman-Durden decomposition technique, a three-component scattering model based on the physics of radar scattering is fitted to polarimetric SAR observations. The three scattering mechanisms which constitute a scattering model are:

1. Bragg scattering for moderately rough surface,
2. Even bounce scattering from a pair of orthogonal surfaces with different dielectric constants,
3. Volume scattering from a cloud of randomly oriented dipoles.

The first component, Bragg surface scattering, models scattering from slightly rough surface with the scattering matrix given by:

$$S = \begin{bmatrix} R_H & 0 \\ 0 & R_V \end{bmatrix}, \quad (4.7)$$

where R_H and R_V are the reflection coefficients for horizontally and vertically polarized waves given by:

$$R_H = \frac{\cos \theta - \sqrt{\epsilon_r - \sin^2 \theta}}{\cos \theta + \sqrt{\epsilon_r - \sin^2 \theta}}, \quad (4.8)$$

$$R_V = \frac{(\epsilon_r - 1)\{\sin^2 \theta - \epsilon_r(1 + \sin^2 \theta)\}}{(\epsilon_r \cos \theta + \sqrt{\epsilon_r - \sin^2 \theta})^2}, \quad (4.9)$$

where θ is the local incidence angle and ϵ_r is the relative dielectric constant of the surface.

The surface scattering covariance matrix, C_{3S} , corresponding to the scattering matrix above is given by:

$$C_{3S} = \begin{bmatrix} |R_H|^2 & 0 & R_H R_H^* \\ 0 & 0 & 0 \\ R_V R_H^* & 0 & |R_V|^2 \end{bmatrix} = f_s \begin{bmatrix} |\beta|^2 & 0 & \beta \\ 0 & 0 & 0 \\ \beta^* & 0 & 1 \end{bmatrix}, \quad (4.10)$$

where f_s is the contribution of the single bounce scattering to the $|S_{VV}|^2$ component and can be obtained as:

$$f_s = |R_V|^2 \text{ and } \beta = \frac{R_H}{R_V}.$$

The second component, even bounce scattering, is modeled by scattering from a dihedral corner reflector. The corresponding scattering matrix is given by,

$$S = \begin{bmatrix} e^{2j\gamma_H} R_{TH} R_{GH} & 0 \\ 0 & e^{2j\gamma_V} R_{TV} R_{GV} \end{bmatrix} \quad (4.11)$$

where, R_{TH} and R_{TV} are the reflection coefficients of the vertical surface of a dihedral for horizontal and vertical polarizations, respectively and R_{GH} and R_{GV} are the reflection coefficients of the horizontal surface of a dihedral for horizontal and vertical polarizations, respectively. Here, $e^{2j\gamma_H}$ and $e^{2j\gamma_V}$ are propagation factors with γ_H and γ_V representing the attenuation and phase change effects occurring during propagation.

The double bounce scattering covariance matrix C_{3D} corresponding to the scattering matrix above is given by:

$$C_{3D} = \begin{bmatrix} |R_{TH} R_{GH}|^2 & 0 & e^{2j(\gamma_H - \gamma_V)} R_{TH} R_{GH} R_{TV}^* R_{GV}^* \\ 0 & 0 & 0 \\ e^{2j(\gamma_H - \gamma_V)} R_{TV} R_{GV} R_{TH}^* R_{GH}^* & 0 & |R_{TV} R_{GV}|^2 \end{bmatrix}, \quad (4.12)$$

$$C_{3D} = f_D \begin{bmatrix} |\alpha|^2 & 0 & \alpha \\ 0 & 0 & 0 \\ \alpha^* & 0 & 1 \end{bmatrix}, \quad (4.13)$$

where f_D is the contribution of double bounce scattering to the $|S_{VV}|^2$ component and

$$f_D = |R_{TV} R_{GV}|^2 \text{ and } \alpha = e^{2j(\gamma_H - \gamma_V)} \frac{R_{TH} R_{GH}}{R_{TV} R_{GV}}.$$

The third component, volume scattering, is modeled by the scattering from a cloud of randomly oriented cylinder shaped scatterers. The averaged covariance matrix for volume scattering from a cloud of randomly oriented, horizontally very thin, cylindrical scatterers is given by:

$$\langle C_{3V} \rangle_\theta = \frac{f_V}{8} \begin{bmatrix} 3 & 0 & 1 \\ 0 & 2 & 0 \\ 1 & 0 & 3 \end{bmatrix}, \quad (4.14)$$

where f_V is the contribution of the volume scattering component.

If three components above are uncorrelated, the model for the total backscatter is given by:

$$C_{3V} = C_{3S} + C_{3D} + \langle C_{3V} \rangle_{\theta}, \quad (4.15)$$

$$C_{3V} = \begin{bmatrix} f_S |\beta|^2 + f_D |\alpha|^2 + \frac{3f_V}{8} & 0 & f_S \beta + f_D \alpha + \frac{f_V}{8} \\ 0 & \frac{2f_V}{8} & 0 \\ f_S \beta^* + f_D \alpha^* + \frac{f_V}{8} & 0 & f_S + f_D + \frac{3f_V}{8} \end{bmatrix}. \quad (4.16)$$

The above model consists of four equations with five unknowns. If the volume contribution is subtracted from the $|S_{HH}|^2$, $|S_{VV}|^2$ and $S_{HH}S_{VV}^*$ terms, then we get:

$$\langle S_{HH}S_{HH}^* \rangle = f_S |\beta|^2 + f_D |\alpha|^2, \quad (4.17)$$

$$\langle S_{HH}S_{VV}^* \rangle = f_S \beta + f_D \alpha, \quad (4.18)$$

$$\langle S_{VV}S_{VV}^* \rangle = f_S + f_D. \quad (4.19)$$

Van Zyl suggested a way to determine the value of one unknown so that total solution can be found [6]. According to van Zyl, if $Re(\langle S_{HH}S_{VV}^* \rangle) \geq 0$, then surface scattering is dominant and $\alpha = -1$. Otherwise, double bounce scattering is dominant and $\beta = +1$.

The span, which is a measure of total scattered power, is given by:

$$Span = |S_{HH}|^2 + 2|S_{HV}|^2 + |S_{VV}|^2 = P_S + P_D + P_V, \quad (4.20)$$

where

$$P_S = f_S(1 + |\beta|^2), \quad (4.21)$$

$$P_D = f_D(1 + |\alpha|^2), \quad (4.22)$$

$$P_V = f_V. \quad (4.23)$$

This model makes following two assumptions:

1. Three component scattering model is always applicable,
2. There always is a reflection symmetry leading to: $\langle S_{HH}S_{HV}^* \rangle = \langle S_{HV}S_{VV}^* \rangle = 0$.

These assumptions limit the applicability of the Freeman-Durden decomposition. The first assumption limits the applicability to a class of scattering problems and becomes invalid where the three component scattering model is not applicable, for example, in case of the surface scattering with entropy other than zero. The second assumption limits the applicability as it holds when the scattering media exhibit either reflection symmetry or rotation symmetry or even mixing both.

4.3 Eigenvalue-Eigenvector Based Decomposition

H/A/alpha Polarimetric Decomposition Theorem:

This method is based on the eigenvalue-eigenvector based analysis of coherency matrix T_3 [6]. It provides a basis invariant description of scatterer. Eigenvector analysis provides information about different types of scattering processes, while eigenvalue analysis provides information about their relative magnitudes.

The coherency matrix T_3 can be written in terms of its eigenvalues and eigenvectors as:

$$T_3 = U_3 \Sigma U_3^{-1}, \quad (4.24)$$

where Σ is a 3×3 diagonal matrix containing eigenvalues of the T_3 matrix given by:

$$\Sigma = \begin{bmatrix} \lambda_1 & 0 & 0 \\ 0 & \lambda_2 & 0 \\ 0 & 0 & \lambda_3 \end{bmatrix}, \quad (4.25)$$

and $U_3 = [\underline{u}_1 \ \underline{u}_2 \ \underline{u}_3]$ is a 3×3 matrix containing three unit orthogonal eigen vectors \underline{u}_1 , \underline{u}_2 and \underline{u}_3 . An eigenvector of averaged coherency T_3 matrix can be parameterized as:

$$\underline{u} = [\cos \alpha e^{j\phi} \quad \sin \alpha \cos \beta e^{j(\delta+\phi)} \quad \sin \alpha \sin \beta e^{j(\gamma+\phi)}]^T. \quad (4.26)$$

The diagonal form of the T_3 matrix, which is described by the equation 4.24, can be considered as a statistically independent set of target vectors. Thus, the coherency matrix T_3 can be decomposed into three independent targets, each represented by a single scattering matrix:

$$T_3 = \sum_{i=1}^3 \lambda_i T_{3i} = \sum_{i=1}^3 \lambda_i \underline{u}_i \underline{u}_i^{T*}. \quad (4.27)$$

The mean parameters of the dominant scattering mechanism are extracted from the 3×3 coherency matrix using:

$$\bar{x} = \sum_{i=1}^3 P_i x_i, \quad (4.28)$$

Where x_i is the element in the random sequence followed by any target parameter x , and P_i is the pseudo-probability of occurrence of each target which is given by:

$$P_i = \frac{\lambda_i}{\sum_{k=1}^3 \lambda_k} \text{ and } \sum_{i=1}^3 P_i = 1. \quad (4.29)$$

A mean unit target vector thus can be constructed as:

$$\underline{u}_0 = e^{j\phi} \begin{bmatrix} \cos \bar{\alpha} \\ \sin \bar{\alpha} \cos \bar{\beta} e^{j\bar{\delta}} \\ \sin \bar{\alpha} \sin \bar{\beta} e^{j\bar{\gamma}} \end{bmatrix}, \quad (4.30)$$

where ϕ is the absolute target phase.

Polarimetric Scattering Parameter ($\bar{\alpha}$):

As $\bar{\alpha}$ is roll invariant parameter, it is the main parameter for identifying the dominant scattering mechanism. The value of $\bar{\alpha}$ can be easily associated with the physics behind the scattering process involved.

The value of $\bar{\alpha}$ varies continuously within the useful range of 0^0 to 90^0 . Each of the $\bar{\alpha}$ values 0^0 , 45^0 and 90^0 , and the continuous range in between them can be related to the specific scattering mechanism. This is described below.

1. $\bar{\alpha} = 0^0$ represents isotropic odd bounce scattering, like surface scattering in geometrical optics where the surface roughness variation is larger than the wavelength of incident wave.
2. $0^0 \leq \bar{\alpha} \leq 45^0$ represents anisotropic odd bounce scattering, like surface scattering in physical optics where the surface roughness variation is smaller than the wavelength of incident wave.
3. $\bar{\alpha} = 45^0$ represents Bragg surface model, like the dipole or volume scattering by cloud of anisotropic particles.
4. $45^0 \leq \bar{\alpha} \leq 90^0$ represents anisotropic even or multiple bounce scattering, like scattering from two perpendicular dielectric surfaces.
5. $\bar{\alpha} = 90^0$ represents isotropic even or multiple bounce scattering, like the reflection from two perpendicular metallic surfaces.

Polarimetric Scattering Entropy (H):

The averaged coherency matrix T_3 has the three eigen values λ_1, λ_2 and λ_3 .

Polarimetric scattering entropy is defined using these three eigenvalues as:

$$H = -\sum_{k=1}^N P_k \log_N(P_k), \quad (4.31)$$

where P_k are the pseudo-probabilities determined from the eigenvalues as:

$$P_k = \frac{\lambda_k}{\sum_{i=1}^3 \lambda_i}. \quad (4.32)$$

N is equal to the polarimetric dimension. Thus, $N=3$ for the monostatic case and $N=4$ for the bistatic case.

Polarimetric scattering entropy is a roll invariant parameter as the eigenvalues are rotational invariant. Polarimetric scattering entropy H is a measure of statistical disorder of each different scatterer within the group.

1. $H=0$ indicates a single scattering mechanism.
2. A low value of H (often $H<0.3$) indicates scattering from a dominant scatterer and the system is considered to be weakly depolarizing.
3. A high value of H (often $H>0.3$) indicates depolarizing system of scatterers and scattering is from the mixture of point scatterers.

4. $H=1$ indicates random target scattering process and represents completely depolarizing system.

Polarimetric scattering anisotropy (A):

The parameter complementary to polarimetric scattering entropy is polarimetric scattering anisotropy:

$$A = \frac{\lambda_2 - \lambda_3}{\lambda_2 + \lambda_3}, \quad (4.33)$$

with $\lambda_1 > \lambda_2 > \lambda_3 > 0$.

It is a very useful parameter especially when the polarimetric entropy reaches a high value. Anisotropy is a measure of relative importance of λ_2 and λ_3 . For low H values (approximately $H < 0.7$), λ_2 and λ_3 are highly affected by noise, which gives noisy anisotropy. As the value of H increases (approximately $H > 0.7$), it becomes difficult to distinguish between different types of scattering processes involved. Anisotropy becomes then a useful parameter for identification of the number of distinguishable scattering processes.

4.4 Miscellaneous Definitions

4.4.1 Scattering Mechanism Indicator $|\delta|$

Parameter $|\delta|$ is a sensitive indicator for the amount of ground scattering visible. It is related to the scattering mechanism indicator $\bar{\alpha}$ through relation [5]:

$$|\delta| = \tan \bar{\alpha} \quad (4.34)$$

4.4.2 Root Mean Square Error

Root mean square error of a parameter y is defined as [19]:

$$RMSE = \sqrt{\left(\frac{1}{n} \sum_{i=1}^n (y_i - \hat{y}_i)^2\right)} \quad (4.35)$$

where y_i is the modeled value and \hat{y}_i is the reference value of the parameter y .

5. Data Description and MATLAB Program Flow

5.1 BioSAR2010

BIOMASS is the proposed satellite mission for the seventh Earth Explorer Mission within ESA's Living Planet Program. The overall goal of this campaign was to provide polarimetric, interferometric, and tomographic radar mapping of forested area covered by the test site for better understanding of carbon stocks and fluxes in relation to the vegetation and climate modeling.

In support of the Earth Explorer BIOMASS mission, an ESA funded airborne SAR campaign BioSAR2010 (BioSAR-3) was carried out in Remningstorp, southern Sweden. BioSAR campaigns collected airborne data that would support the BIOMASS mission. The first two campaigns were BioSAR-1 (BioSAR 2007) and BioSAR-2 (BioSAR 2008). They were carried out at Remningstorp which is located in the Southern Sweden and at Krycklan which is located in the Northern Sweden respectively. BioSAR-3 (BioSAR 2010) was the most recent campaign that was carried out at Remningstorp. The same test site was used for both the campaigns BioSAR-1 and BioSAR-3. One of the main objectives of the BioSAR-3 campaign was to detect and map the temporal changes in the forest biomass and disturbances in relation to the data and results from the BioSAR-1 campaign. The test site for that reason had to be the same for BioSAR-3 campaign as for the BioSAR-1 campaign. This thesis work focuses on the data acquired during BioSAR-3 campaign over the test site of Remningstorp.

5.2 Test Site

The Remningstorp test site is located in southern Sweden ($58^{\circ}30'N$, $13^{\circ}40'E$). Location of the test site is shown in Figure 3. Figure 4 shows an aerial image of the test site. The Remningstorp test site covers over 1500 ha area including both land and water, of which about 1200 ha is productive forest land. The estate is divided into 665 delineated regions, as shown in Figure 5.

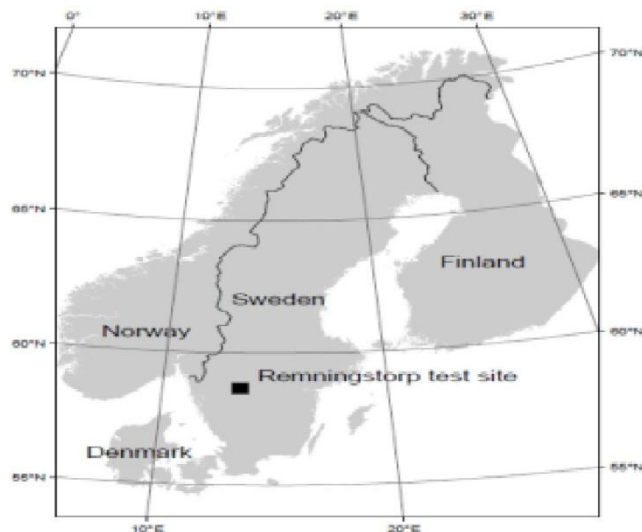


Figure 3: Location of the Remningstorp test site ($58^{\circ}30'N$, $13^{\circ}40'E$) [13].

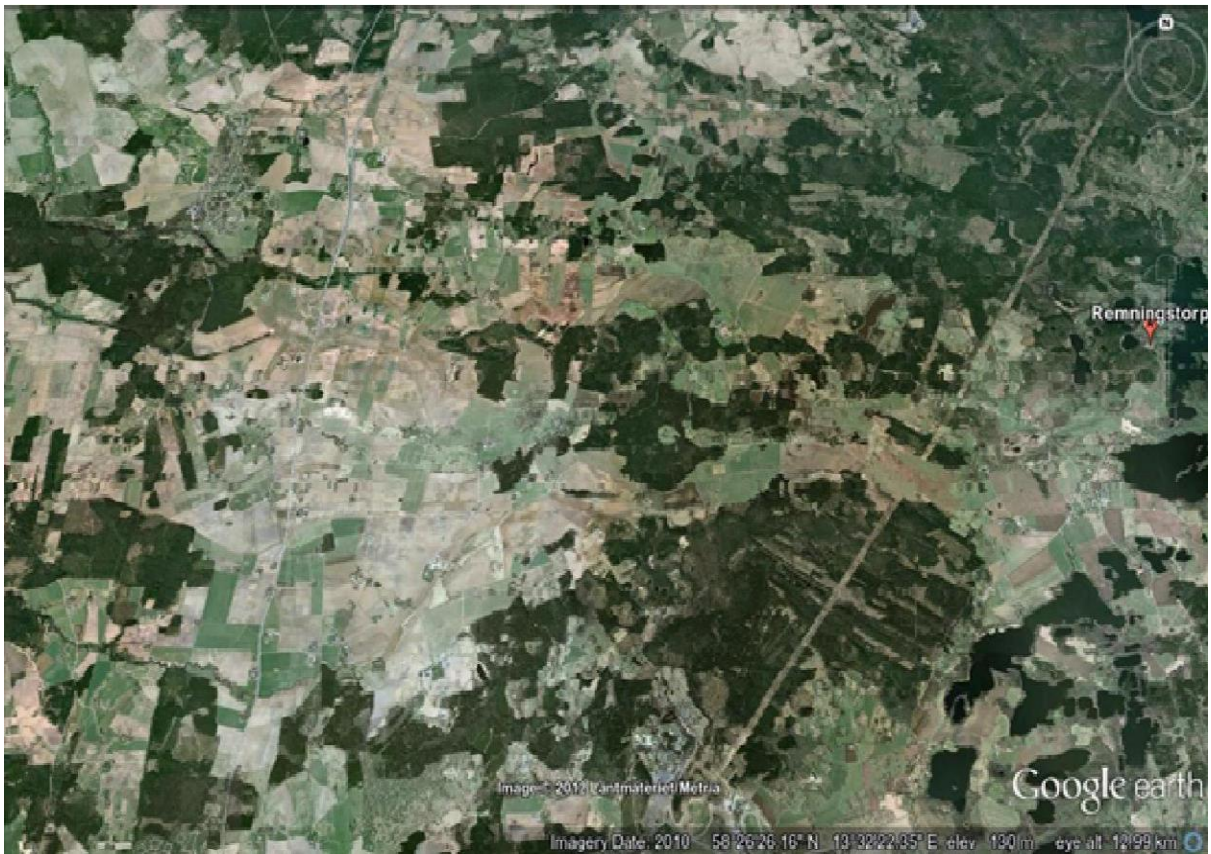


Figure 4: Aerial image of the Remningstorp test site [14].

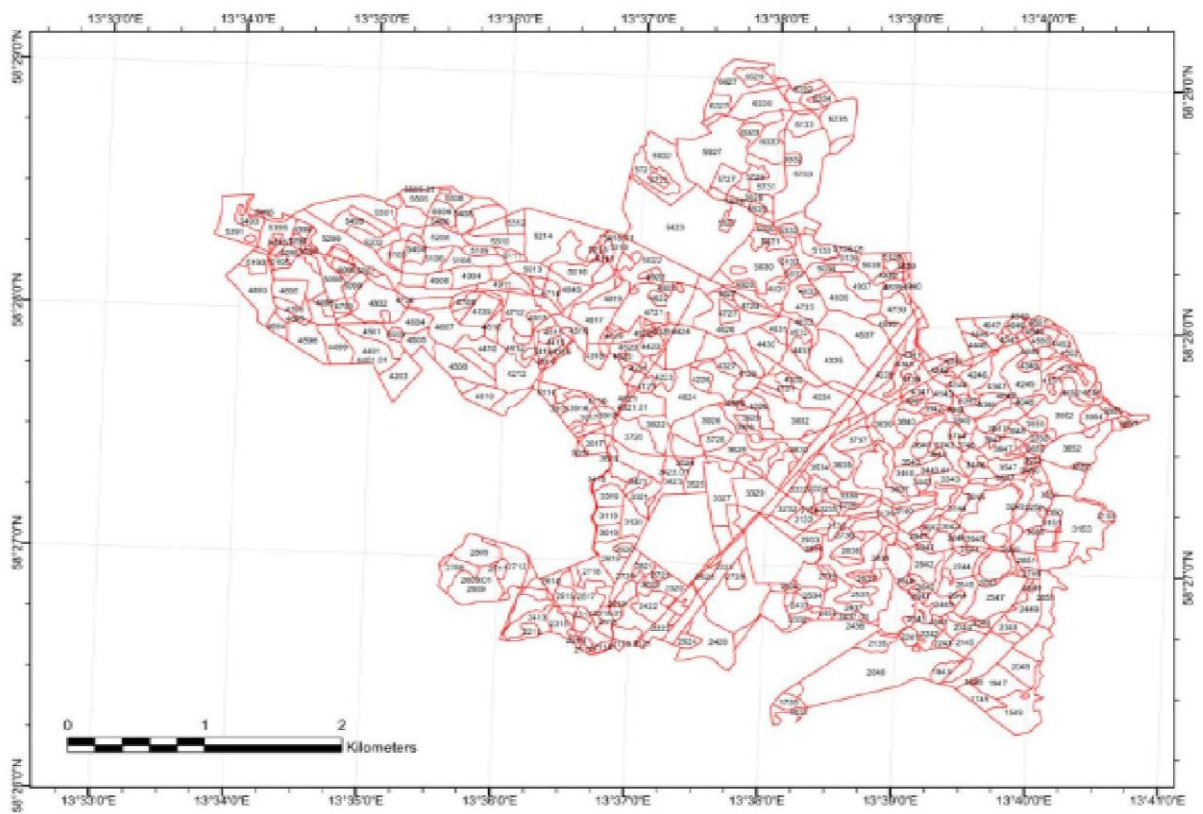


Figure 5: The forest stands in Remningstorp test site with identification numbers [13].

The test site is dominated by Norway spruce (*Picea abies*), Scots pine (*Pinus sylvestris*) and birch (*Betula spp.*) [13]. A few forest stands contain primarily oak (*Quercus robur*) and beech (*Fagus sylvatica*). The major soil type is till. Some field layer present consists of blueberry (*Vaccinium myrtillus*) and narrow thinned grass (*Deschampsia flexuosa*). Stand-level biomass values for the Remningstorp test site reach a maximum value of about 370 tons/ha [13]. The test site has overall flat ground terrain, with height variations between 120 m to 145 m above sea level. However, in some areas, ground slope can be significant, which might need to be considered in the analysis as it can affect forest backscatter.

5.3 Airborne SAR Data Acquisition

An airborne system, ONERA SETHI, was used for SAR data acquisition in the BioSAR-3 campaign [13]. This SAR sensor was different from E-SAR used in the BioSAR-1 campaign. On September 23, 2010, airborne SAR data were collected by this system, and included ten flight tracks and three headings. The data were acquired using P- and L-band polarimetric and repeat-pass interferometric modes. The data for seven of these imaging passes were acquired with the two flight headings 178° and 199°. These two flight headings were the same as in the previous BioSAR-1 campaign. A new flight heading of 270° covering a larger part of the test site was used for the remaining three passes. Table 2 summarizes the system parameters used for both radar bands during BioSAR 2010.

Table 2: System parameters for SETHI used during the BIOSAR-3 campaign [13].

Parameter	P-Band	L-Band
Geometry		
Altitude [ft/m]	13000/3962	13000/3962
Velocity[m/s]	120	120
Antenna		
Elevation Aperture[⁰]	100	20
Azimuth Aperture[⁰]	60	16
Waveform		
Mode	Full-Polar	Full-Polar
Peak Power [W]	500	200
actual PRF[kHz]	2.5	5
Sampling rate [MHz]	500	500
Bandwidth [MHz]	260-460	1250-1400
Processed wave length [m]	0.676-1.082	0.214-0.24
Processed bandwidth [MHz]	277-443	1250-1400
Relative bandwidth[%]	46	11
Range resolution [m]	0.78	0.92
Azimuth resolution [m]	0.79	0.92
Range pixel spacing [m]	0.55	0.75
Azimuth pixel spacing [m]	0.55	0.75
Near range [m]	4350	4350
Number of pixels in range	7251	2600
Incidence angle range[⁰]	24-62	24-47

Out of these ten passes, six passes were selected for the precision processing and calibration. This resulted in the following database which is then used for the subsequent data analysis.

- 1) Two PolInSAR pairs (headings 199°, 270°) suitable for forest height retrieval.
- 2) Three SAR images (headings 178°, 199° and 199°) suitable for change analysis with E-SAR data from 2007.
- 3) One SAR image (heading 178°) suitable for calibration analysis based on two in-scene large (5.15 m) corner reflectors.

Out of these six passes, three are used in this thesis for the forest structure assessment. Table 3 shows the SETHI data acquisitions selected.

Table 3: Selected SETHI data acquisitions for the thesis work [13].

Pass	Heading	Mode	Altitude (ft)
Bio01	199 ⁰	P+L full polar	13253
Bio05	178 ⁰	P+L full polar	13253
Bio07	270 ⁰	P+L full polar	13253

Successful processing and calibration was done of both L- and P-band data from the six selected passes. Using the available digital elevation model, all the single look complex P- and L-band data are projected into a geographic projection in WGS84.

5.4 Reference Biomass Data

Biomass data corresponding to each stand is available in the form of a biomass map, which was developed using the extensive ground data set. This map contains above ground biomass value in tons per hectare for each stand. This biomass map has been used as a reference in this work during the modeling of biomass.

5.5 MATLAB Program Flow

Figure 6 shows the flow of data processing in MATLAB for the computation of scattering parameters for three decomposition theorems.

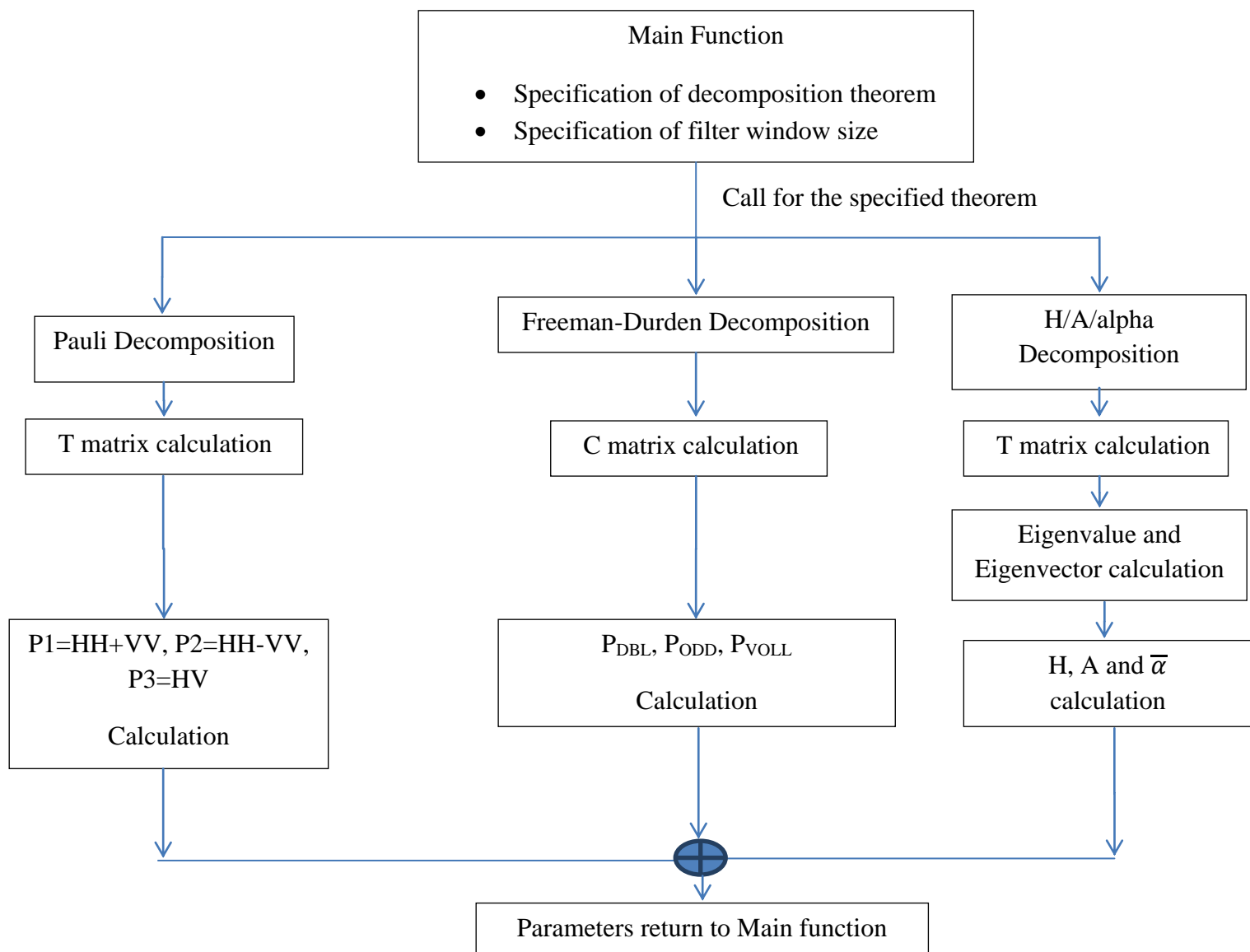


Figure 6: Flow of data processing in MATLAB for the computation of scattering parameters for three decomposition theorems.

6. Results and Discussion

6.1 Heading Bio01

Figure 4 shows the aerial image of actual Remningstorp test site that has been taken during the same year as that of the campaign. The image covers approximately the same area as that of the heading Bio01. As can be seen in the image, the test site mainly consists of a forested area, two large lakes and a power line passing through it. As shown in Figure 5, the forest is divided into 665 stands. It also contains number of small lakes and manmade structures such as houses, fields etc. The important manmade structures deployed on the test site are two large trihedral corner reflectors. Position of these reflectors is shown in Figures 7 and 8. These two of four reflectors were used for the calibration of the Japanese Advanced Land Observing Satellite (ALOS) [13].

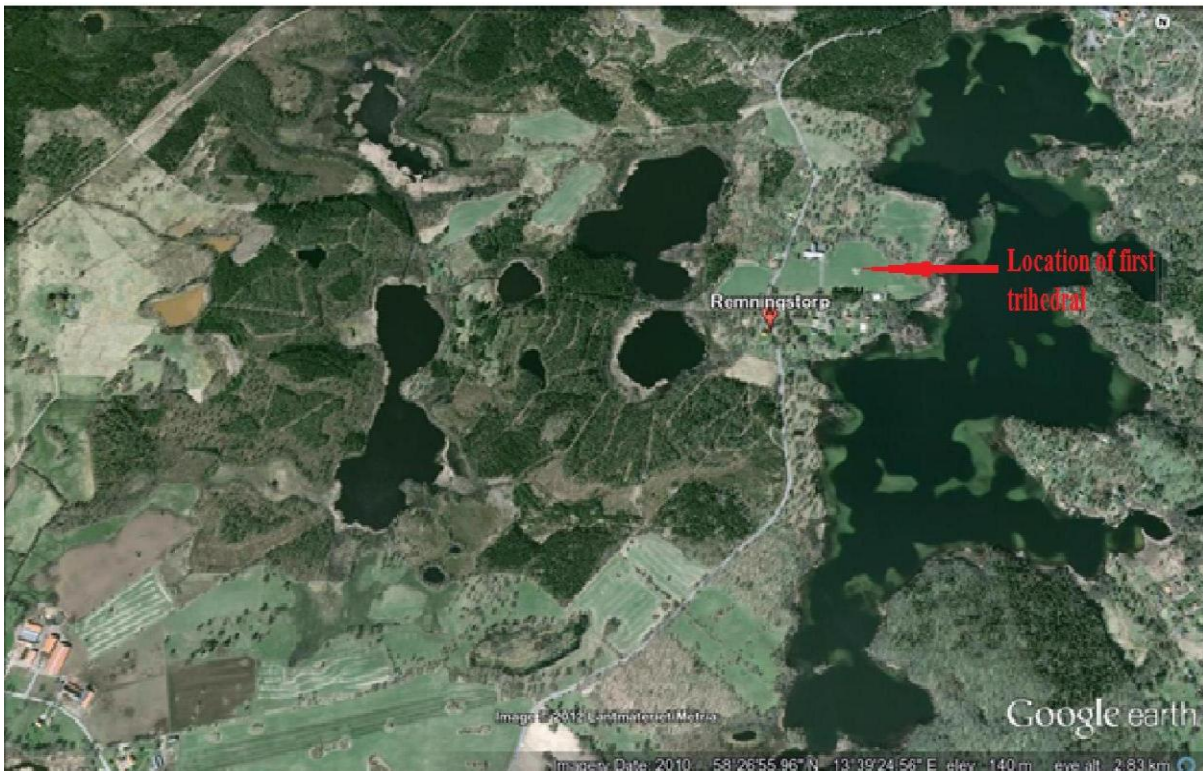


Figure 7: Aerial image showing the position of first trihedral corner reflector [14].



Figure 8: Aerial image showing the position of second trihedral corner reflector [14].

6.2. Decomposition Results

6.2.1 Pauli Decomposition:

As explained in Section 4.1, the Pauli decomposition gives coherent decomposition of the three scattering mechanisms for the monostatic case. Heading Bio01 data has been decomposed using the Pauli decomposition. Figures 1-6 in Appendix 1 show three Pauli decomposition components for P-band and L-band. Figures show the different scattering mechanisms occurring over the test site. Difference in the scattering phenomenon at P-band frequency and L-band frequency over the same region can be easily noted. P-band frequency having the longer wavelength penetrates deeper into the scatterer. On the other hand, L-band having the shorter wavelength is more sensitive to the small surface variations. This is explained in details below. Figure 10 and Figure 11 represent a color-coded Pauli image for P-band and L-band respectively, with color coding as Red: $|HH-VV|$, Green: $|HV|$ and Blue: $|HH+VV|$. Figure 9 shows the RGB color coding used. Combination of red, green and blue color results in another color as shown [19].

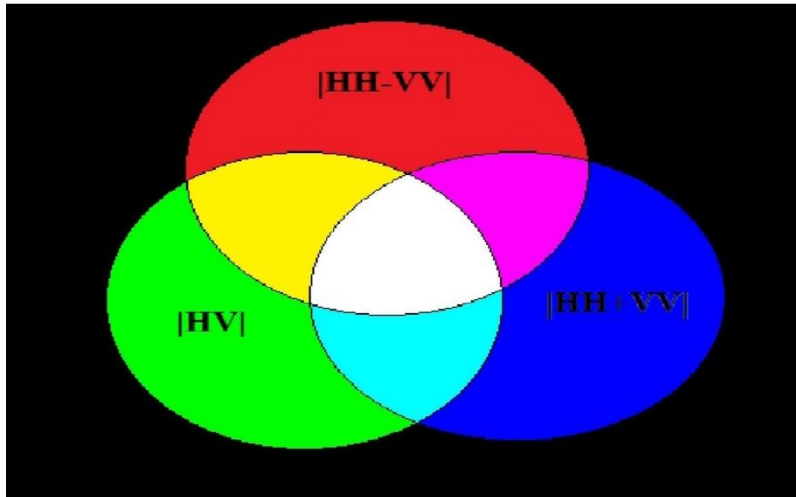


Figure 9: Color coding for Pauli Decomposition

As can be seen in Figure 10 and 11, due to the antenna positions on an airborne platform and due to the imaging geometry, the L-band image covers less area than the P-band image. The two images differ in various aspects. The forested area is mostly represented by green color in the L-band image, whereas it is a mixture of green and red color in the P-band image. This difference mainly occurs because of the fact that the P-band has a longer wavelength than that of the L-band. Longer wavelength signal penetrates deeper into the scatterer. This causes the difference in the types of scattering processes occurring at two bands. The L-band signal cannot penetrate through the forest canopy because of its shorter wavelength. On the other hand, the P-band signal penetrates through the forest canopy because of its longer wavelength and interacts further with the tree trunk and ground. Thus, L-band is more sensitive to forest canopy whereas P-band images forest canopy as well as double bounce scatter from ground-trunk (or trunk-ground) of the tree.

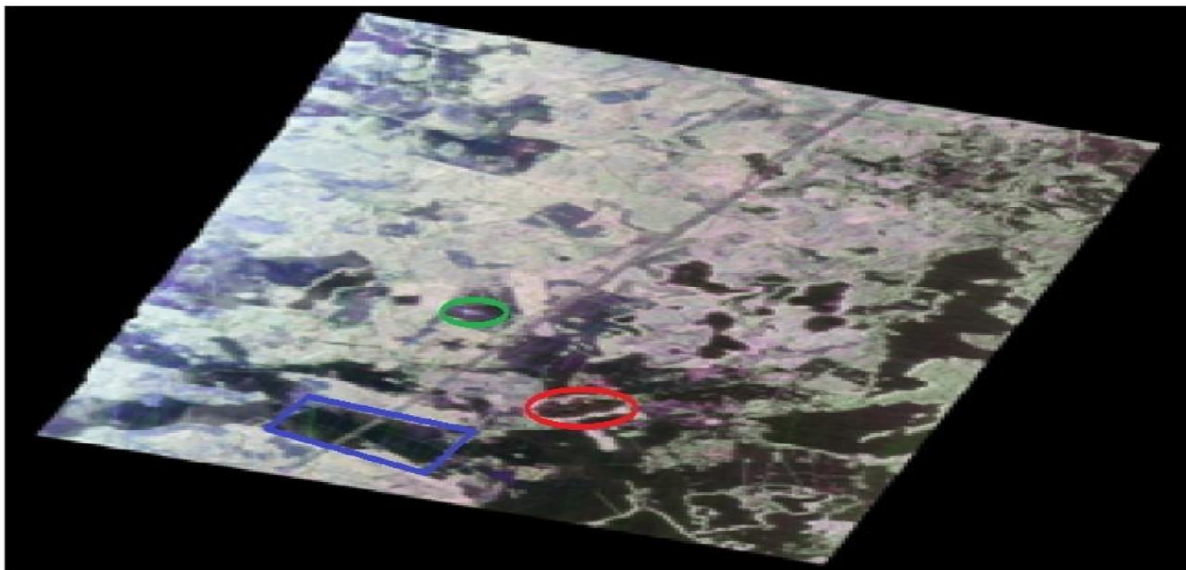


Figure 10: P-Band Pauli RGB image

Image color coded as Red: $|HH-VV|$, Green: $|HV|$ and Blue: $|HH+VV|$

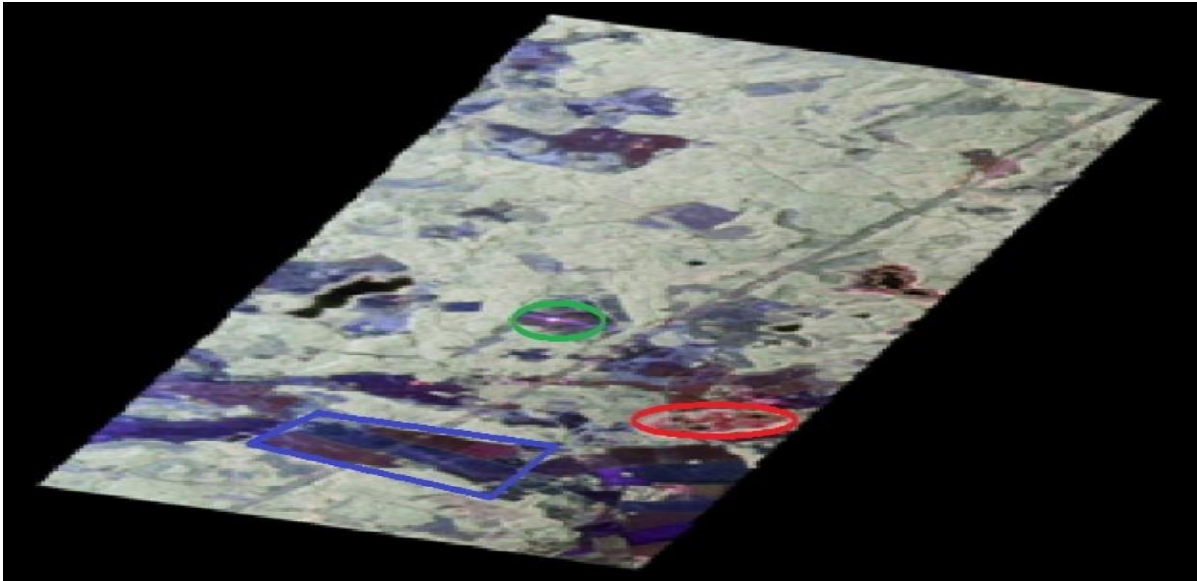


Figure 11: L-Band Pauli RGB image

Image color coded as Red: $|HH-VV|$, Green: $|HV|$ and Blue: $|HH+VV|$

Different scattering phenomena for two bands over the same region can also be seen at other regions. For example, the region encircled in red in Figures 10 and 11 show that the L-band signals undergo double bounce scattering over a whole region where P-band signals undergo double bounce scattering only at the outer edges of the same region. Figure 12 shows the aerial image of that region, which is a small dip containing some water and some vegetation in it. Also, major difference can be seen at the regions where fields and clear cuts are present. This region is enclosed in blue rectangles in Figures 10 and 11. L-band image distinctly shows the double and odd bounce scattering over the harvested and empty fields respectively, as compared to P-band image. Figure 13 shows the actual image of the fields. As it can be seen, at L-band double bounce scattering takes place at harvested fields whereas single bounce scattering takes place at empty fields because of the short wavelength of the L-band signal. Figures 10 and 11 also show the high backscatter from the trihedral reflector caused by the odd bounce. The backscatter is stronger in case of L-band. Besides the strong reflection from trihedral reflector, there is also another strong reflection shown in the Figures 10 and 11 by green circle. If we look at the aerial image, Figure 14, we can infer that it comes from some manmade objects placed at that location. The lakes in both P- and L-band images show very low back scatter due to specular reflections of radar signals. Buildings, wherever present, cause odd or even bounce scattering together with the ground, depending upon their structure. As a result, they give backscatter in blue or red channel. Backscatter for this case is also stronger for L-band. The Figures 10 and 11 also show the effect of imaging geometry i.e. change in the scattering mechanism with the incidence angle. At low incidence angles (left edge of each image), odd bounce scattering dominates over the large incidence angle, thus representing more blue colored regions. However, at the large incidence angles (right side of each image), double bounce scattering and volume scattering dominates representing more red and green regions depending upon the scatterer.



Figure 12: Aerial image of the small crater [14].



Figure 13: Aerial image of the fields [14].



Figure 14: Aerial image of the manmade scatterer [14].

6.2.2 Freeman-Durden Decomposition:

As explained in the Section 4.2, Freeman Durden three component decomposition gives three component scattering mechanism model. Heading Bio01 data have been decomposed using Freeman- Durden three component decomposition. Figures 9-14 in Appendix 1 show three Freeman-Durden decomposition components for P-band and L-band. Similar to the Pauli decomposition component images, difference in scattering mechanism over the same region for two different frequencies can be seen in these images. Presence of more odd and double bounce scatter at P-band can be clearly seen.

Figure 16 and 17 shows the Freeman-Durden RGB images for P-band and L-band respectively. The Images are color coded as Red: Double bounce scattering, Green: Volume scattering, and Blue: Odd bounce scattering. Figure 15 shows the RGB color coding used.

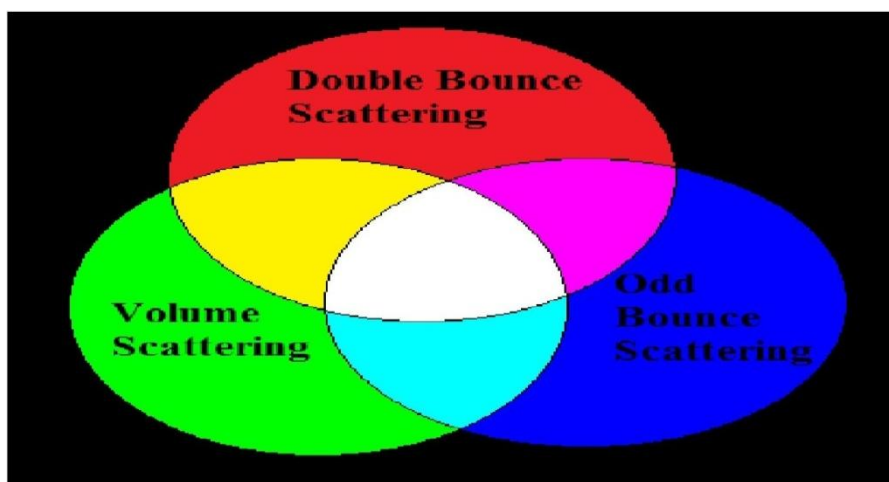


Figure 15: Color coding for Freeman-Durden Decomposition

As can be seen from the Figures 16 and 17, all the features described in the Pauli decomposition are also represented by the Freeman-Durden decomposition. However, Freeman-Durden decomposition provides better understanding of dominant scattering mechanism. In case of the P-band image, dominance of volume scattering and double bounce scattering from ground-trunk or trunk-ground reflection over forested area can be clearly seen. The non-forested areas such as fields, empty lands can be clearly distinguished by the odd bounce scattering represented by the blue color. However difference between harvested and empty fields is subtle at P-band. In case of the L-band image, forested areas can be easily distinguished by the dominance of volume scattering represented by green color. Due to less penetration, as explained earlier, L-band images forest canopy and thus represents forested area completely by green color. The difference between harvested and empty fields can be seen better at the L-band as it maps roughness due to shorter wavelengths.

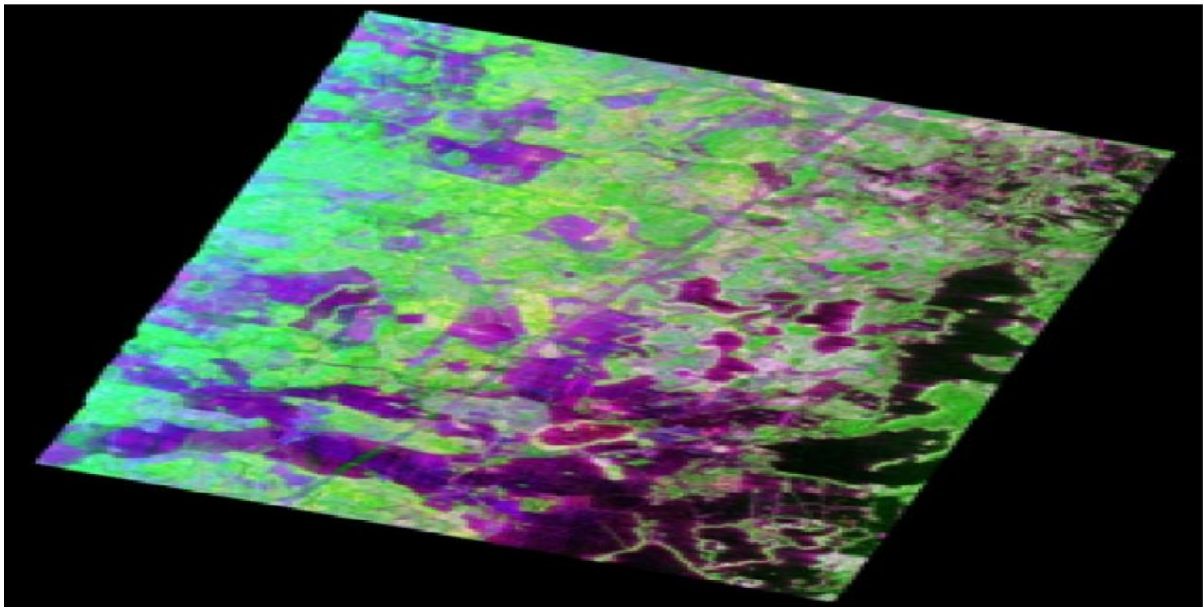


Figure 16: P-Band Freeman-Durden RGB image

Image color coded as Red: Double bounce scattering, Green: Volume scattering, and Blue: Odd bounce scattering

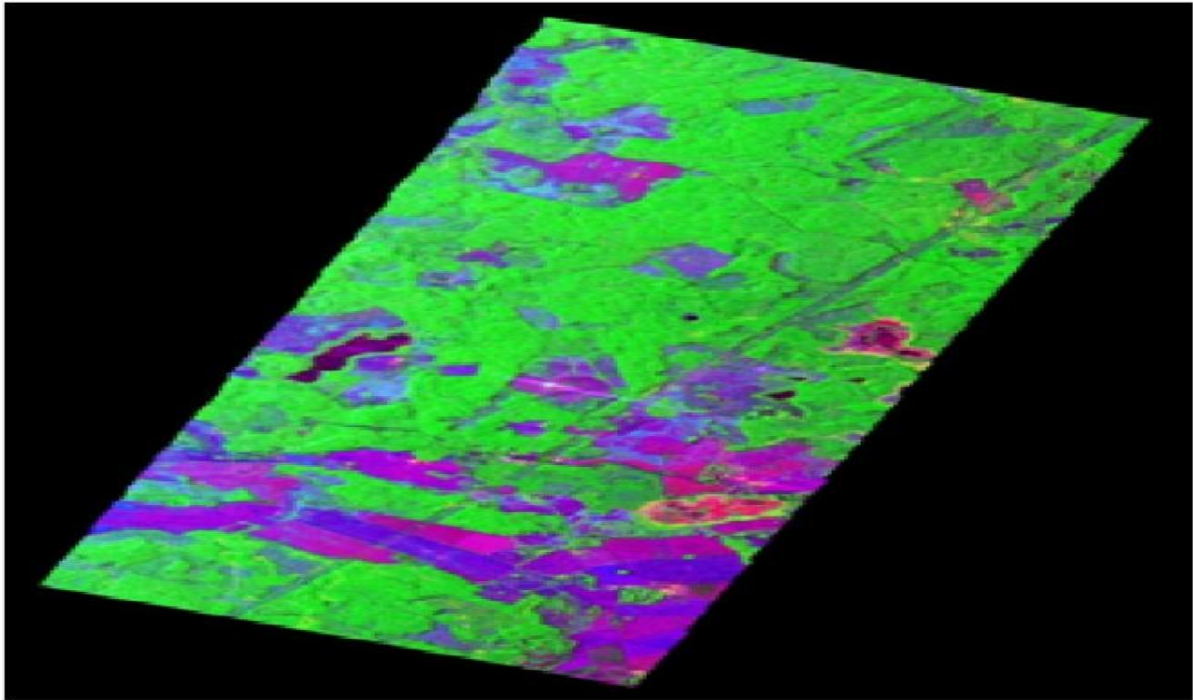


Figure 17: L-Band Freeman-Durden RGB image

Image color coded as Red: Double bounce scattering, Green: Volume scattering, and Blue: Odd bounce scattering

In overall comparison, the Freeman-Durden decomposition method provides better visual classification than the Pauli decomposition. Freeman-Durden decomposition provides more realistic representation with sharper details as it is based on the scattering models with dielectric surfaces. Freeman-Durden decomposition is thus useful to discriminate between forested and deforested areas [6]. Pauli decomposition is a type of coherent decomposition. Coherent decomposition results are affected by the use of 3×3 coherency, T_3 , or covariance, C_3 , matrix. The results of coherent decompositions are thus affected by the use of averaging, which is used to reduce the effect of speckle noise. Coherent decomposition theorems are useful in the case of high resolution, low-entropy scattering problems where only one dominant target component is expected.

6.2.3 H/A/alpha decomposition:

As explained in the Section 4.3, H/A/alpha decomposition provides information about the type of scattering process by parameters, entropy, H , and anisotropy, A , as well as information about the underlying physical scattering mechanism by parameter mean alpha angle $\bar{\alpha}$. Heading Bio01 data has been decomposed using H/A/alpha decomposition theorem. Figures 17-22 in Appendix 1 show three H, A and $\bar{\alpha}$ components for P-band and L-band.

The P-band entropy component figure, Figure 17 Appendix 1, shows that the low to moderate entropy occurs over the surface of lakes in case of P-band. On the other hand, the same region in Figure 18 Appendix 1 shows low entropy in the case of L-band. Entropy for L-band is also low over the regions of fields. The reason behind that is L-band frequency,

because of its shorter wavelength, is more sensitive to slightly rough surfaces as mentioned earlier. The low value of entropy indicates weakly depolarizing system and indicates the possible presence of an identifiable equivalent point scatterer. On the other hand, moderate to high entropy occurs over the forested region in the case of P-band, representing an ensemble of depolarizing scatterers. Thus, in this case, different scattering types must be considered. This is in agreement with the previous results, as in P-band multiple scattering processes occur due to its deeper penetration.

The P-band anisotropy component, Figure 19 Appendix 1, shows that the low anisotropy occurs over the surface of lakes, which represents the presence of either single dominant mechanism or presence of random scattering. Latter is true in this case as the signals are reflected specularly over the surface of lake away from the radar. High anisotropy occurs over the regions of fields in case of the L-band, which indicates the presence of second scattering mechanism. This can be seen in Figure 20 Appendix 1. Medium to high anisotropy also occurs over the manmade structures.

The P-band $\bar{\alpha}$ component figure, Figure 21 Appendix 1, shows medium and high values of $\bar{\alpha}$ ($45^\circ < \bar{\alpha} < 90^\circ$) over the region of forest. The large value of $\bar{\alpha}$ indicates the presence of single and double bounce scattering mechanism. Again, the presence of different scattering mechanisms for P- and L-band over the same region can be seen. In case of L-band, as can be seen in Figure 22 Appendix 1, fields show low value of $\bar{\alpha}$ indicating the surface scattering.

Thus, the parameter $\bar{\alpha}$ represents the underlying average physical scattering mechanism and the parameters entropy, H, and anisotropy, A, represent the randomness of scattering.

6.3 Biomass Modeling

One of the tasks in radar polarimetry application to forestry is the modeling of biomass in terms of the backscattering coefficient. Some of the backscattering coefficients are well correlated with the forest biomass while others are not. The extent of correlation mainly depends upon the type of forest, forest structure, tree species, terrain topography, and radar system specifications including imaging geometry. These factors in turn affect the accuracy of estimation of biomass because of the inconsistent modeling of biomass in terms of the backscattering coefficient. One model created for one forest may not find applicable for the other. This makes biomass modeling complex and potentially inaccurate. In this thesis, use of one such model using linear regression is described. The model is developed by relating backscattering coefficient with the above ground biomass (AGB) information available for each stand. The model defines estimated biomass in terms of the backscattering coefficient as [16]:

$$\log(\text{Biomass}) = a_1(\text{Backscattering Coefficient})_{dB} + a_2, \quad (6.1)$$

where a_1 and a_2 are constants.

As shown in Figure 18, Remningstorp forest test site is divided into 665 stands spread over all the area. Each of these stands is represented by a different color. However, each flight heading, encompassing limited area, does not cover all these stands. So in the modeling, it is required to filter out the stands which are not covered by that particular heading. Figure 19 shows the stands covered by Heading Bio01.

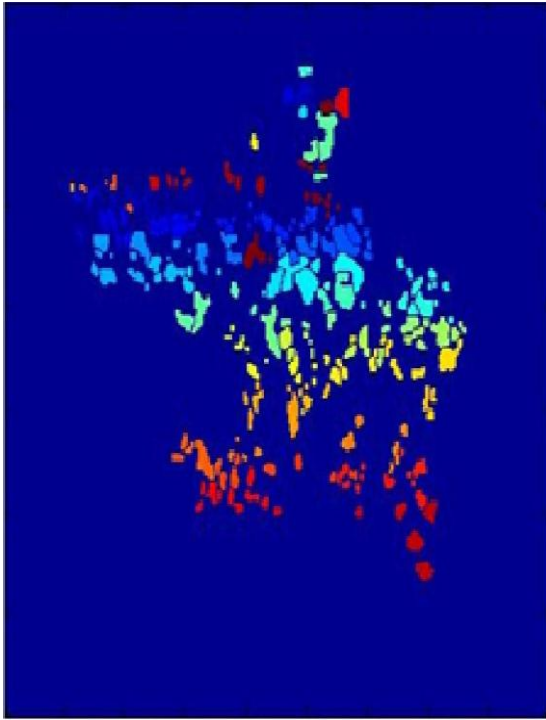


Figure 18: Total stands over test site

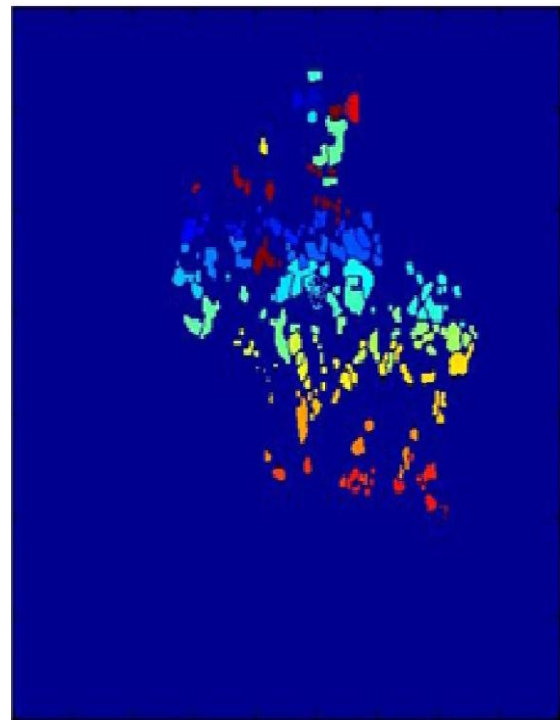


Figure 19: Stands covered by heading Bio01

Figures 23-33 and 34-44 in each appendix show the plots of different backscattering coefficients against the reference biomass for P- and L-band data respectively. Some coefficients show the wide spread around the fitted line. On the other hand, some parameters lie in the close vicinity of the fitted line and thus possess a good statistical relation and correlation with the reference biomass. The model, which estimates the biomass in terms of the backscattering coefficient, can then be developed. One such model is given by equation (6.1). The coefficients which possess good correlation with the reference biomass are suitable for modeling. Tables B-2 and C-2 in each appendix show the value of correlation between backscattering coefficient and reference biomass, root mean square error in tons/ha, and model parameters for P- and L-band data respectively. In case of the P-band data, polarimetric scattering mechanism type indicator $|\delta|$ is most correlated with the reference biomass. While in the case of L-band, $|\text{HH-VV}|$ is sensitive to biomass. Biomass estimation model corresponding to parameter $|\delta|$, in case of P-band, and parameter $|\text{HH-VV}|$, in case of L-band, shows the lowest root mean square error of the order of 35-50 tons/ha, for all flight headings.

6.4 Discussion on Biomass Modelling Results

Equation (6.1) represents a simple biomass retrieval linear regression model. Biomass is estimated by fitting the reference biomass data and radar backscattering coefficients to this model. The terrain topography, different tree structures, environmental factors, and radar imaging geometry are the possible factors affecting the results of biomass retrieval model [15]. The error is introduced due to the dependence of radar backscatter on the incidence angle. This error can be minimized by using the parameter γ^0 in the retrieval model instead of σ^0 . The two parameters are related by, $\gamma^0 = \frac{\sigma^0}{\cos \theta_i}$, where θ_i is the local incidence angle. Radar backscatter is also affected by the dependence of different scattering mechanisms on incident angle and terrain topography. Local moisture conditions, species distribution, tree density, and forest structure also affect the radar backscatter. At lower biomass values, most of the backscatter contributions come from surface scattering. This backscatter also contains information about the soil moisture and surface roughness.

A valid biomass retrieval algorithm must compensate for the errors introduced by these factors. Further research is required to investigate and quantify how strongly the relationship between AGB and radar backscatters is affected by these factors as well as to develop more sophisticated model to estimate AGB accurately.

6.5 Heading Bio05 and Heading Bio07

Analysis of data for Heading Bio05 and Heading Bio07 can be carried out similarly as for Heading Bio01. All the results, for decomposition theorems and for biomass modeling, for Heading Bio05 and Heading Bio07 are included in Appendix 2 and Appendix 3, respectively. Results for Heading Bio05 and Heading Bio07 show that each heading provides additional information about the test site.

6.6 Effect of heading on scattering mechanism

The type of scattering mechanism occurring at the scatterer can be different for different radar flight directions. As the radar flight direction changes, the geometry of the scatterer seen by the radar also changes. This causes change in the radar backscattering and change in the type of scattering mechanism. Figure 20 and 21 shows P-band Freeman-Durden RGB images of the common region covered by Heading Bio01 (199°) and Heading Bio07 (270°) respectively.

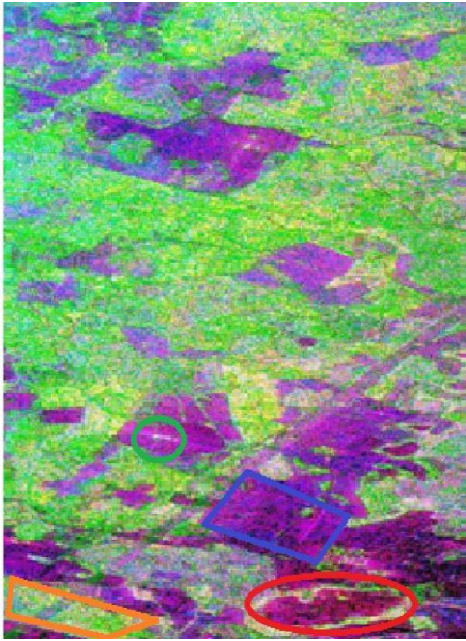


Figure 20: Part of P-band Heading Bio01
Freeman-Durden RGB image

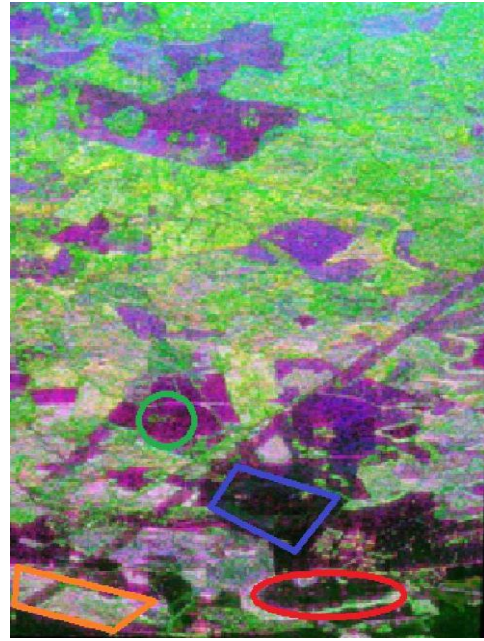


Figure 21: Part of P-band Heading Bio07
Freeman-Durden RGB image

In Figure 20 and 21, effect of flight heading on the scattering mechanism over the same region can be clearly seen. The region marked by the red circle in both the images is the small crater containing some water and vegetation. Change in the flight direction causes different type of scattering mechanism to take place over this region. In Figure 20, this region shows scattering in red channel representing double bounce scattering from the edges of the crater. The same region for Heading Bio07 shows very low back scatter due to specular reflection. Green circle shows the location of some manmade object. This object gives strong reflection in Heading Bio01. While in Heading Bio07, there is no reflection from this object and it is completely missed by the radar. The difference in scattering mechanism over the regions of fields and forests is also notable. This is shown by blue and orange boxes, respectively. For Heading Bio01, fields show more surface scattering in blue channel. On the other hand, in the case of Heading Bio07, fields show very low backscatter. Forested region, shown in orange box, shows more double bounce scattering in Heading Bo07 while, more volume scattering in Heading Bio01. Thus, the radar flight heading has the prominent effect on the scattering mechanism occurring at the scatterer. One object present in one heading could be completely missed by the radar in other heading. Change in the scattering mechanism also has an effect on biomass modeling. Same backscattering coefficient shows different correlation with the reference biomass for different headings. This can be seen in Figures (23-33 and 34-44 in each appendix) and Tables (B-2 and C-2 in each appendix). Thus, to get the complete picture of region of interest, data from multiple headings should be used.

7. Conclusions

SAR polarimetry plays an important role in forest structure assessment and in biomass estimation. Scattering processes occurring over a region of interest can be understood with the use of target decomposition theorems, when applied to the polarimetric data corresponding to that region. These scattering processes help to understand the forest structure. Each target decomposition theorem provides information about the scatterer in unique way. Out of the three decomposition theorems studied, Freeman-Durden decomposition provides better visual classification, as it is based upon the scattering models with dielectric surfaces. Freeman-Durden decomposition provides sharper details of scatterers and thus is useful to study the forest structure.

Scattering processes show dependence on:

- 1) Signal frequency: The smaller the frequency of the signal, the longer is the wavelength. Thus, signal penetrates deeper into the scatterer. This causes scattering mechanism to take place that is different than the one that would take place in the case of the shorter wavelength signal. Out of the two frequency bands used in this work, P-band has a longer wavelength and thus penetrates deeper beyond the forest canopy. This signal after penetrating canopy interacts with the stem structure in two ways: first, ground-trunk (or trunk-ground) reflection giving rise to double bounce scatter and second, reflection directly from the stem giving rise to single bounce scatter. On the other hand, L-band signal has a shorter wavelength. Thus, signal scatters mostly from forest canopy. P-band signal thus maps more biomass than L-band signal as, the biomass is primarily stored in the stem structure;
- 2) Incidence angle: Due to the imaging geometry, incidence angle varies across the swath. This results in different scattering mechanisms to take place across the swath. More ground contribution is seen for lower incidence angles as, the signal undergoes more surface scattering in this case;
- 3) Flight heading: Different scattering mechanism takes place over the same region for different flight headings. Thus, one scatterer present in one heading can be absent in another flight heading. Thus, to understand the complete picture of the region, data from multiple headings should be used.

Biomass can be estimated by developing a model based on a linear regression analysis of different decomposition products. Results for P-band data show that of all studied parameters, the parameter $|\delta|$, which is a sensitive indicator for the amount of ground scattering visible, is best correlated with reference biomass. On the other hand, results for L-band data show that of all studied parameters, the parameter $|HH-VV|$ is best correlated with reference biomass. Biomass estimation model corresponding to parameters $|\delta|$, in case of P-band, and parameter $|HH-VV|$, in case of L-band, shows the lowest root mean square error of the order of 35-50 tons/ha, for all flight headings. The root mean square error can be further reduced by modeling the biomass using more sophisticated models that take into account ground topography, soil moisture, and forest structure.

8. References

- [1] “Global Forest Resources Assessment 2005”, Food and Agriculture Organization of the United Nations, 2006.
- [2] K.E. Skog and J.A. Stanturf, “Forest Biomass Sustainability and Availability”, American Chemical Society, ACS Symposium Series, Chapter 1, 2011.
- [3] R.A. Houghton, “Aboveground Forest Biomass and the Global Carbon Balance”, *Global Change Biology*, vol.11, page 945-958, June 2005.
- [4] M. Neumann, S.S. Saatchi, L.M.H. Ulander, and J.E.S. Fransson, ”Assessing Performance of L- and P-Band Polarimetric Interferometric SAR Data in Estimating Boreal Forest Above-Ground Biomass”, *IEEE Transactions on Geoscience and Remote Sensing*, vol. 50, no. 3, page 720, March 2012.
- [5] W.-M. Boerner, *Basic Concepts In Radar Polarimetry*, PolSARPRO v3.0 Lecture Notes.
- [6] J.S. Lee, E. Pottier, *Polarimetric Radar Imaging From Basics to Applications*, CRC Press, 2009.
- [7] M.I. Skolnik, *Introduction to Radar Systems*, 3rd edition, McGraw-Hill, 1981.
- [8] R.J. Sullivan, *Radar Foundations for Imaging and Advanced Concepts*, SciTech Publishing, 2009.
- [9] “IEEE Standard Letter Designations for Radar-Frequency Bands”, IEEE Std 521-2002, 2003.
- [10] C. Nordling, *Physics Handbook for Science and Engineers*, Chartwell-Bratt Ltd., 1996.
- [11] H. Meikle, *Modern Radar System*, 2nd edition, Artech House, 2008.
- [12] B. Mahafaza, *Radar Systems Analysis and Design using MATLAB*, Chapman & Hall/CRC, 2000.
- [13] L.M.H. Ulander et al., “BioSAR2010 Technical Assistance for the Development of Airborne SAR and Geophysical Measurements during the BioSAR2010 Experiment Final Report”, version 1.0, Prepared by Swedish Defence Research Agency (FOI) and office d’Études et de Recherches Aérospatiales (ONERA), 2011.
- [14] ©Photo: Google Earth.
- [15] M.J. Soja, “Modelling and Retrieval of Forest Parameters from Synthetic Aperture Radar Data”, Thesis for the Degree of Licentiate of Technology, Chalmers University of Technology, Gothenburg, Sweden, 2012.
- [16] L.M.H. Ulander, G. Sandberg, and M.J. Soja, “Biomass Retrieval Algorithm Based on P-Band BioSAR Experiments of Boreal Forest”, *IEEE International Geoscience and Remote Sensing Symposium*, July 2011.
- [17] European Space Agency, “Radar Course II”
http://earth.esa.int/applications/data_util/SARDOCS/spaceborne/Radar_Courses/Radar_Course_II/
- [18] C. Wolff, “Radartutorial”, <http://www.radartutorial.eu/20.airborne/>, January 2013
- [19] Wikipedia Encyclopedia, <http://en.wikipedia.org/>, January 2013.

Appendix 1

Appendix 1 includes the results of decomposition algorithms and of biomass modeling for Heading Bio01.

A. Decomposition Results for P- and L-Band:

A.1. Pauli Decomposition:

P-Band	L-Band
--------	--------

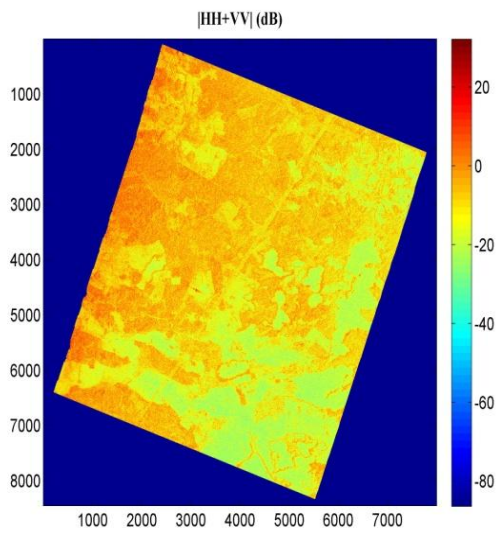


Figure 1

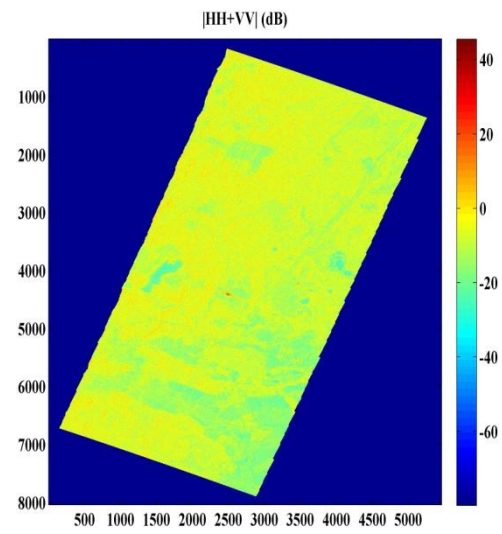


Figure 2

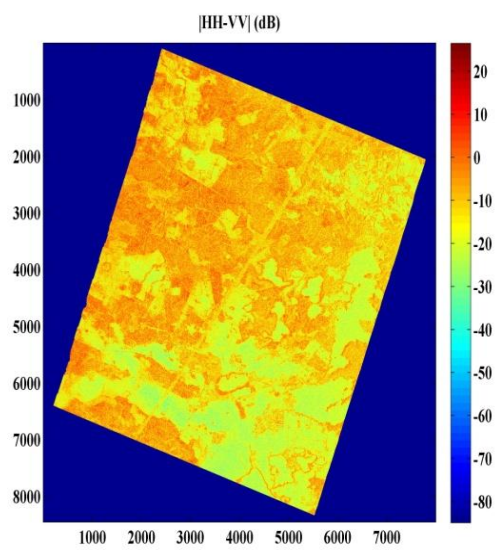


Figure 3

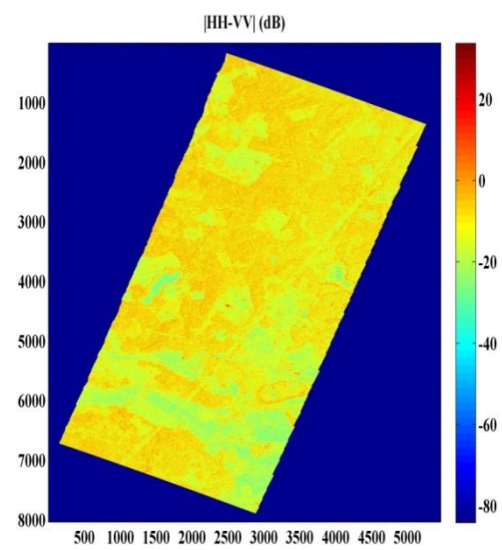


Figure 4

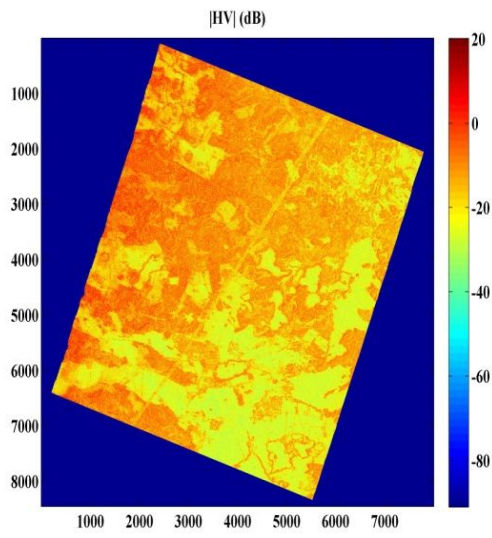


Figure 5

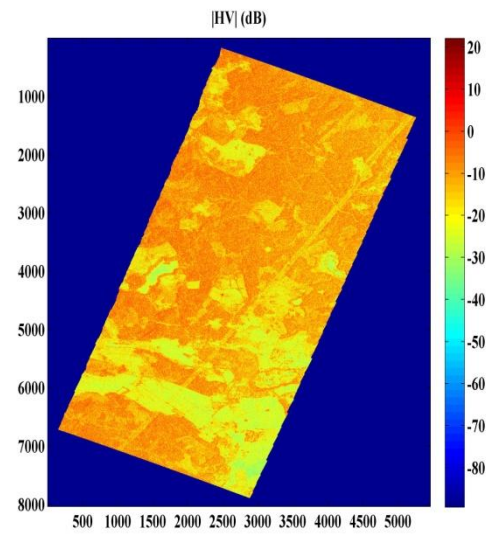


Figure 6

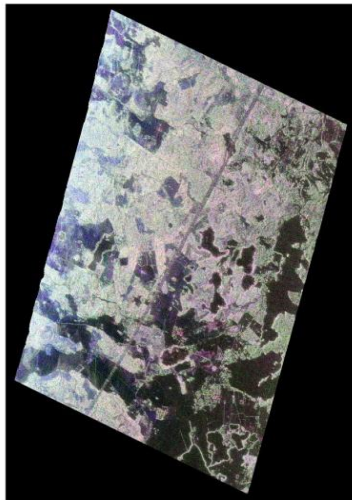


Figure 7



Figure 8

Pauli RGB image

Image color coded as Red: $|HH-VV|$, Green: $|HV|$, and Blue: $|HH+VV|$

A.2. Freeman-Durden Three Component Decomposition:

P-Band

L-Band

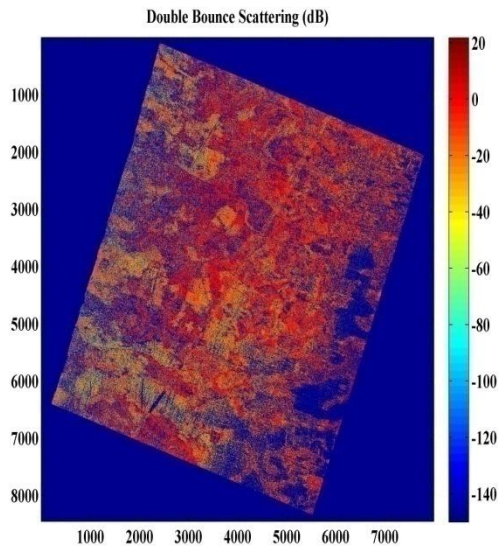


Figure 9

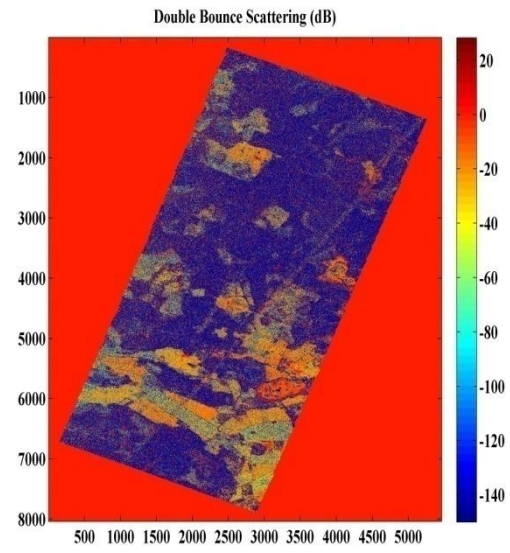


Figure 10

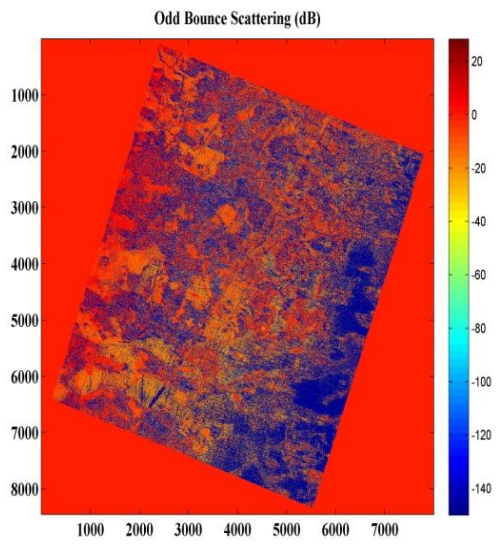


Figure 11

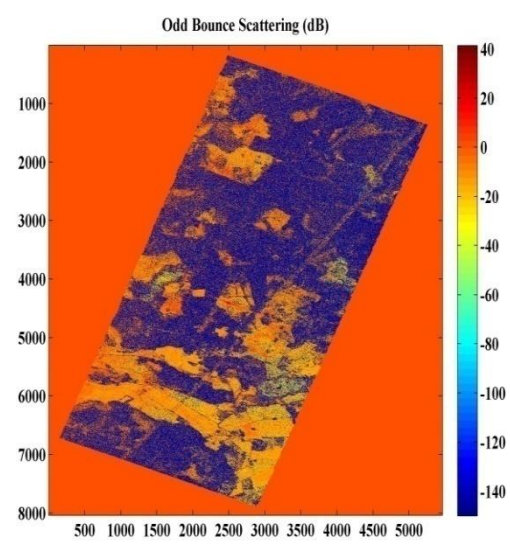


Figure 12

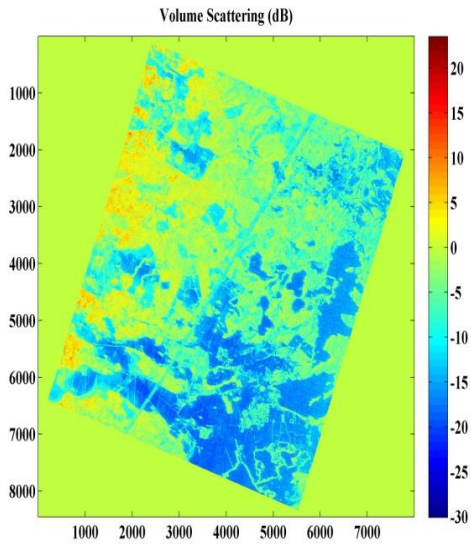


Figure 13

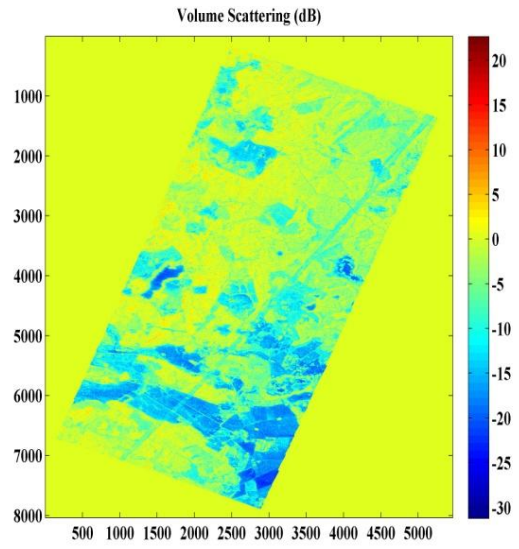


Figure 14

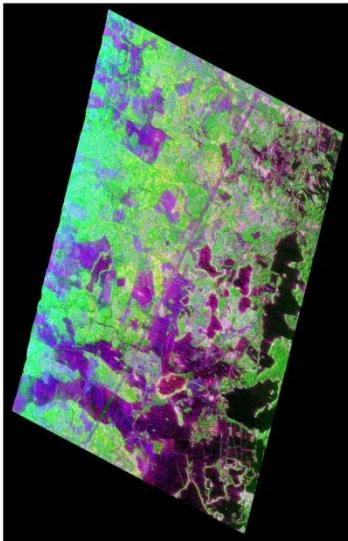


Figure 15

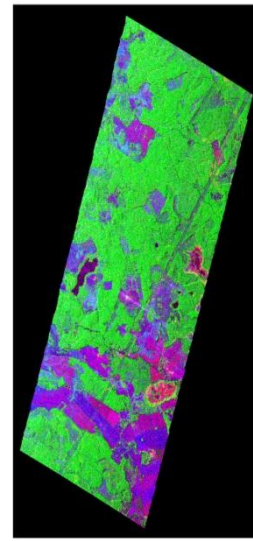


Figure 16

Freeman-Durden RGB image

Image color coded as Red: Double bounce, Green: Volume scatter, and Blue: Odd bounce

A.3. H/A/alpha Decomposition:

P-Band

L-Band

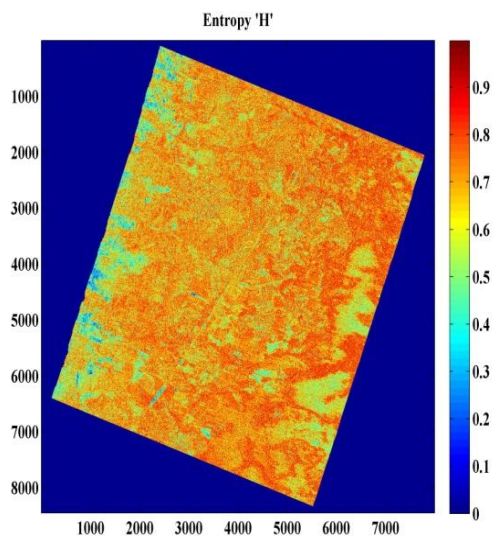


Figure 17

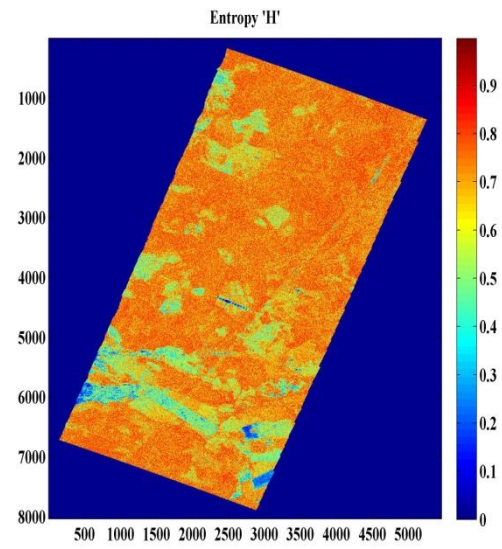


Figure 18

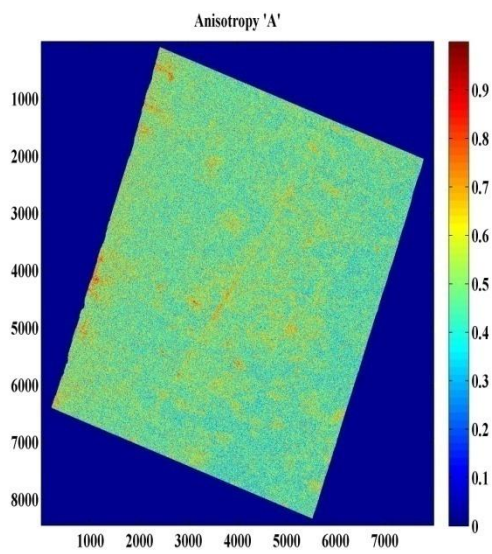


Figure 19

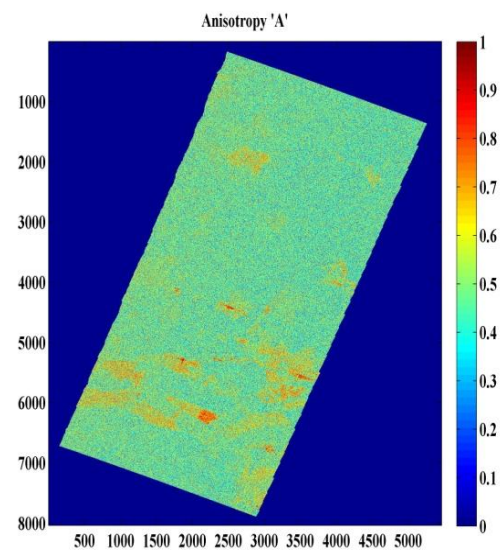


Figure 20

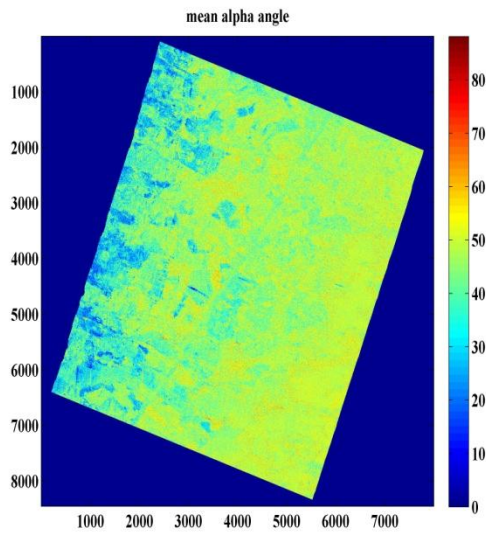


Figure 21

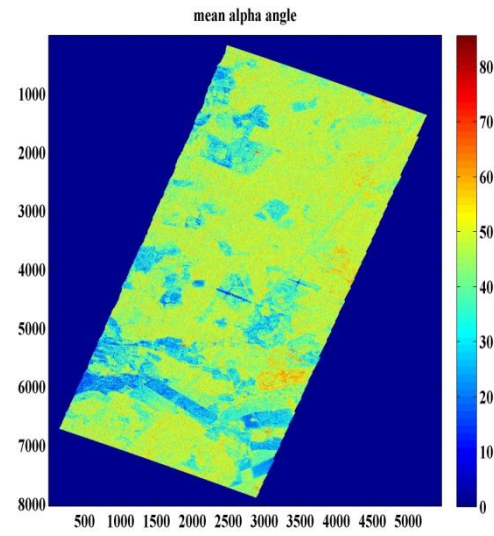


Figure 22

B. P-band Biomass modeling results:

B.1 Plots of Backscattering Coefficient vs. Reference Biomass:

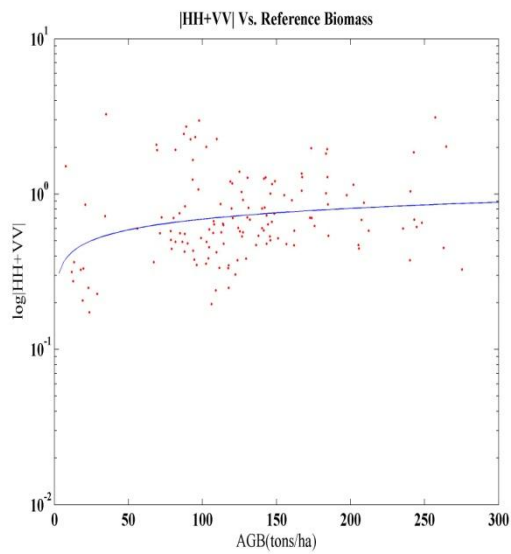


Figure 23

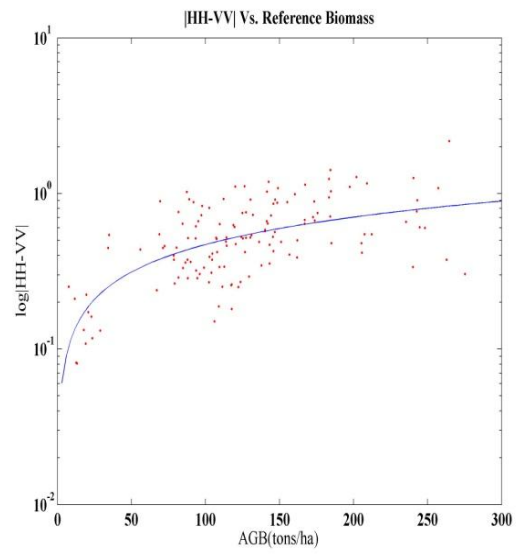


Figure 24

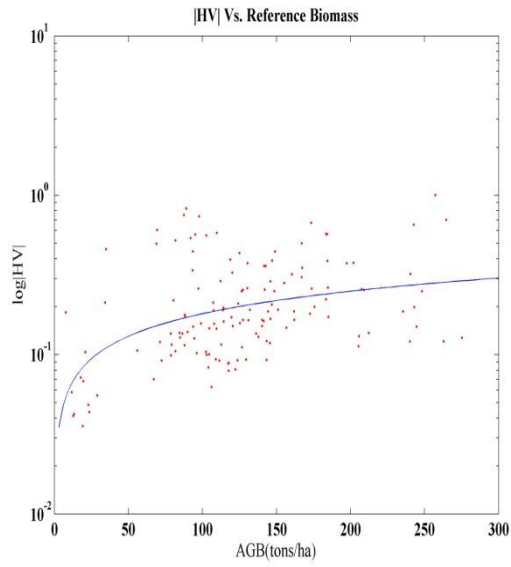


Figure 25

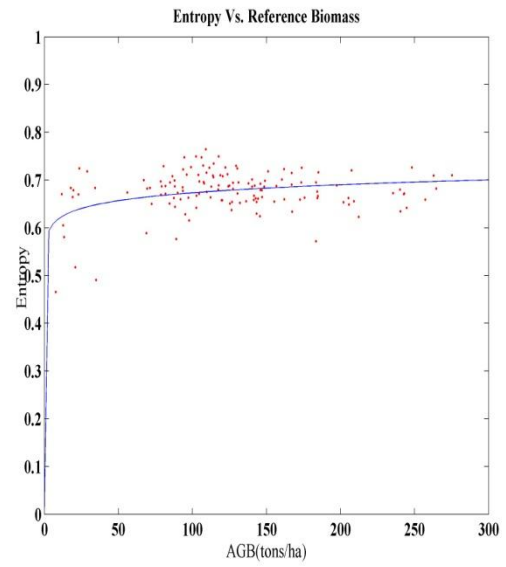


Figure 26

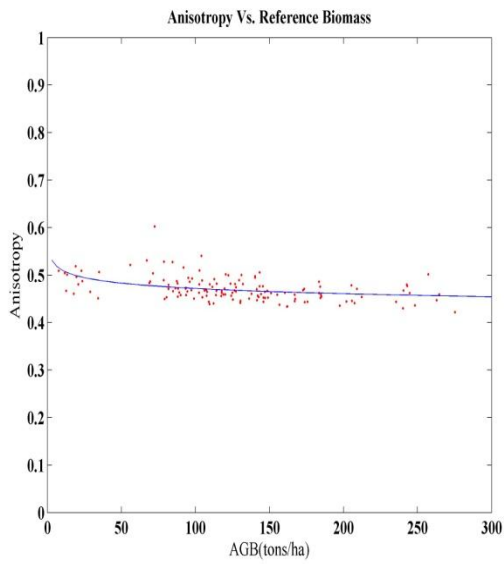


Figure 27

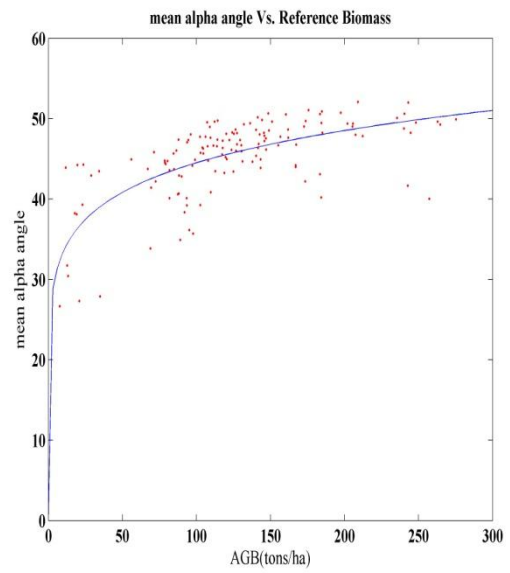


Figure 28

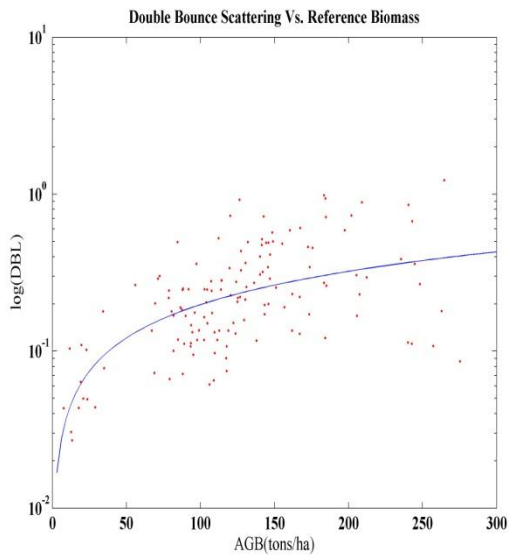


Figure 29

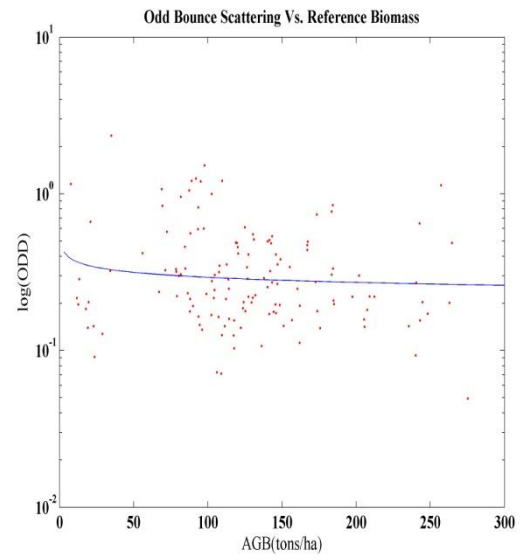


Figure 30

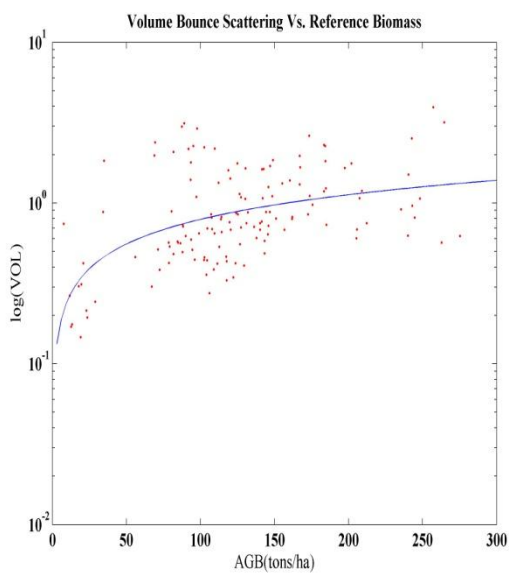


Figure 31

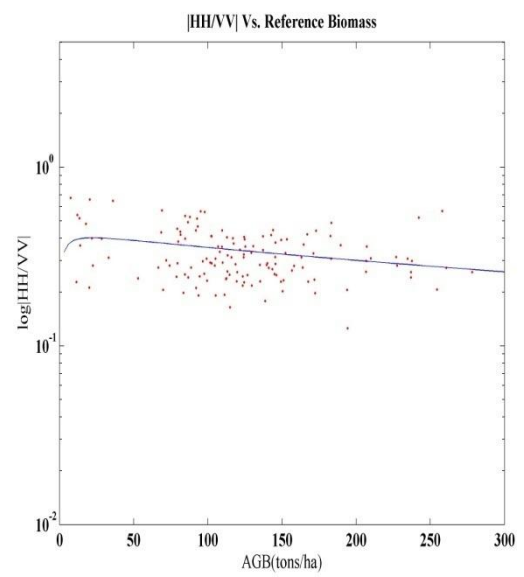


Figure 32

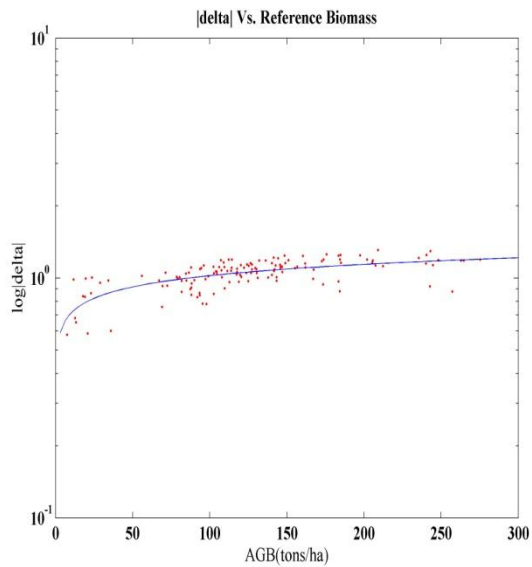


Figure 33

B.2 Table of Biomass Modeling Parameters:

Scattering Coefficient	Correlation Coefficient	RMSE	Model parameter 'a1'	Model parameter 'a2'
HH+VV	0.098	57.7125	0.0259	2.0732
HH-VV	0.5251	49.2640	0.0714	2.2541
HV	0.2647	55.3707	0.0426	2.3431
H	0.1603	58.2388	0.03195	2.5785
A	0.4518	51.3135	-0.5433	0.255
$\bar{\alpha}$	0.6047	45.4192	0.3788	-4.2272
Double Bounce	0.4786	50.4349	0.0532	2.3953
Odd Bounce	-0.1775	57.9470	-0.0097	1.9816
Volume Scatter	0.3266	54.1124	0.0498	2.0757
HH/VV	0.2357	49.6139	0.0175	0.8577
\delta	0.6314	44.8769	0.3059	1.9882

C. L-band Biomass Modeling Results:

C.1 Plots of Backscattering coefficient vs. Reference Biomass:

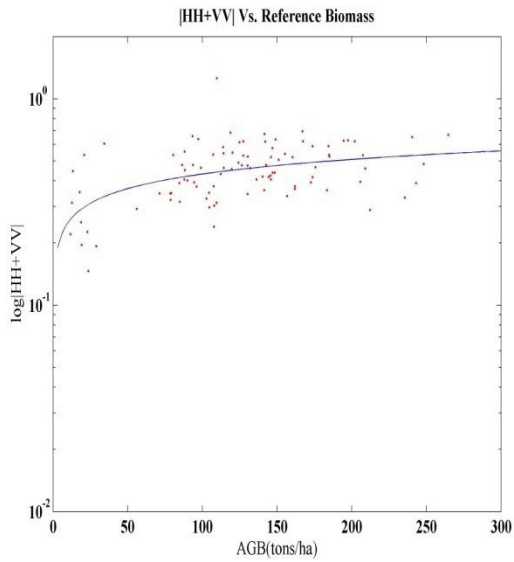


Figure 34

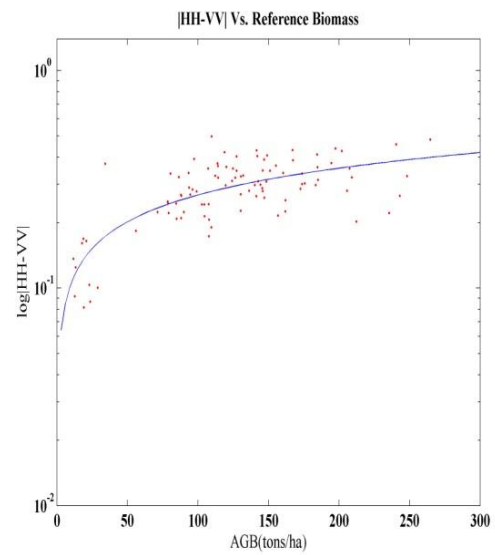


Figure 35

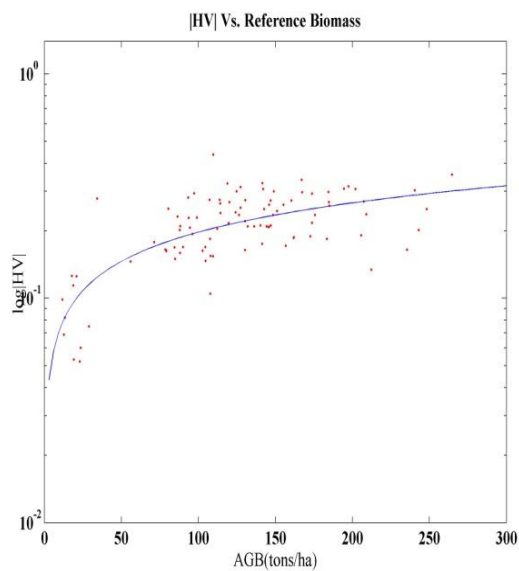


Figure 36

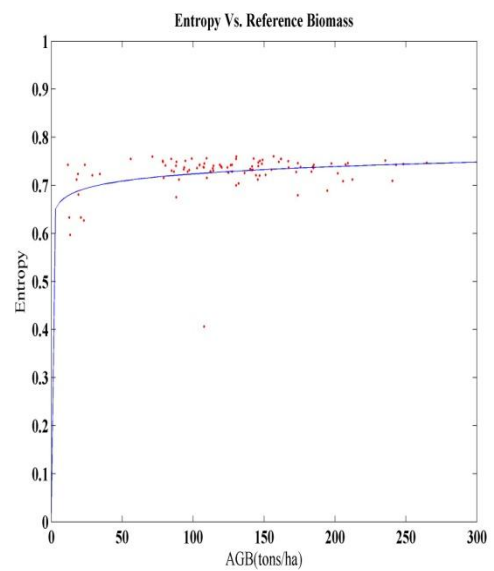


Figure 37

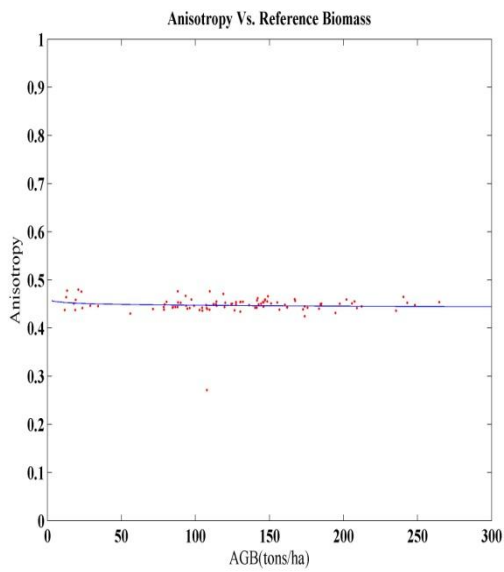


Figure 38

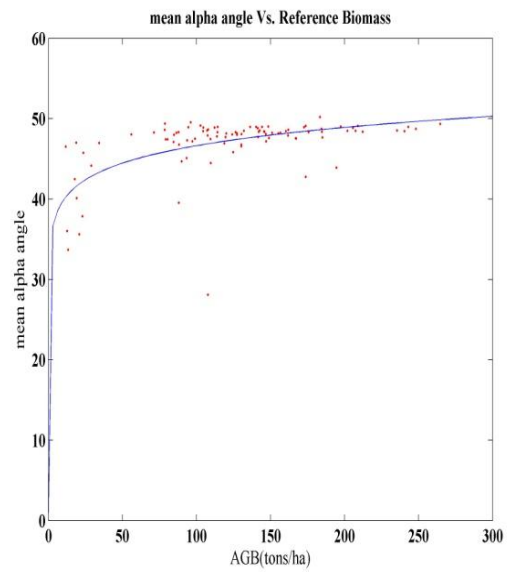


Figure 39

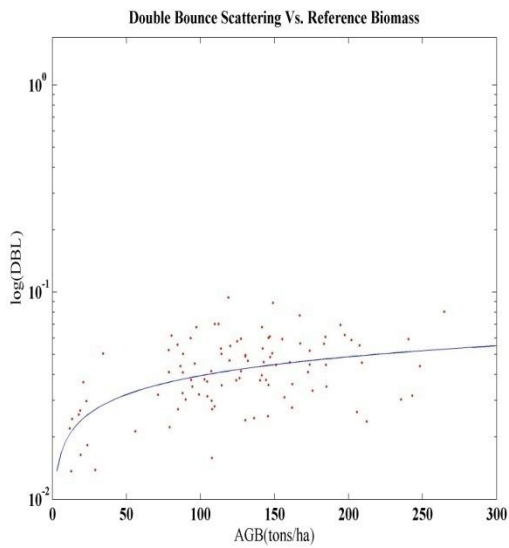


Figure 40

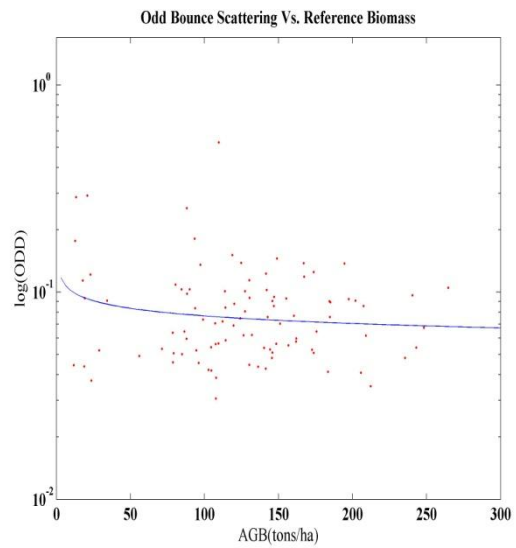


Figure 41

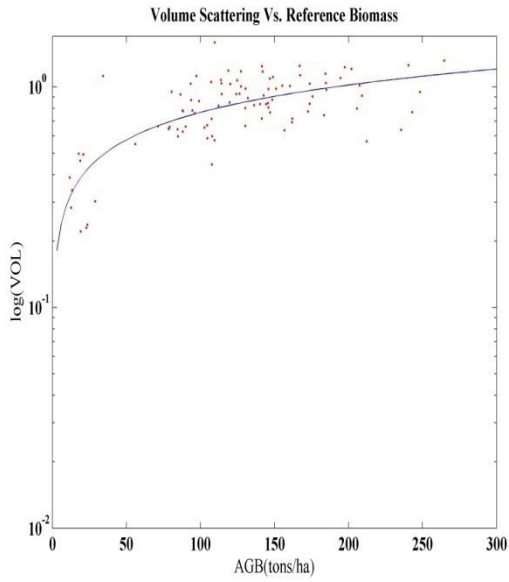


Figure 42

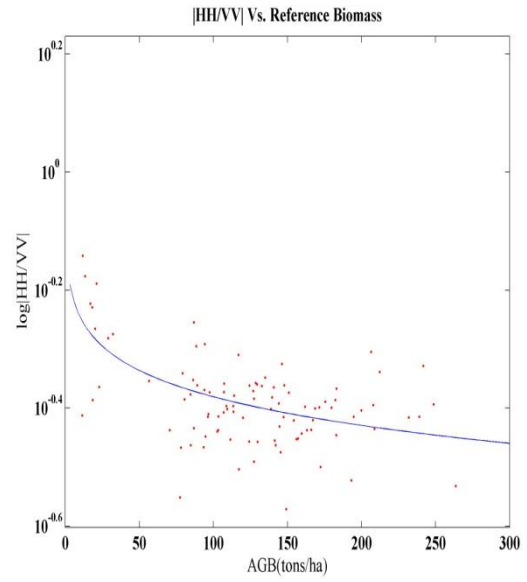


Figure 43

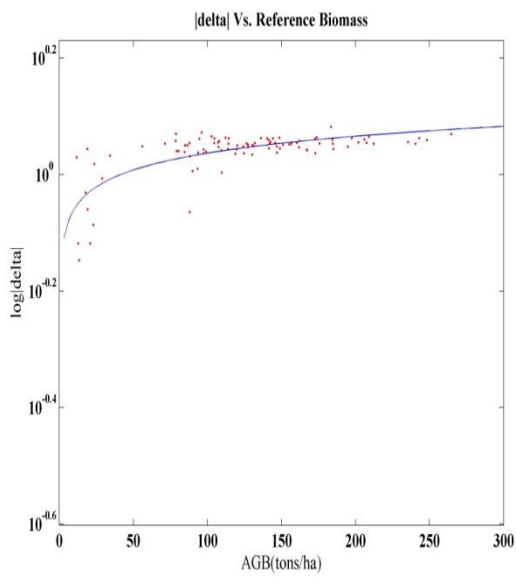


Figure 44

C.2 Table of Biomass Modeling Parameters:

Scattering Coefficient	Correlation Coefficient	RMSE	Model parameter 'a1'	Model parameter 'a2'
HH+VV	0.3474	53.9508	0.1043	2.3999
HH-VV	0.6015	46.7975	0.139	2.8058
HV	0.5618	48.2166	0.1241	2.8866
H	0.2509	55.1458	0.277	2.4134
A	-0.0292	57.4287	-0.0887	1.7157
$\bar{\alpha}$	0.4731	48.8666	0.4332	-5.2116
Double Bounce	0.3860	52.8291	0.0888	3.2649
Odd Bounce	-0.1793	57.0854	-0.0233	1.7655
Volume Scatter	0.5759	47.8492	0.1326	2.1642
HH/VV	-0.3196	49.9025	-0.0903	1.4737
\delta	0.5962	47.8968	0.5461	1.8094

Appendix 2

Appendix 2 includes the results of decomposition algorithms and biomass modeling for Heading Bio05.

A. Decomposition Results for P- and L-Band:

A.1. Pauli Decomposition:

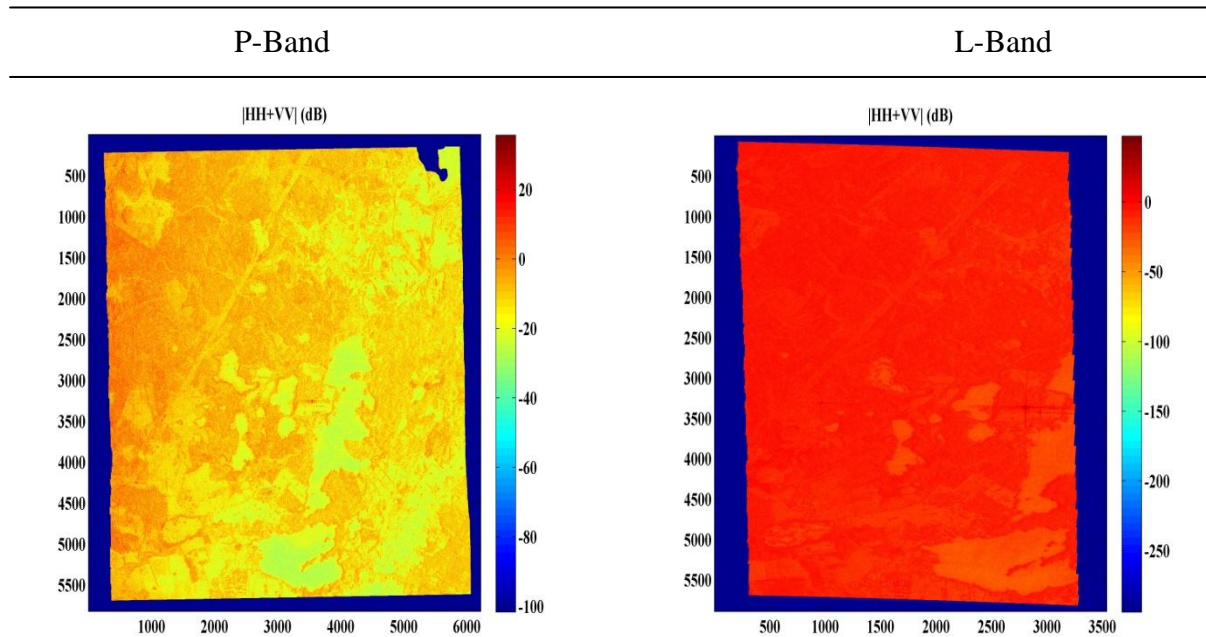


Figure 1

Figure 2

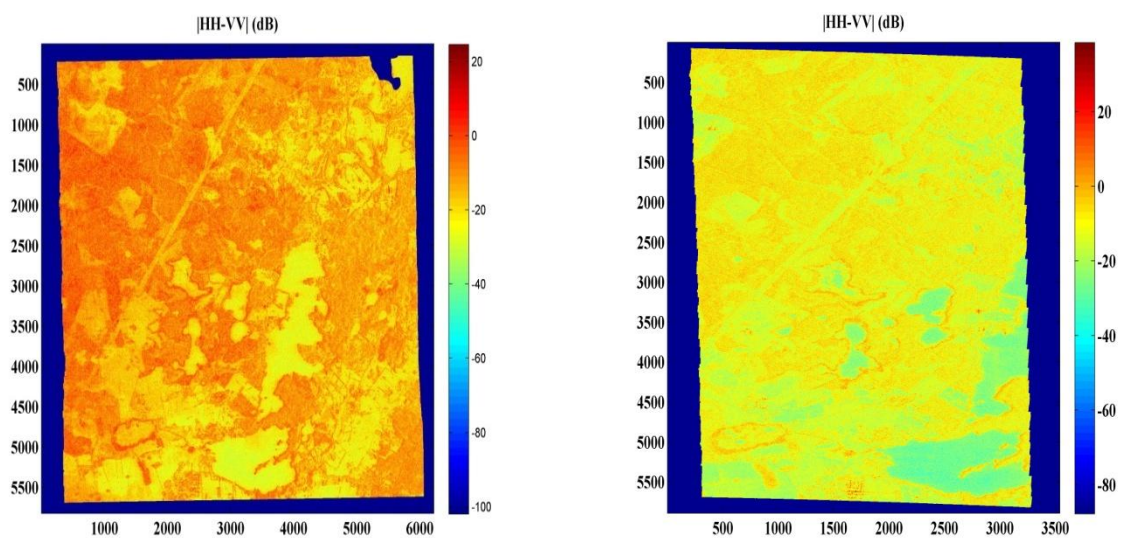


Figure 3

Figure 4

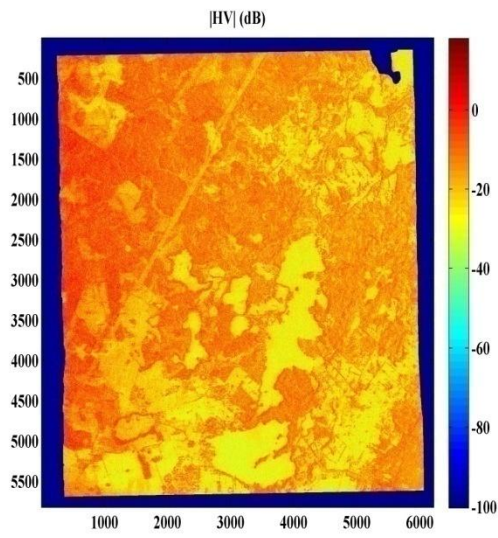


Figure 5

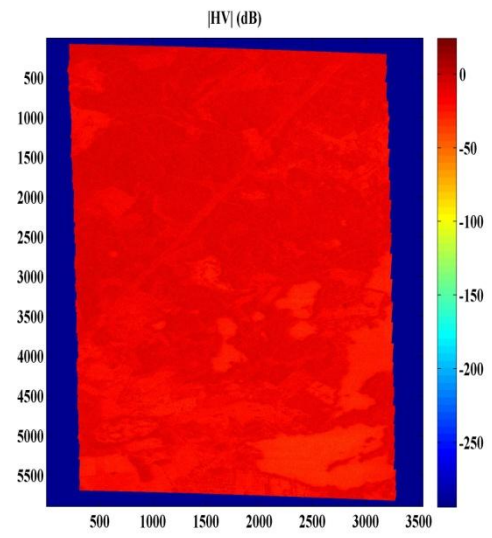


Figure 6



Figure 7

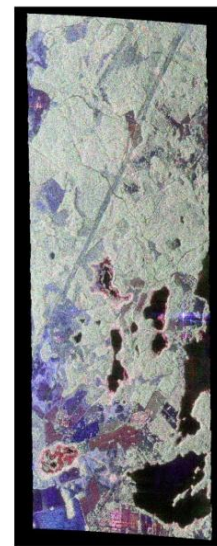


Figure 8

Pauli RGB image

Image color coded as Red: $|HH-VV|$, Green: $|HV|$ and Blue: $|HH+VV|$

A.2. Freeman-Durden Three Component Decomposition:

P-Band

L-Band

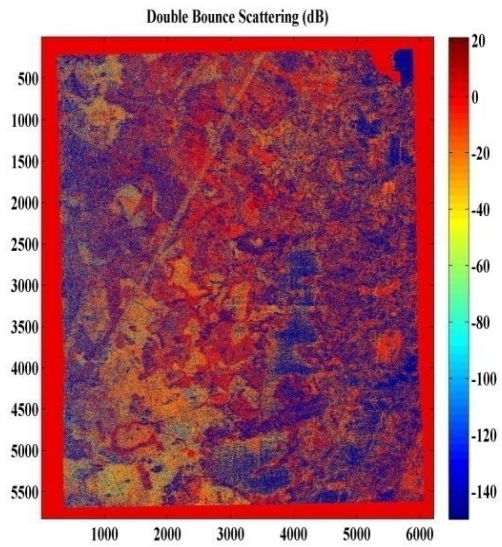


Figure 9

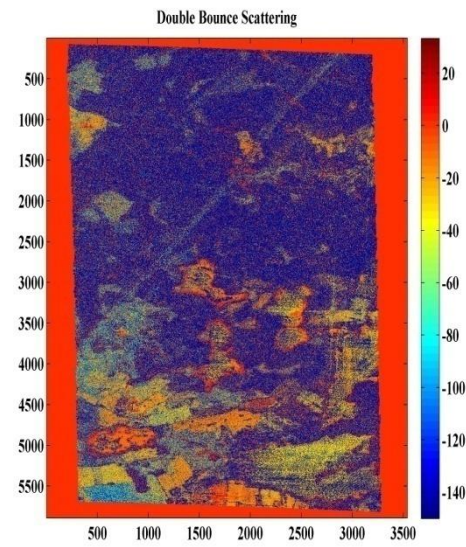


Figure 10

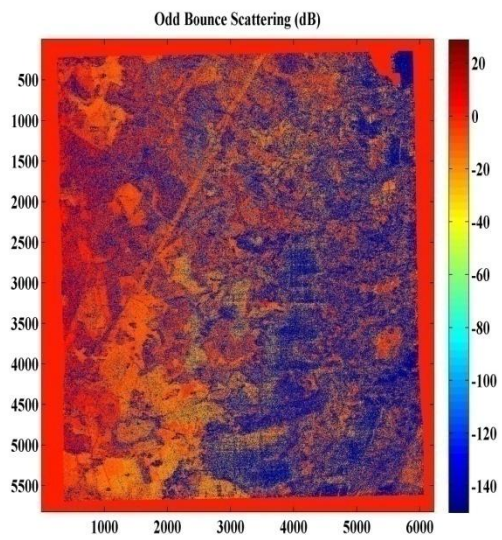


Figure 11

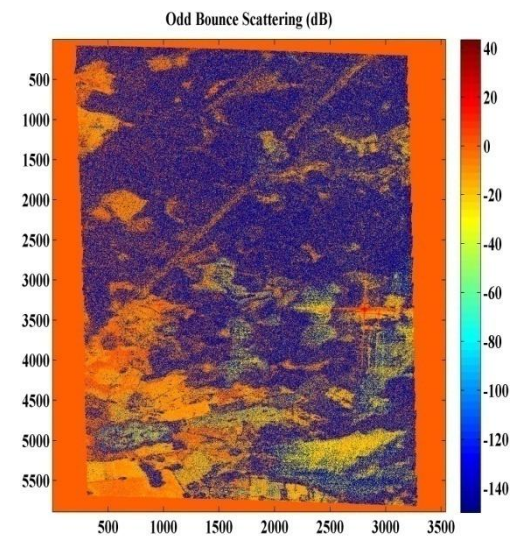


Figure 12

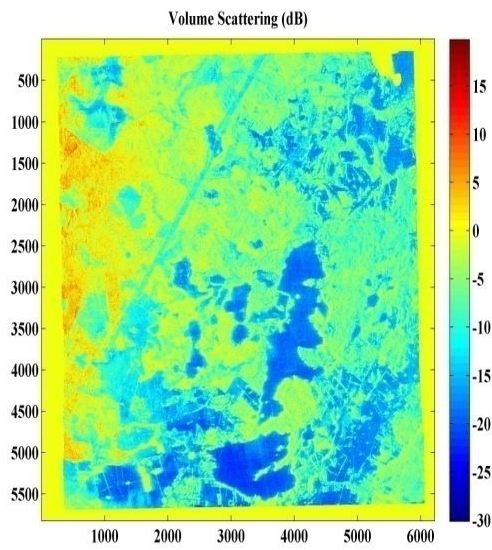


Figure 13

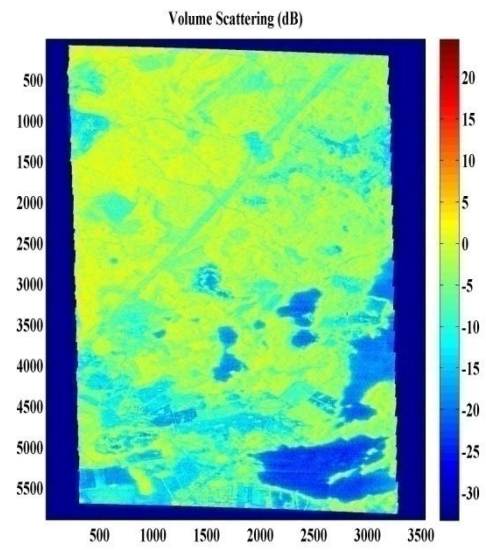


Figure 14

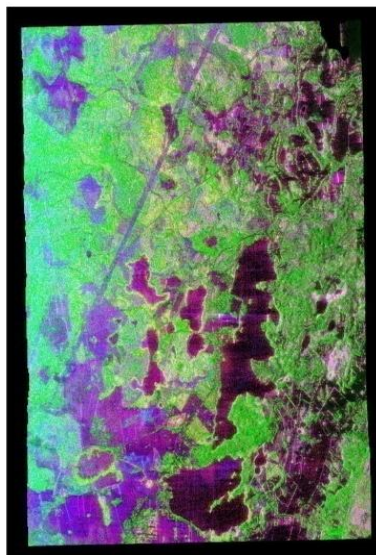


Figure 15

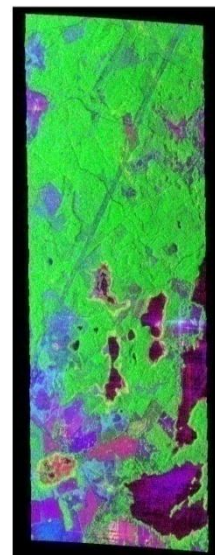


Figure 16

Freeman-Durden RGB image

Image color coded as Red: Double bounce, Green: Volume scatter, and Blue: Odd bounce

A.3. H/A/alpha Decomposition:

P-Band

L-Band

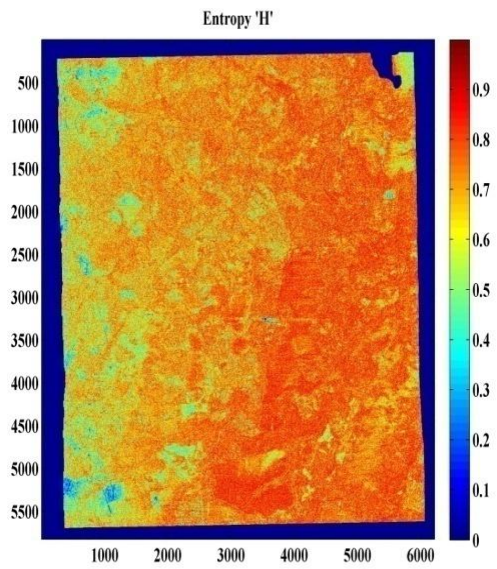


Figure 17

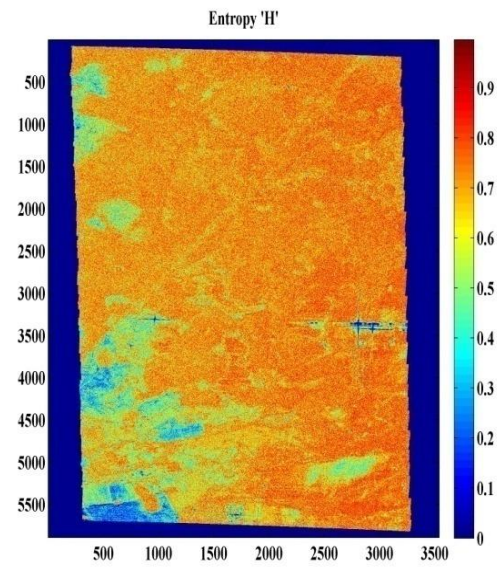


Figure 18

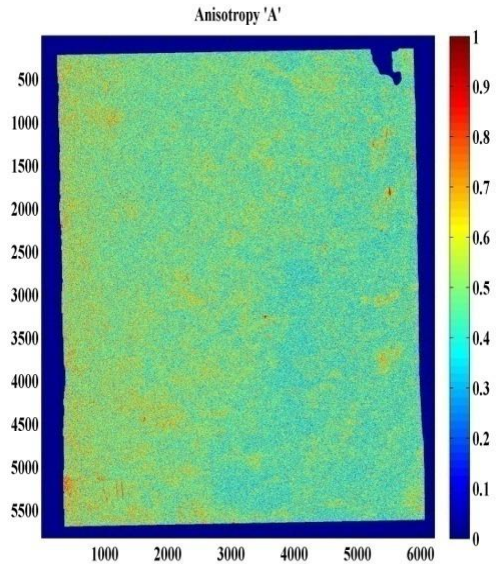


Figure 19

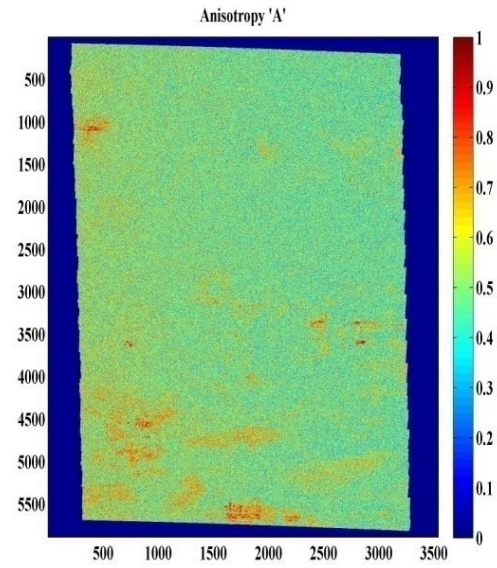


Figure 20

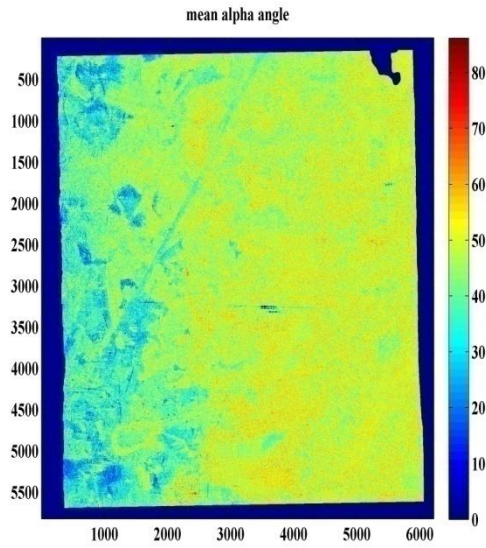


Figure 21

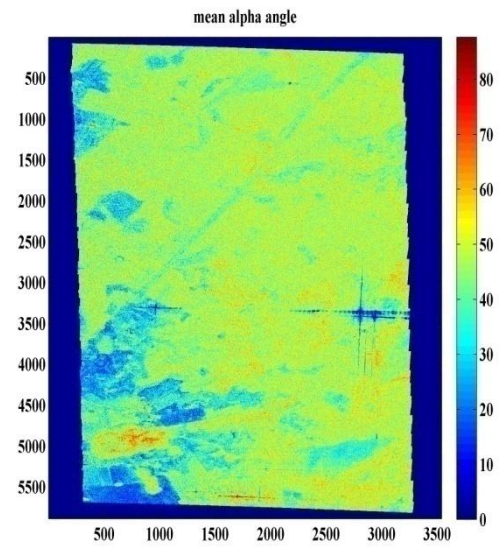


Figure 22

B. P-band Biomass modeling Results:

B.1 Plots of Backscattering Coefficient vs. Reference biomass:

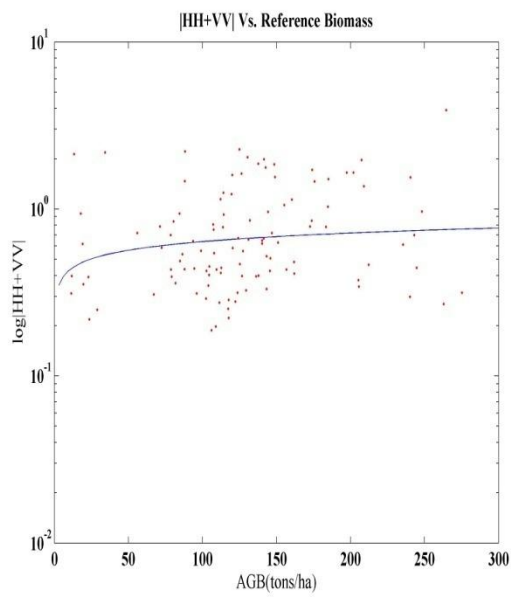


Figure 23

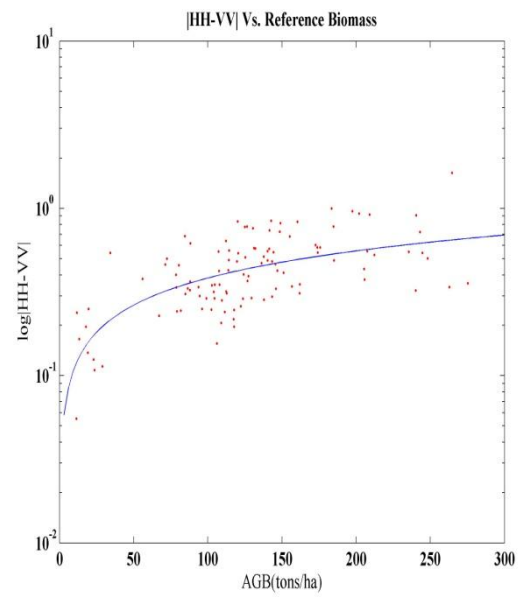


Figure 24

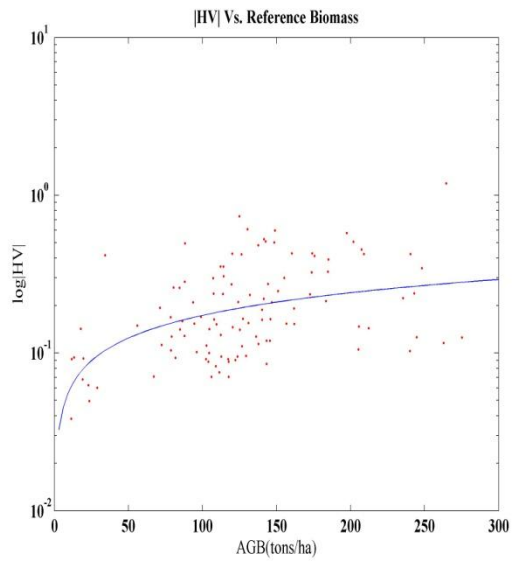


Figure 25

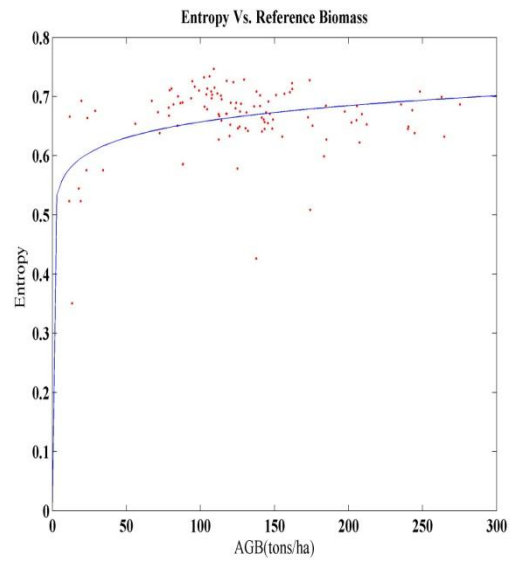


Figure 26

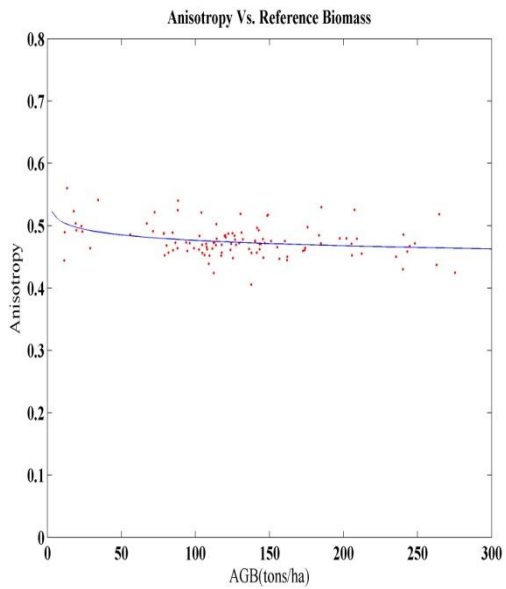


Figure 27

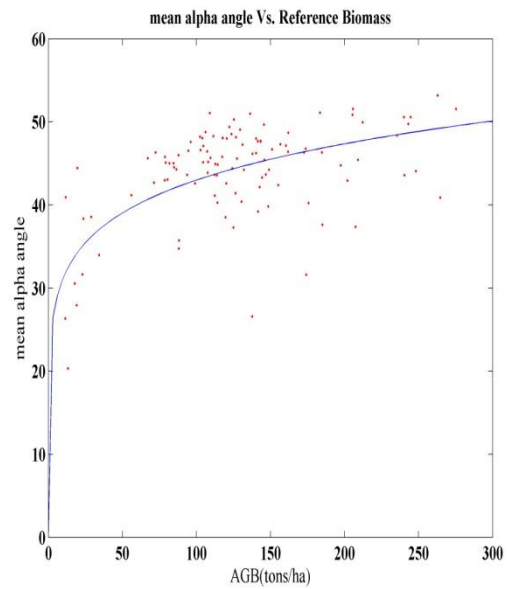


Figure 28

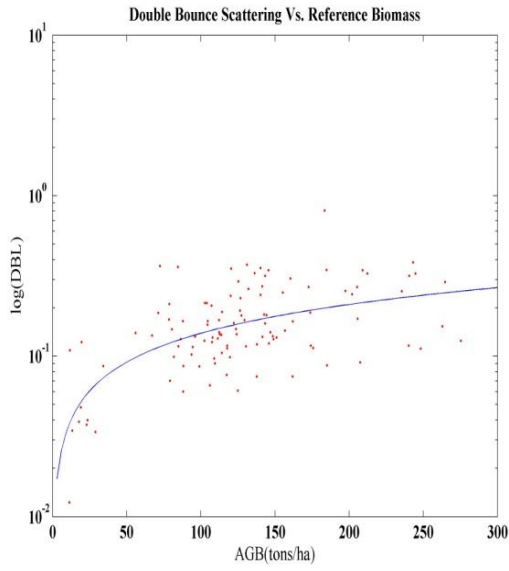


Figure 29

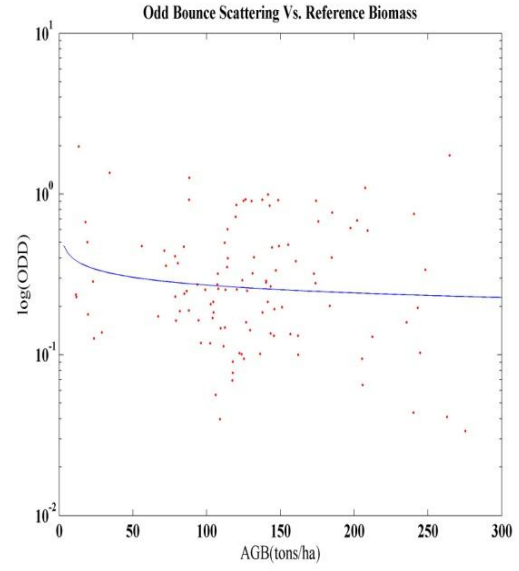


Figure 30

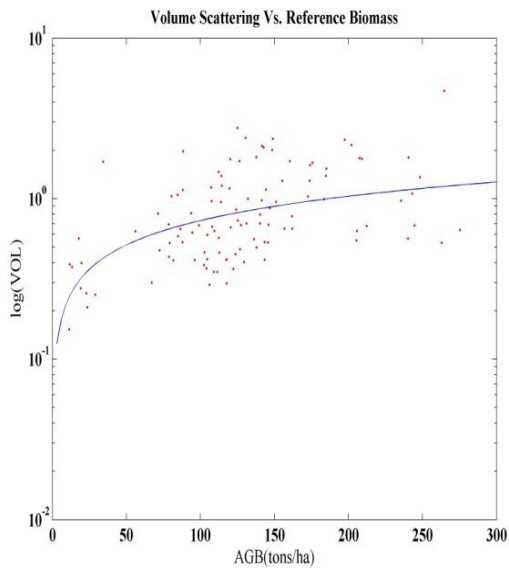


Figure 31

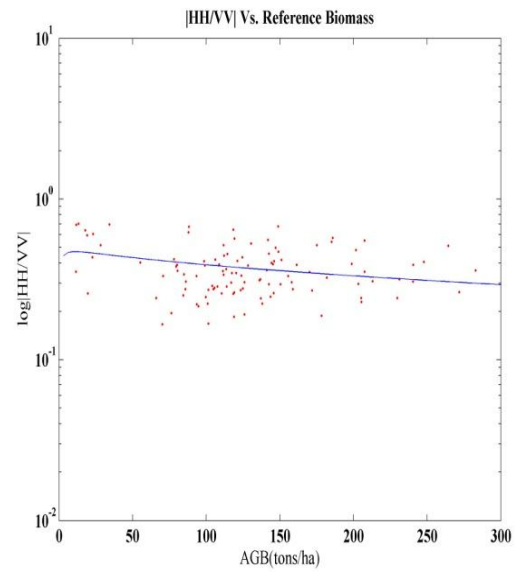


Figure 32

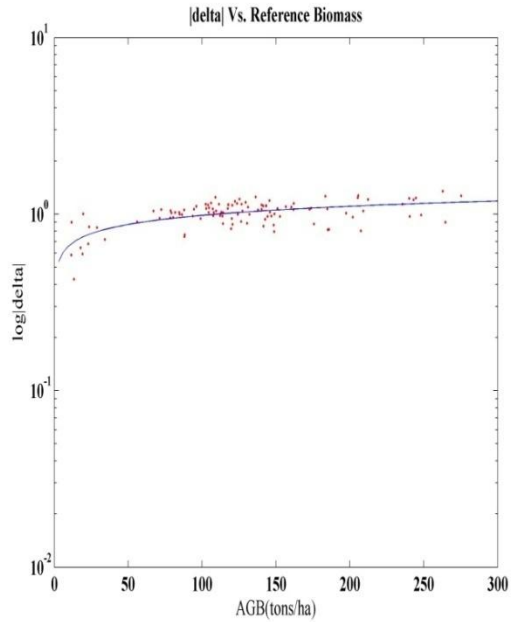


Figure 33

B.2 Table of Biomass Modeling Parameters:

Scattering Coefficient	Correlation Coefficient	RMSE	Model parameter 'a1'	Model parameter 'a2'
HH+VV	0.2039	57.5035	0.0164	2.0733
HH-VV	0.5529	48.3526	0.0807	2.3601
HV	0.3814	53.4885	0.0452	2.3773
H	0.1875	57.8852	0.2412	2.4761
A	-0.2897	56.1884	-0.3927	0.7738
$\bar{\alpha}$	0.466	51.5989	0.2571	-2.1716
Double Bounce	0.424	51.8290	0.0643	2.5779
Odd Bounce	-0.0204	58.1637	-0.0093	1.9891
Volume Scatter	0.417	52.3176	0.052	2.1022
HH/VV	0.1542	53.3285	0.0064	1.8293
\delta	0.5082	50.6959	0.2377	2.0425

C. L-band Biomass Modeling Results:

C.1 Plots of Backscattering Coefficient vs. Reference Biomass:

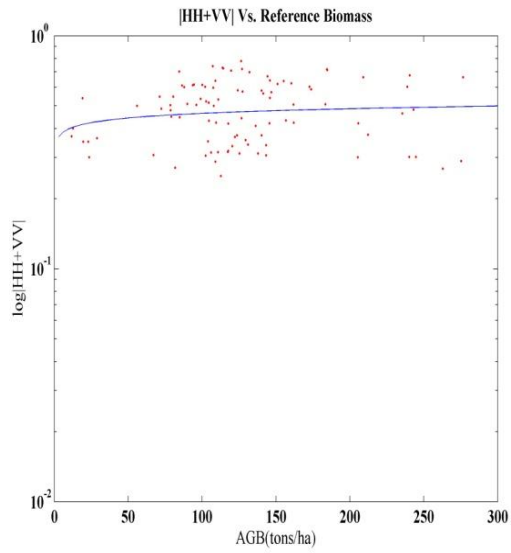


Figure 34

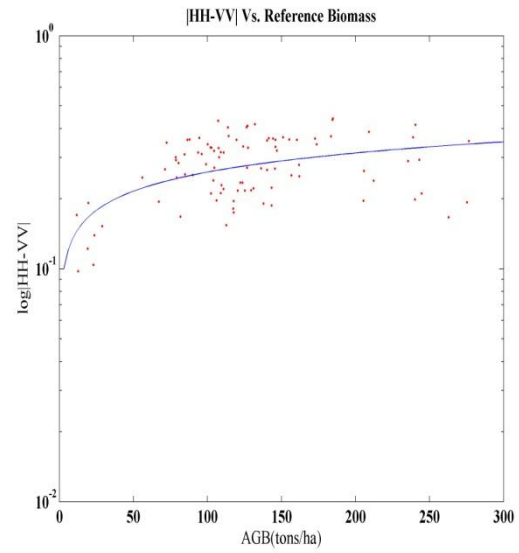


Figure 35

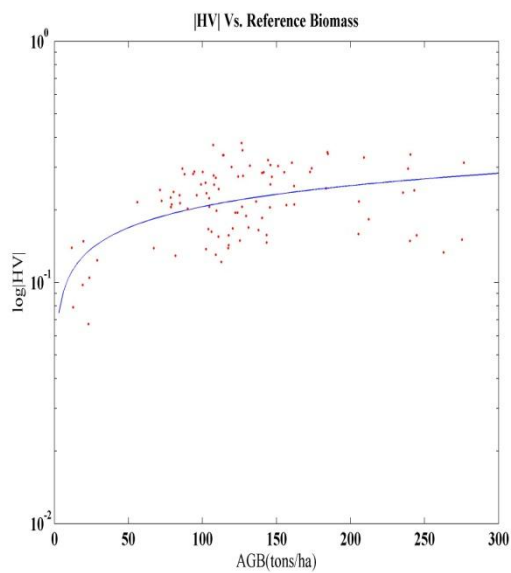


Figure 36

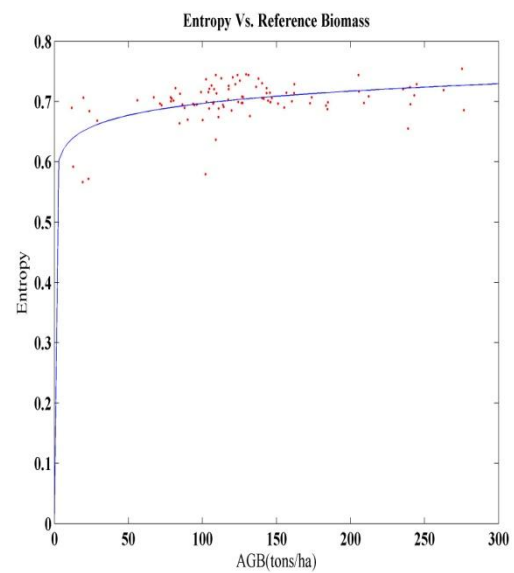


Figure 37

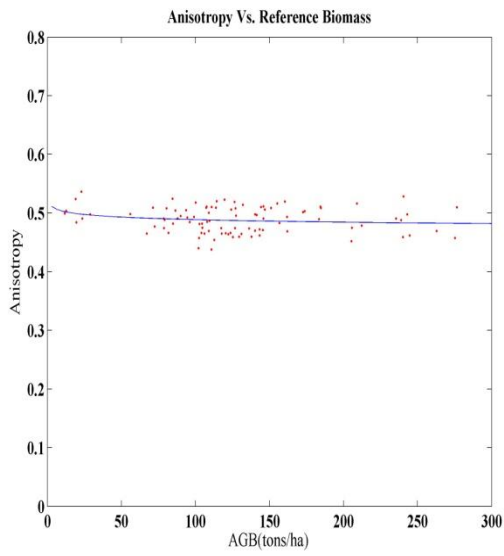


Figure 38

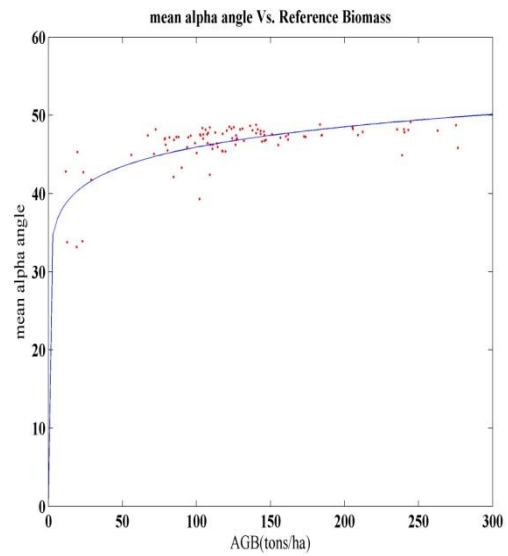


Figure 39

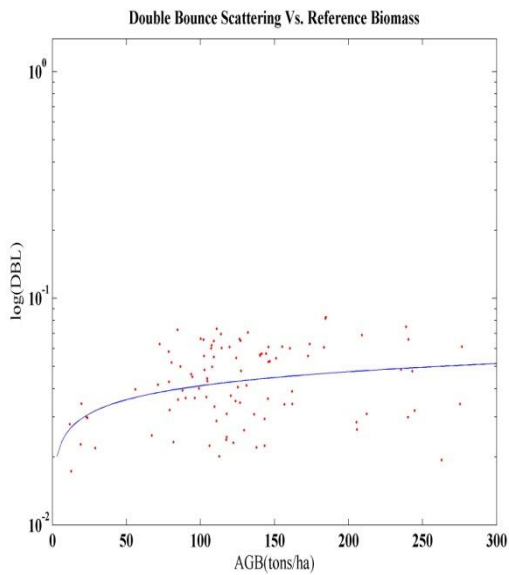


Figure 40

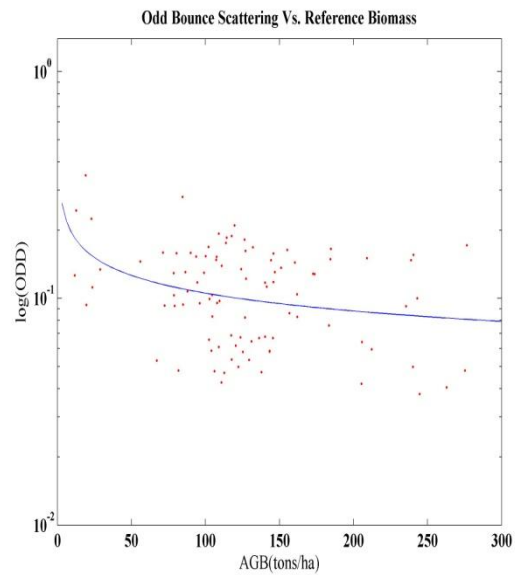


Figure 41

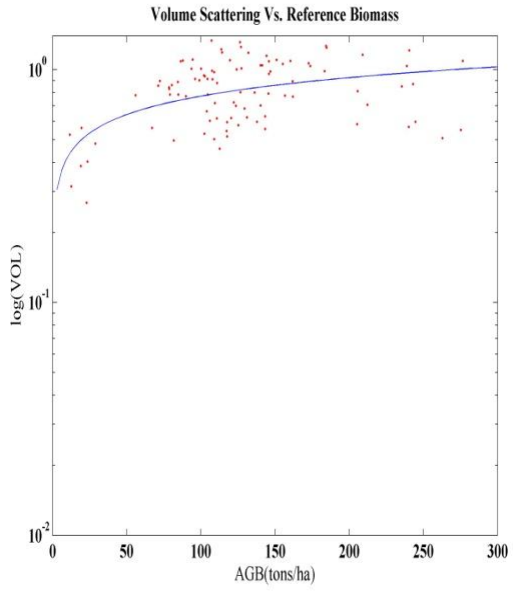


Figure 42

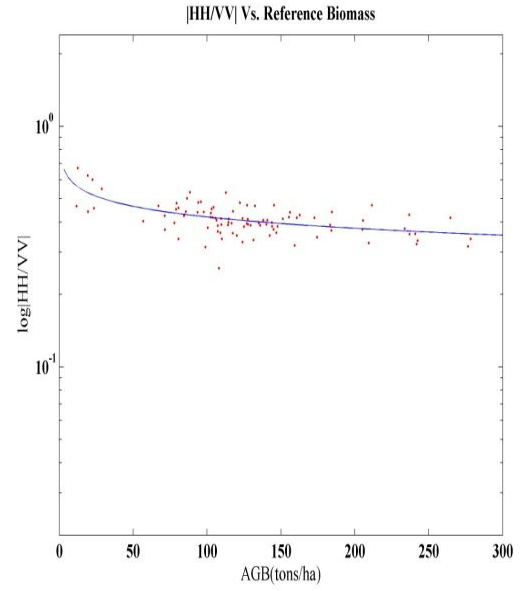


Figure 43

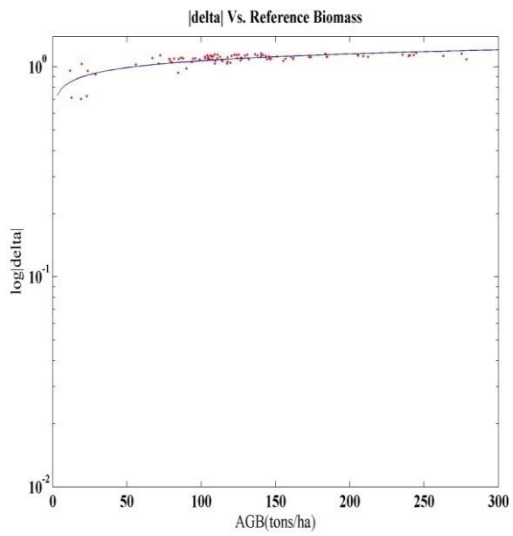


Figure 44

C.2 Table of Biomass Modeling Parameters:

Scattering Coefficient	Correlation Coefficient	RMSE	Model parameter 'a1'	Model parameter 'a2'
HH+VV	0.0709	57.8988	0.0266	2.1356
HH-VV	0.2942	55.3921	0.096	2.5269
HV	0.2950	55.3142	0.0852	2.6206
H	0.3724	54.1058	0.6103	2.9926
A	-0.1122	57.6020	-0.2341	1.3186
$\bar{\alpha}$	0.5299	47.8591	0.6176	-8.2412
Double Bounce	0.2161	56.6601	0.0504	2.7413
Odd Bounce	-0.2947	55.4882	-0.0395	1.6569
Volume Scatter	0.2748	55.6803	0.0893	2.1374
HH/VV	-0.4751	50.8543	-0.1131	1.5144
\delta	0.5953	44.0366	0.5368	1.8595

Appendix 3

Appendix 3 includes the results of decomposition algorithms and biomass modeling for Heading Bio07.

A. Decomposition Results for P- and L-Band:

A.1. Pauli Decomposition:

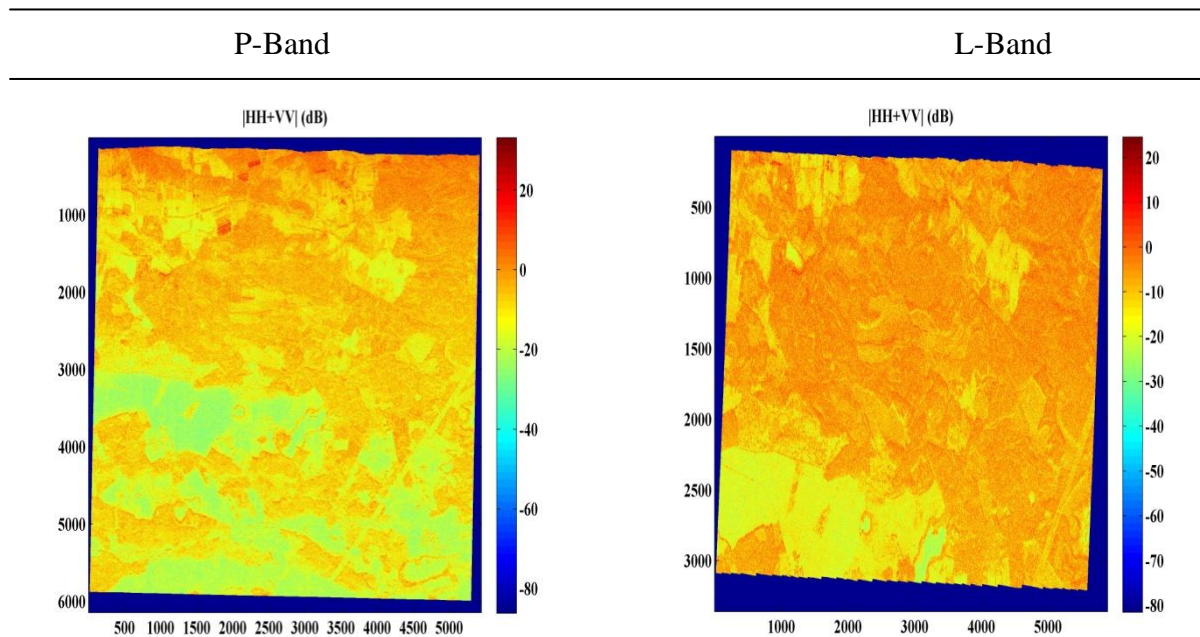


Figure 1

Figure 2

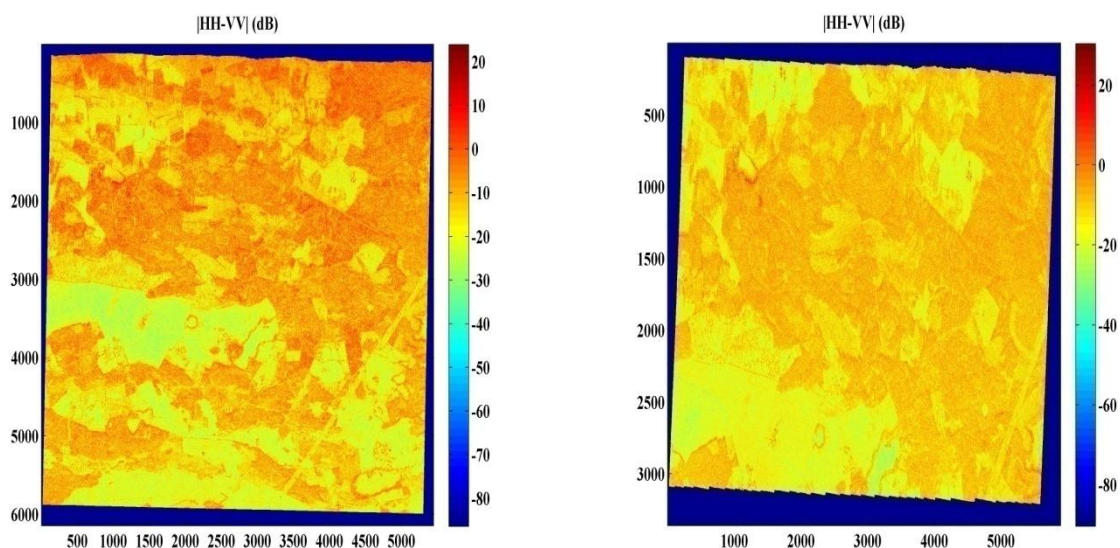


Figure 3

Figure 4

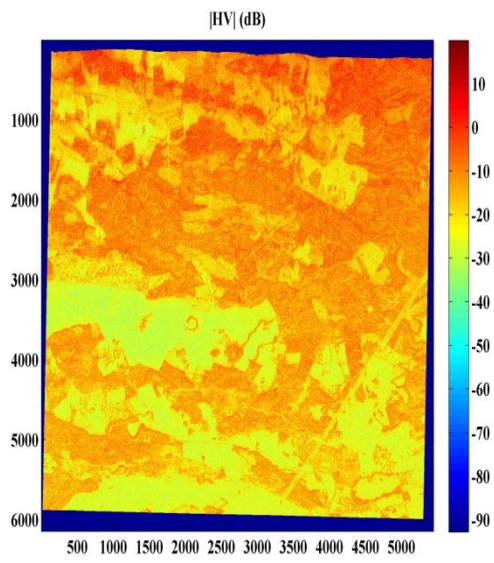


Figure 5

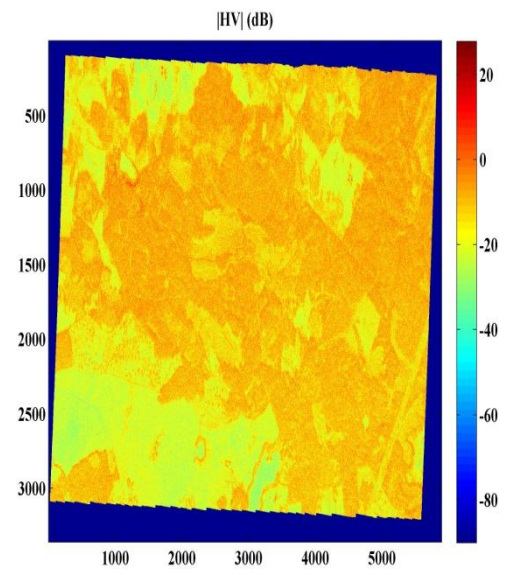


Figure 6



Figure 7

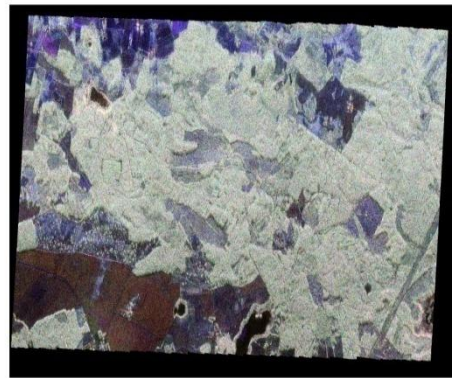


Figure 8

Pauli RGB image

Image color coded as Red: $|HH-VV|$, Green: $|HV|$, and Blue: $|HH+VV|$

A.2. Freeman-Durden Three Component Decomposition:

P-Band

L-Band

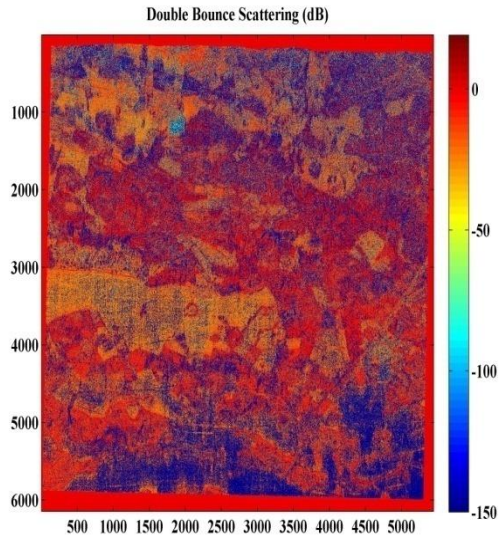


Figure 9

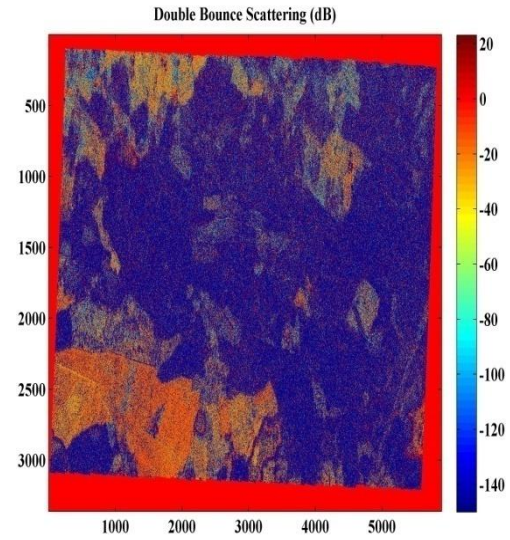


Figure 10

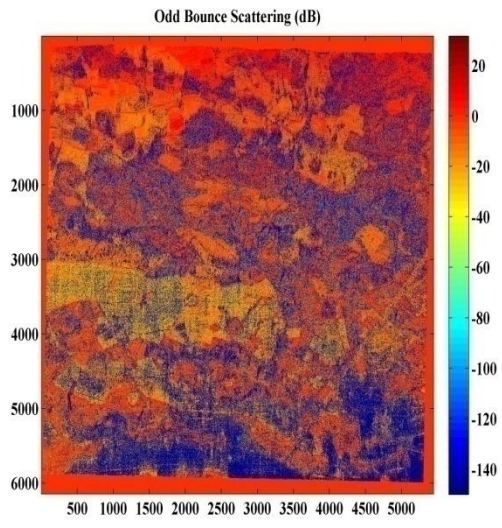


Figure 11

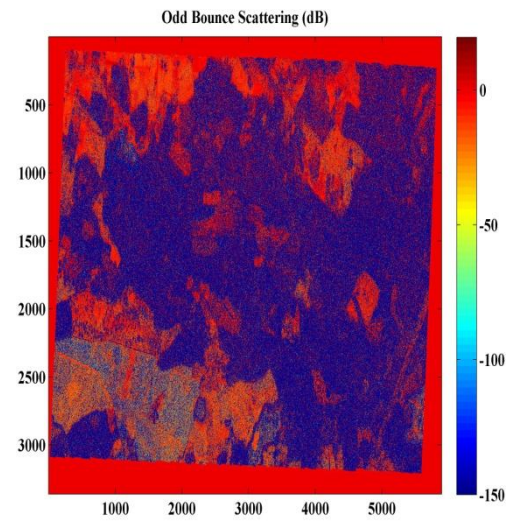


Figure 12

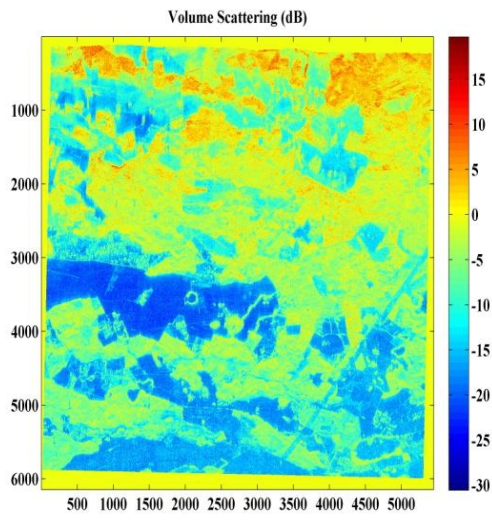


Figure 13

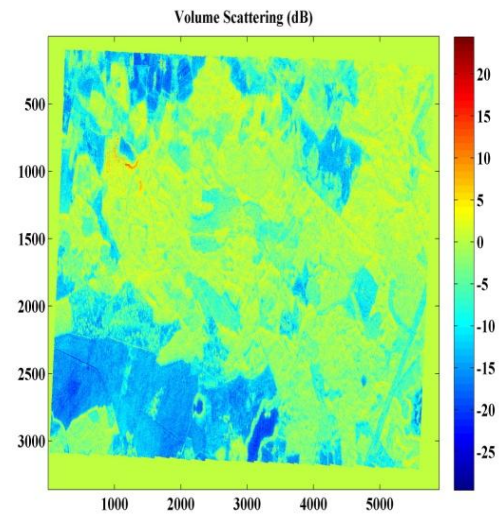


Figure 14

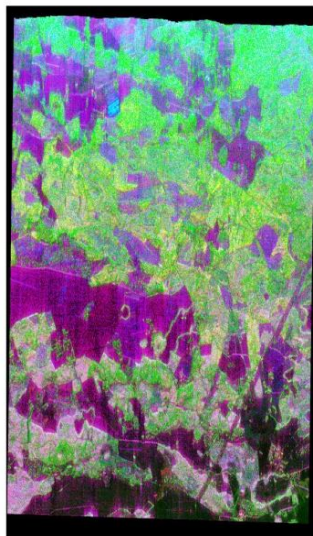


Figure 15

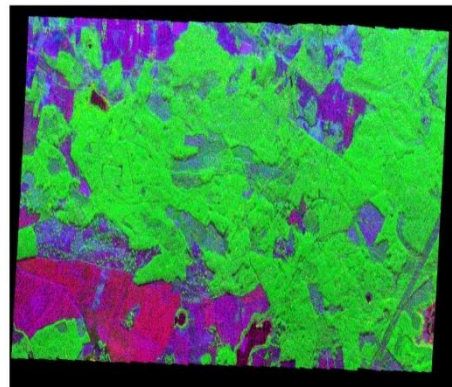


Figure 16

Freeman-Durden RGB image

Image color coded as Red: Double bounce, Green: Volume scatter, and Blue: Odd bounce

A.3. H/A/alpha Decomposition:

P-Band

L-Band

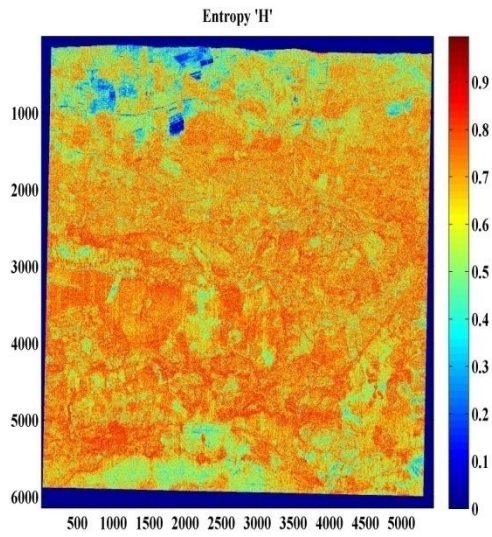


Figure 17

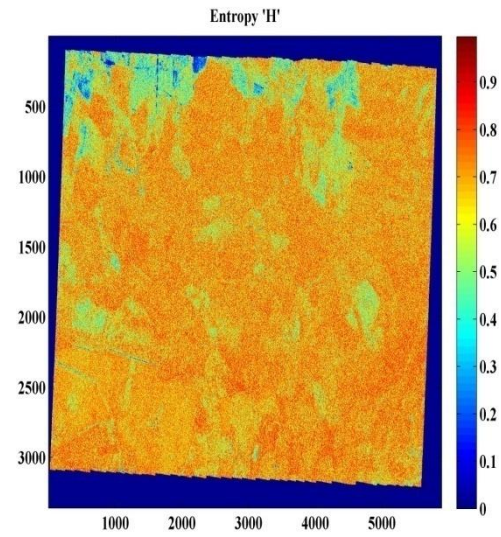


Figure 18

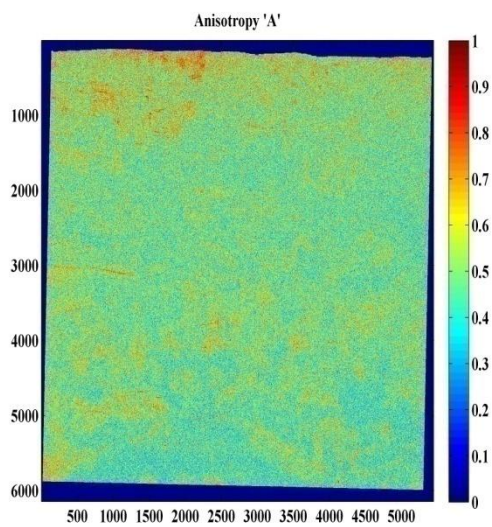


Figure 19

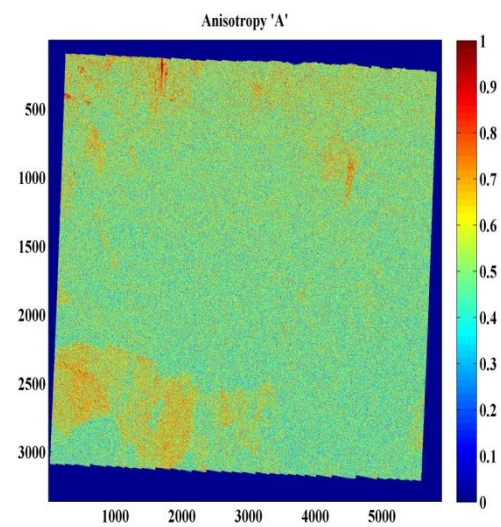


Figure 20

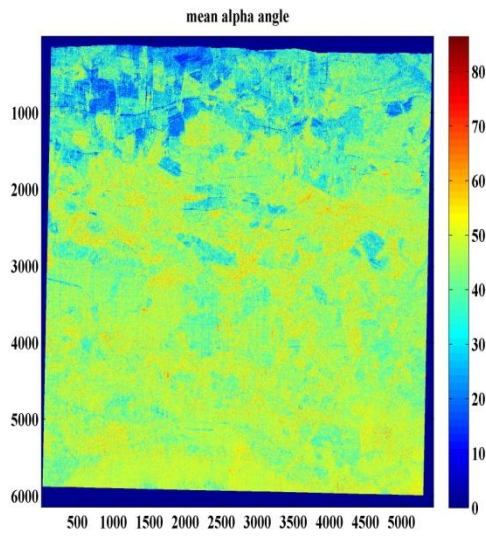


Figure 21

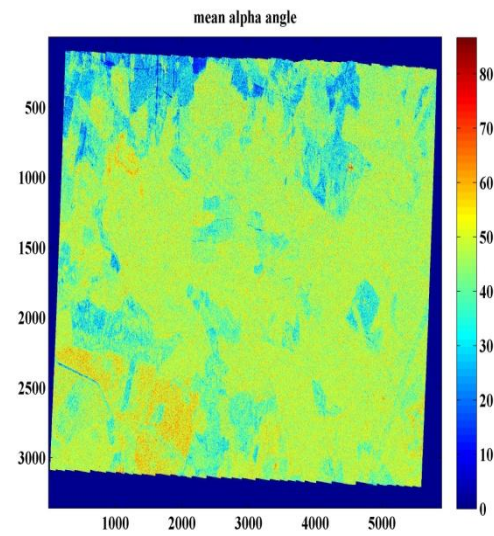


Figure 22

B. P-band Biomass Modeling Results:

B.1 Plots of Backscattering Coefficient vs. Reference Biomass:

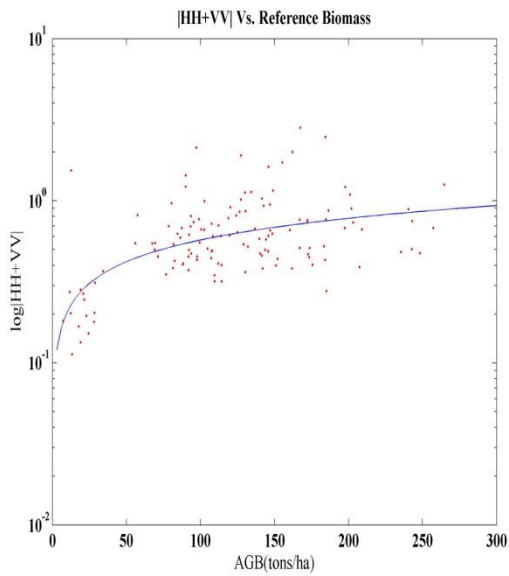


Figure 23

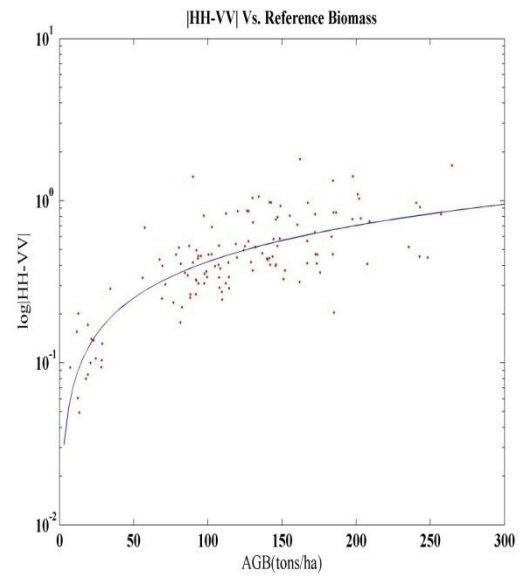


Figure 24

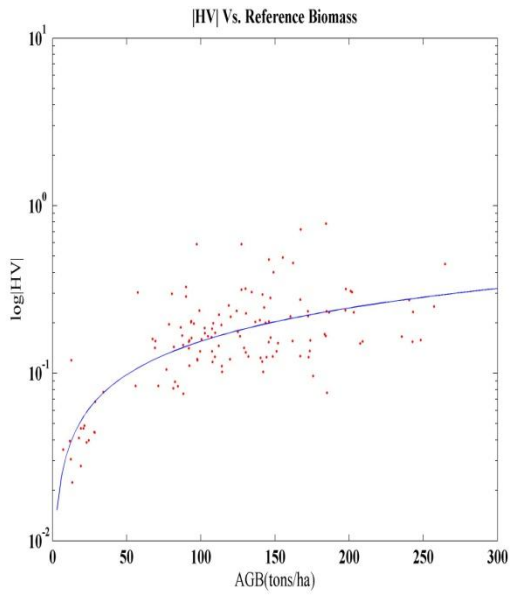


Figure 25

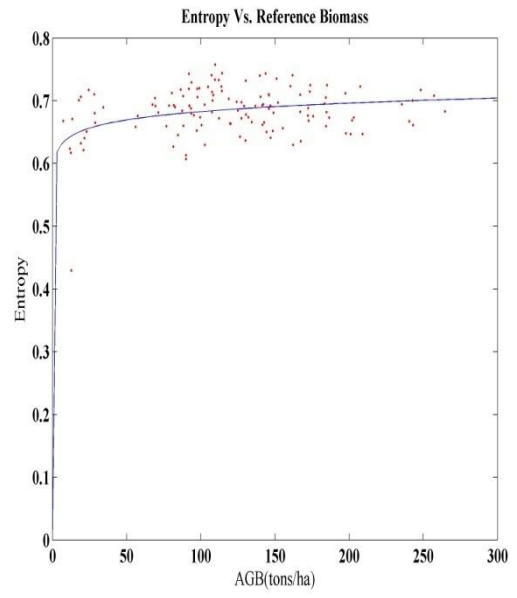


Figure 26

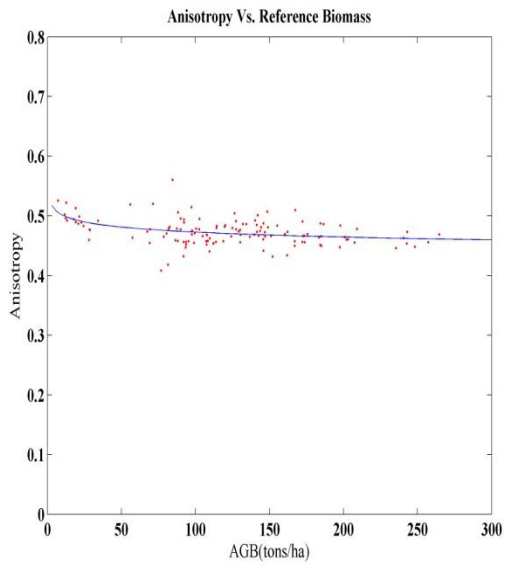


Figure 27

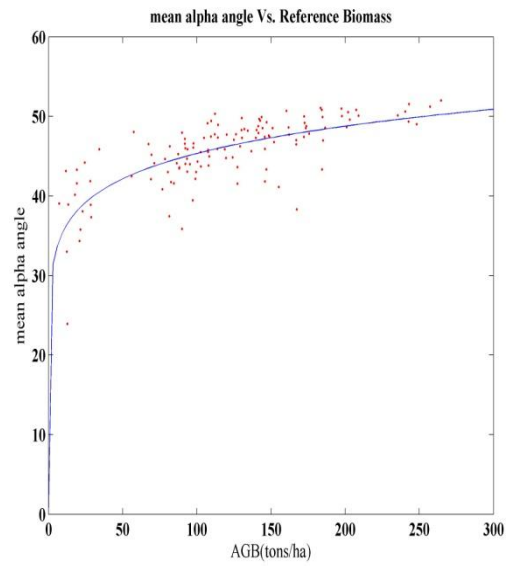


Figure 28

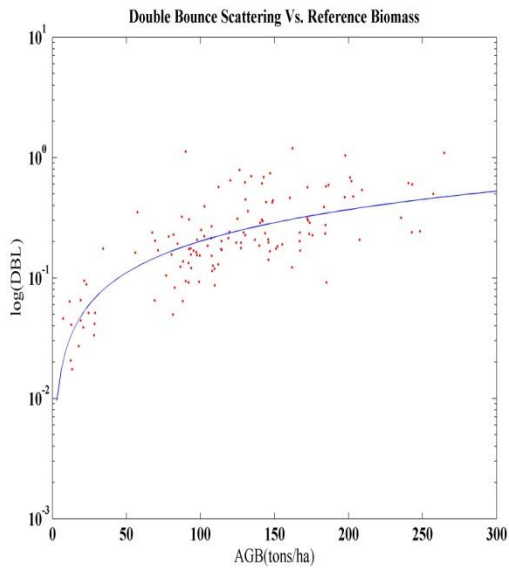


Figure 29

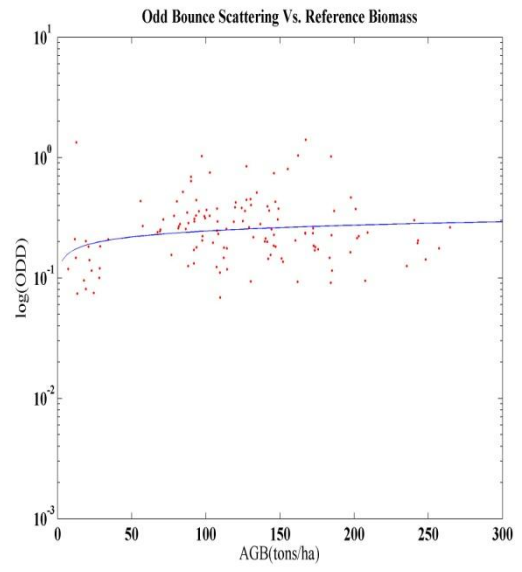


Figure 30

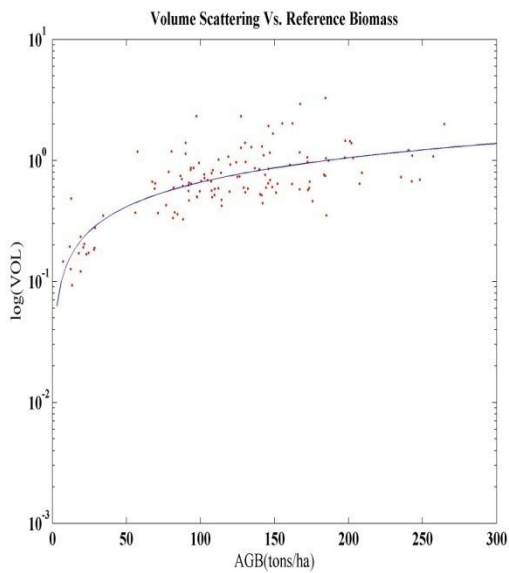


Figure 31

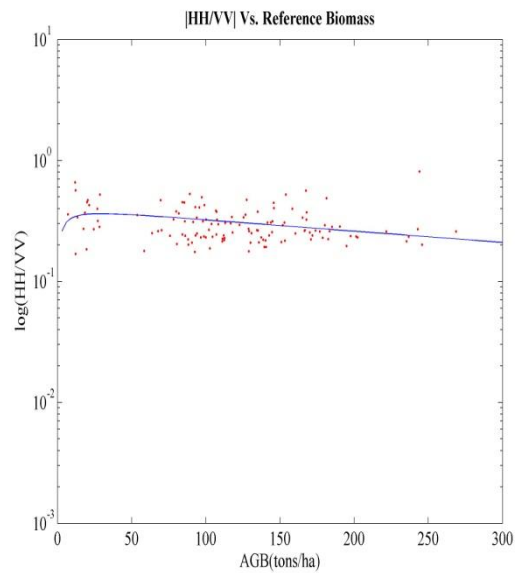


Figure 32

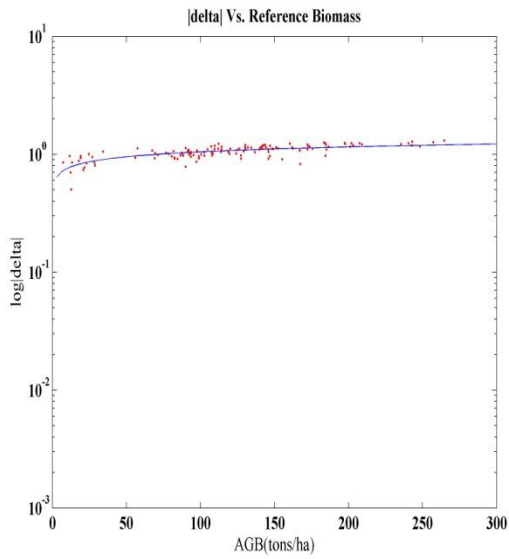


Figure 33

B.2 Table of Biomass Modeling Parameters:

Scattering Coefficient	Correlation Coefficient	RMSE	Model parameter 'a1'	Model parameter 'a2'
HH+VV	0.3099	54.7233	0.0702	2.1713
HH-VV	0.6111	45.2721	0.0842	2.3172
HV	0.44	51.3711	0.0797	2.6459
H	0.2051	57.6411	0.3850	2.6396
A	-0.3508	56.2370	-0.6386	-0.0759
$\bar{\alpha}$	0.7127	37.7253	0.4956	-6.2093
Double Bounce	0.5505	46.0753	0.0672	2.4466
Odd Bounce	0.0298	25.4207	0.0233	2.1442
Volume Scatter	0.4827	50.11421	0.0823	2.1497
HH/VV	0.3726	45.2651	0.0344	1.7807
\delta	0.7481	36.8956	0.3868	1.9234

C. L-band Biomass Modeling Results:

C.1 Plots of Backscattering Coefficient vs. Reference Biomass:

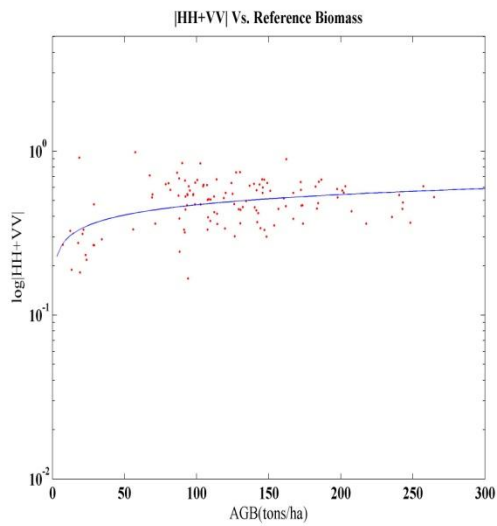


Figure 34

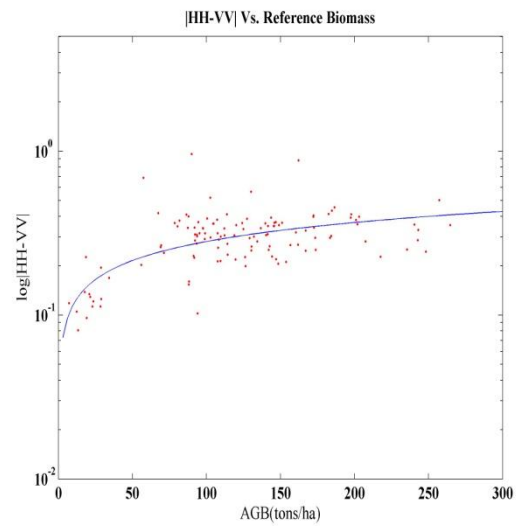


Figure 35

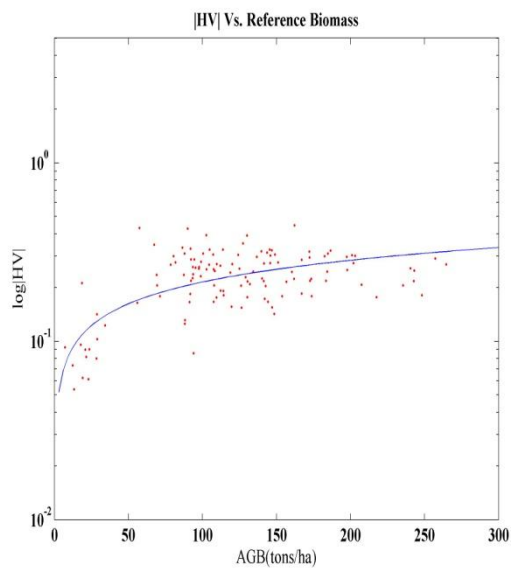


Figure 36

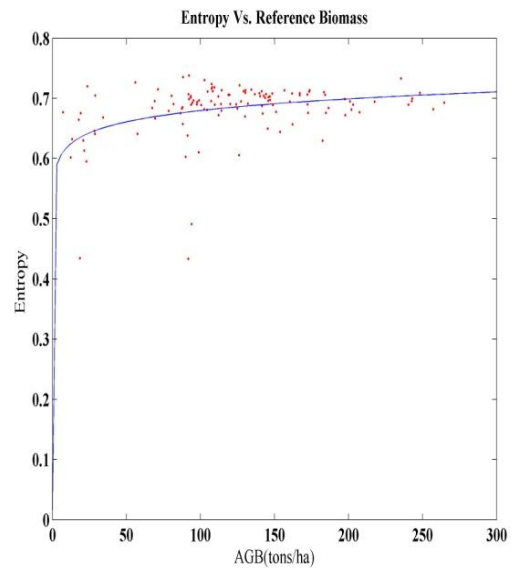


Figure 37

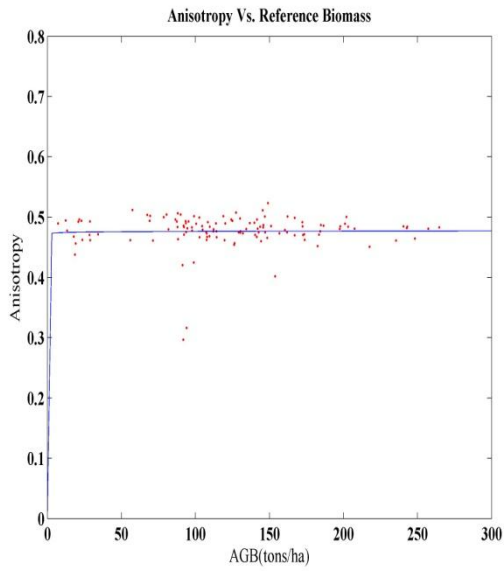


Figure 38

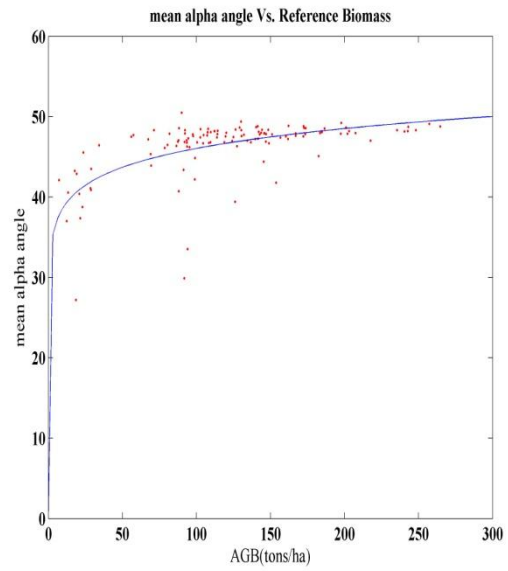


Figure 39

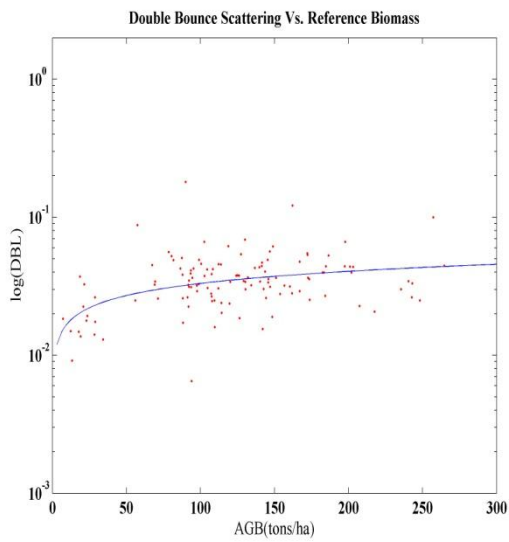


Figure 40

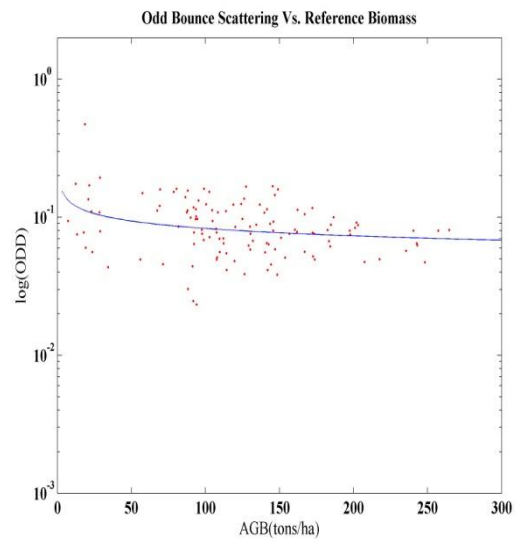


Figure 41

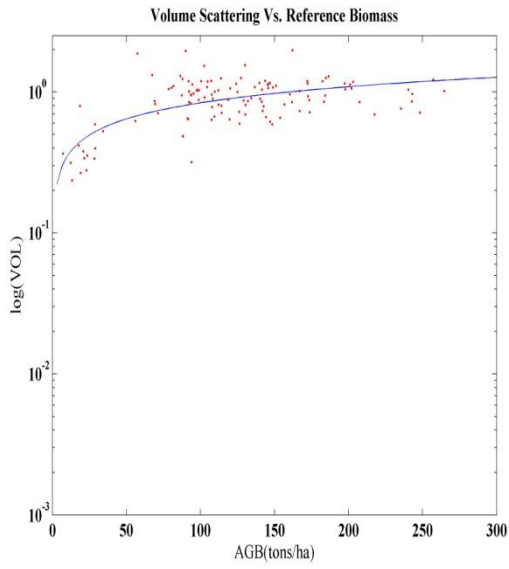


Figure 42

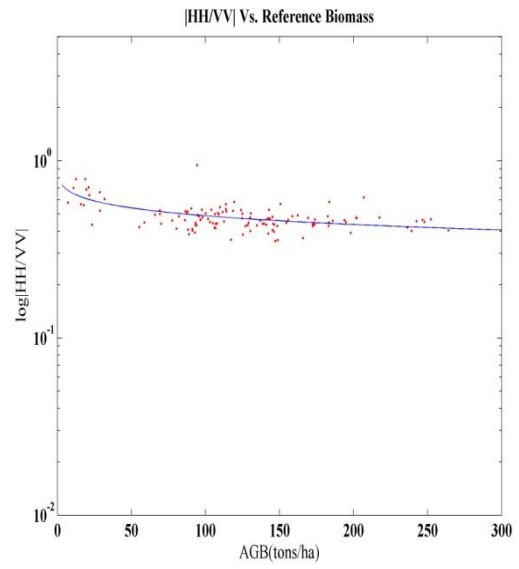


Figure 43

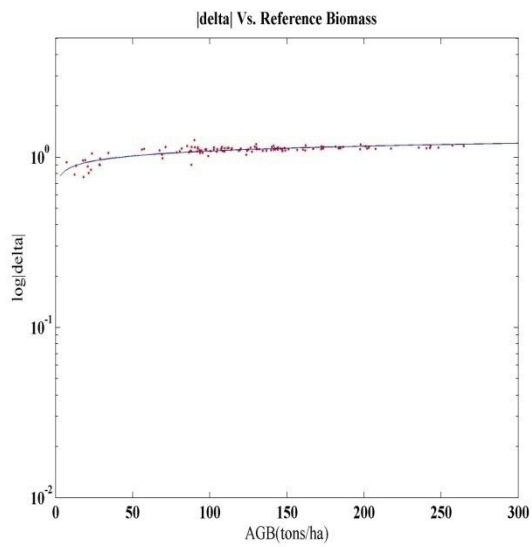


Figure 44

C.2 Table of Biomass Modeling Parameters:

Scattering Coefficient	Correlation Coefficient	RMSE	Model parameter 'a1'	Model parameter 'a2'
HH+VV	0.1969	56.1833	0.0845	2.2873
HH-VV	0.3439	54.1974	0.1056	2.59
HV	0.3771	53.4216	0.1062	2.7171
H	0.3098	54.4881	0.3113	2.5333
A	0.029	57.4588	0.017	2.068
$\bar{\alpha}$	0.5214	46.7915	0.4411	-5.3271
Double Bounce	0.2082	55.4849	0.0624	2.9337
Odd Bounce	-0.3175	56.1112	-0.0408	1.5712
Volume Scatter	0.3651	53.7721	0.1084	2.0903
HH/VV	-0.3971	47.6335	-0.1005	1.5758
\delta	0.6568	44.1123	0.6704	1.7644